POLITECNICO DI TORINO

Master's Degree Course in Automotive Engineering

Propulsion Systems Development

Master's Degree Thesis

Performance optimization of a lean-burn DI hydrogen engine via numerical simulation

Supervisors
Prof. Mirko Baratta
Prof. Daniela Misul

Candidate
Federico Ferraro

Academic year 2021/2022

Index

Index of figures

Index of tables

1. Introduction

The climate-change concerns, that have become prominent especially in the last decades, are leading to the introduction of more and more stringent pollutant species and carbon dioxide emissions regulations which, ideally, would aspire to the complete de-carbonization of the transport sector and to a fully sustainable mobility.

This perspective is pushing the automotive industry to seek for both new solutions and a further improvement of mature technologies.

Although the end-users are being more and more directed to the perception that vehicles' electrification is the only viable path towards the reduction of noxious emissions and climate risks, researchers are aware and convinced that internal combustion engines powered vehicles can still play an important role in the transport sector. For this reason, it must be expected that the future mobility will involve several solutions in terms of propulsion, including internal combustion engines, powered by either conventional or alternative fuels, and electrified powertrains.

Whichever solution will be considered, including electrification, it has to be remarked that one of the most important aspects from the propulsion point of view is concerned with the energy production: so as to achieve a true reduction of vehicles' emissions from this side, it would be needed to significantly increase the share of energy produced starting from renewable sources, since fossil fuels are still predominant.

In addition, in order to have a realistic and complete overview of the impact of vehicles on the environmental pollution, it should be performed a life-cycle analysis rather than focusing on the tank-to-wheel emissions only, by considering: the fuel extraction and refining processes and its transportation, the electricity production and distribution, the infrastructures, the mechanical parts' wearing as well as the components' end-of-life disposal.

Moreover, a complete transition towards electrification would require significant time and this is another reason to keep on investigating the potentialities of thermal engines.

In this complex scenario and with a focus on propulsion systems, internal combustion engines can still play an important role in the transport sector; if thinking to the history of such a mature technology, many efforts have been put into the improvement of several aspects, including the environmental impact, and outstanding results have been achieved.

Over the years, it has been possible to achieve a strong reduction of both CO_2 and pollutant species emissions by resorting to several solutions, which are not often mutually exclusive, the most significant of which are resumed in the following.

- Development of efficient aftertreatment systems such as three-way catalytic converter (TWC), selective catalytic reduction (SCR) systems, lean NOx traps (LNT), gasoline and diesel particulate filters (GPF and DPF).

- Development and enhancement of combustion systems and modes to improve the engine efficiency and to reduce the fuel consumption, including the combustion chamber design, the control of the charge motion within the cylinder and the mixture formation process.

- Employment of turbocharging (TC), downsizing and variable valve actuation (VVA).

- Investigation of different injection strategies, which led to an even more diffused adoption of direct injection (DI).

- Adoption of alternative fuels.

The core of the present dissertation is focused on the last-mentioned solution.

In particular, the starting point is a natural gas (NG) DI turbocharged spark ignition (SI) engine: the natural gas is a first step towards the emissions reduction, but it is still a carbon-based fuel.

The first part of the project is related to the calibration and the validation of 0D and 1D models of the reference engine against the available experimental data.

The second part of the project is concerned with a feasibility study of the switch from NG to pure hydrogen, firstly by adopting a stoichiometric mixture and then a lean one, with the objective of running the engine with a carbon-free fuel, which would allow to nominally set the pollutant species and CO_2 emissions to zero, and optimizing its performances.

1.1. Natural gas in internal combustion engines

Natural gas is a largely available mixture of different chemical species with variable composition and can be either extracted from gas wells or produced alongside other fossil species such as oil or coal.

The most significant species in the NG composition is methane, CH_4, present in a range of 70% - 98% by volume; among the other species, it is possible to find further hydrocarbons (e.g. ethane and propane), nitrogen, helium, carbon dioxide and water vapor.

Concerning the system layout of internal combustion engines running on NG, there are two possibilities.

On one hand, there are spark ignition gasoline engines which are converted aftermarket into NG ones and retaining bi-fueling capabilities, which are likely to suffer from power losses and drivability problems due to the design and installation of the additional components needed to perform the conversion (e.g. gas mixer, regulator, shut-off valves, control system and fuel storage system) despite the original characteristics of the engine architecture are maintained.

On the other hand, there are native SI NG internal combustion engines that allow to achieve better performances with respect to converted ones, since they are optimized for the reference fuel and their design is not bounded by the different characteristics of gasoline, which, as mentioned, in the case of converted engines, is alternated with NG.

As every solution, natural gas displays both advantages and disadvantages: some of the most relevant characteristics of NG as a fuel in ICEs are resumed in the following.

For first, the research octane number (RON) of NG is about 130, that is much higher than the gasoline one which, according to European Standards, must have a minimum RON=95 and the maximum value, which is the one characterizing iso-octane, is RON=100.

Since RON is one of the most important factors related to the probability of the knock onset and the higher it is the lower is the knock probability, native NG engines could operate at compression ratio (CR) up to 16, which is higher with respect to the gasoline-derived ones, which have CR typically ranging from 8 to 12, without knock or detonation. It has been found that, if comparing a gasoline-derived engine and an equivalent native NG one with

higher compression ratio, the thermal efficiency could be improved by about 10 to 20 percent.

Then, NG has wider flammability limits (5.3%-15% by volume) with respect to both gasoline and diesel oil, allowing to resort to a larger range of air-fuel ratios; the maximum thermal efficiency is attained when it is burnt in a lean mixture in the range $\lambda = 1.3 - 1.5$, despite this causes power losses. The maximum power, instead, is reached for slightly rich mixtures. Moreover, volumetric efficiency is lower with respect to gasoline, since NG is a gaseous fuel having very low density (0.72 kg/m^3 at 1 bar and 273 K) and so it displaces more volume compared to liquid fuels, leading to power reduction: this problem can be solved by considering different injection strategies, for example by passing from port fuel to direct injection, and turbocharging with a suitable boost pressure.

Another point to be addressed is related to the storage. Due to its low energy density at atmospheric conditions, NG is compressed and stored on-board at very high pressure, typically 200 bar: due to the weight and the space required by CNG (when stored in such a way, natural gas takes the name of "compressed natural gas") storage systems, the range of NG powered vehicles results to be lower with respect to conventional ones. The range limitations can be reduced if natural gas is stored in the liquid form (LNG), but in this case the drawback is related to the fact that, to have NG in liquid form, it must be stored at the cryogenic temperature of -162 °C. The systems needed to maintain this temperature introduce additional weight and costs.

One of the most important characteristics of natural gas as a fuel is related to its environmental impact. Since NG is primarily composed by methane, which has only one carbon atom, the CO_2 emissions are reduced up to 20-25% with respect to gasoline, which is composed by longer and heavier hydrocarbons chains (e.g. iso-octane C_8H_{18}). Non-methane unburned hydrocarbons are reduced by about 50% (which, among the other advantages, leads to a reduction of the photochemical smog), carbon monoxide emissions are reduced up to 70-95% and nitrogen oxides up to 50-87%. The drawback of natural gas from this point of view is related to the methane unburned hydrocarbons emissions, which are higher with respect to gasoline engines and that require dedicated aftertreatment systems since their oxidation is not so simple. Moreover, methane itself is a greenhouse gas with a global warming potential (GWP) equal to 25, compared with the carbon dioxide

which is characterized by the reference value GWP=1; yet, the impact on the overall greenhouse gas emissions performance depends not only on GWP but also to the extent of the emissions themselves.

1.2. Hydrogen in internal combustion engines

Hydrogen is the lightest element, the first one on the periodic table and, at standard conditions, is a diatomic gas having the formula H_2. On the contrary with respect to NG, which is considered a primary energy source, hydrogen is an energy carrier (like electricity). In the field of energetics, an energy carrier is produced by human technology from a primary energy source; in fact, hydrogen can be produced in different ways.

The most common industrial production method consists in the steam methane reforming process, which usually starts from breaking down heavier hydrocarbons into methane (pre-reforming). Then, the first reaction to take place is the steam methane reforming (SMR) one, which is expressed by the following equation:

(1.1) $CH_4 + H_2O \leftrightarrow CO + 3H_2$

Secondly, by means of the water-gas shift reaction (WGSR), consisting in the reaction between water and the carbon monoxide generated by (1.1), further hydrogen is produced:

(1.2) $CO + H_2O \leftrightarrow CO_2 + H_2$

Moreover, during the steam reforming process, other reactions occur, such as the direct steam reforming (DSR):

(1.3) $CH_4 + 2H_2O \leftrightarrow CO_2 + 4H_2$

One of the main drawbacks of this process, apart from the large amount of energy needed to keep constant the reactor temperature ((1.1) and (1.3) are endothermic reactions), is the release of carbon dioxide into the atmosphere. To mitigate the effect of this method on the climate change, very often a share of the so produced CO_2 is captured by means of the carbon capture and storage (CCS) method.

Another way to produce hydrogen, always starting from natural gas, is the methane pyrolysis, which consists in breaking CH_4 down into gaseous hydrogen and solid carbon by using a molten metal catalyst at 1340 K:

(1.4) $CH_4(g) \rightarrow C(s) + 2H_2(g)$

Apart from hydrogen itself and the solid carbon which, in any case, is not released into the atmosphere and therefore causes no pollution, no other byproducts result from this reaction.

A third method to produce hydrogen is the water electrolysis, which consists in running a current through the water, with the formation of gaseous hydrogen at the cathode and gaseous oxygen at the anode:

(1.5) $2H_2O(l) \rightarrow 2H_2(g) + O_2(g)$

As for methane pyrolysis, also in this case no CO_2 is produced.

The main problem is that, whichever is the considered method, the energy which is necessary to produce hydrogen is higher with respect to the energy that the hydrogen can provide when it is converted into useful energy (e.g. in internal combustion engines for propulsion or in fuel cells to generate electricity): despite it is true that, if hydrogen is oxidized to generate energy, only water is produced and therefore it could be considered completely green the point is that, as mentioned earlier, the vast majority of the available energy sources needed to produce hydrogen as well as electricity is still hydrocarbon-based. To reduce the overall climate impact, it would be necessary to resort to more and more renewable energy sources.

Net of this consideration, hydrogen is characterized by properties that make it suitable to be employed as a fuel in conventional internal combustion engines and is one of the most promising substitutes of hydrocarbon-based fuels with near-zero emissions and satisfactory efficiencies. Leaving apart the employment of hydrogen in fuel cells for electricity production, which is beyond the scope of this dissertation, the most important characteristics of this species and its use as a fuel in internal combustion engines are discussed in the following.

Hydrogen has a very wide flammability range, even wider than the methane one, that is 4%-75% by volume, corresponding to $0.1 < \Phi < 7.1$ in terms of equivalence ratio. The lower limit implies the possibility to resort to a wide range of air-fuel ratios including

extremely lean mixtures which, in general, allows for better fuel economy, higher engine efficiency and for lower combustion temperatures, which in turn leads to a reduction of NOx emissions and of the heat transfer to the wall. This property together with the high flame propagation speed of hydrogen-air mixtures allows various load control strategies, such as power regulation by varying the equivalence ratio, similarly to the load control in diesel engines, avoiding to resort to a throttle valve (at least for medium to high loads, as discussed in the following), thus avoiding throttling losses, with the possibility to obtain extremely lean combustion processes. As depicted in *Figure 1-1*: hydrogen and gasoline laminar flame speed

, where the solid lines represent the laminar flame velocity for different mixtures of air and hydrogen and the dashed line represents a least squares fit polynomial between experimental data related to a mixture of air and gasoline, at each equivalence ratio the H_2 flame speed is higher than the gasoline one: passing from stoichiometric to lean mixtures, the flame speed decreases significantly but still remaining so high not to require turbulence enhancing methods (if considering the combustion only, without accounting for the mixing process).

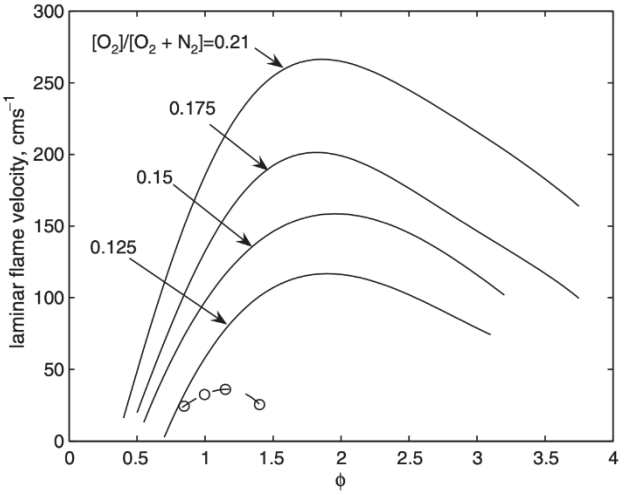

Figure 1-1: hydrogen and gasoline laminar flame speed

Apart from the abovementioned advantages provided by the high hydrogen flame speed, further interacting characteristics have to be considered: hydrogen features a small quenching distance, i.e. 0.64 mm at stoichiometry versus 2 mm of gasoline, and a very low minimum ignition energy, i.e. 0.02 mJ at $p = 1\ bar$ and $T = 298\ K$ versus 0.24 mJ of gasoline in the same conditions. The high flame propagation speed together with the low minimum ignition energy implies the risk of pre-ignition and backfire, since the hot gases and hot spots in the cylinder can easily serve as sources of ignition. A preignition event causes the mixture to burn mostly during the compression stroke, i.e. to advance the start of combustion (SOC), the temperature in the combustion chamber increases, i.e. the heat release rate (HRR) increases, thus causing the hot spots that led to the preignition event to further increase their temperature, with the risk of an even earlier preignition events, i.e. to further advance SOC, in the following cycles. On the other hand, such values of minimum ignition energy lead to the possibility to run the engine lean ensuring prompt ignition. The small quenching distance implies a risk of backfire as well: by considering a PFI application, being a hydrogen-air mixture able of easily passing a nearly closed intake valve, if the combustion in the piston top-land persists up to the intake valve opening (IVO) or if preignition events led to advance SOC to a great extent cycle after cycle, it can ignite the fresh charge and the flame can propagate towards the intake port and eventually the intake manifold, causing a pressure rise which can damage or destroy the intake system.

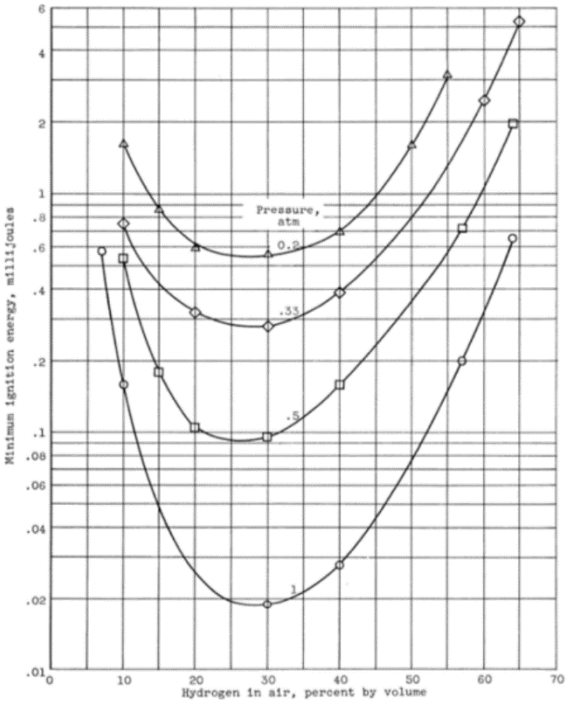

Figure 1-2: hydrogen minimum ignition energy

In general, preignition and backfire are the most significant phenomena bounding the choice of the equivalence ratio towards lean mixtures, which is possible due to the hydrogen flammability limits, in turn meaning to limit the engine output power. In fact, it is extremely difficult to operate the engine with a stoichiometric mixture without encountering frequent preignition events. The risk of such abnormal combustion events can be reduced through

several strategies such as: charge cooling, the adoption of water-cooled spark plugs, the implementation of variable valve timing (VVT) or variable valve actuation (VVA) for effectively scavenging the exhaust gases, the use of direct injection (DI) rather than PFI. These strategies are aimed at contemporarily reducing the occurrence of these phenomena and increasing the engine output power: for instance, if DI is implemented, it is possible to contemporarily eliminate the risk of backfire and to increase the engine output power with respect to PFI, both effects attributable to the fact that the fuel can be injected when the intake valves are closed. Thus, the enflamed charge won't travel back in the intake system and the volumetric efficiency is improved a lot: in this way, it is possible to resort to richer mixtures and so to increase the theoretical engine output power. However, at stoichiometric air-fuel ratio, the combustion temperature is very high and so a large amount of NOx is produced, also increasing the risk of preignition, that is still possible with DI. It is possible to reduce the NOx emissions and to increase the engine power output by resorting to the abovementioned countermeasures and by implementing proper load control strategies, as detailed in the following.

As far as pollutant emissions are concerned, the combustion of H_2 with O_2 produces only water; however, in internal combustion engines the hydrogen is burned with air that, as known, contains 78% N_2 by volume and therefore nitrogen oxides are produced too. NOx are mainly produced due to the very high temperatures of the combustion chamber during the combustion process. Due to this fact and to the previously made considerations, the extent of NOx formation depends, among other factors, on the air-fuel ratio, compression ratio, engine speed, ignition timing and on the use of dilutant such as EGR.

In addition to NOx, near-to-zero amount of CO, CO_2 and unburned HC can be measured due to the fast oil burning in the combustion chamber.

The engine efficiency and the NOx emissions are the two main parameters on the base of which the load control strategy is determined. When possible, wide-open throttle (WOT) operation is used due to the increased engine efficiency: this can be done by regulating the load through the variation of the equivalence ratio, i.e. the amount of fuel injected, rather than by throttling, thus reducing pumping losses. Across the load range of the engine, different control strategies can be implemented. NOx production is dependent on the equivalence ratio, being it the parameter with the greatest impact on the maximum combustion temperature, as depicted in *Figure 1-3*. At lean mixtures, NOx production is very low until the so called "NOx formation limit", occurring normally at around $\Phi = 0.5$, is reached. Richer mixtures produce high levels of NOx and a maximum is reached at about $\Phi = 0.8 - 0.95$ depending on the compression ratio. In particular, higher values of CR generally produce higher maximum level of NOx at lower values of Φ. Thus, the need to keep NOx emissions low and, as previously mentioned, to reduce as much as possible the risk of preignition and backfire events, bound the choice of the equivalence ratio towards lean mixtures: the problem is that such lean mixtures lead to a reduction of the maximum engine output power. However, it is possible to keep NOx production low and to contemporarily increase the engine output power by resorting to a dilution with EGR, intended to decrease the temperatures reached in the combustion chamber, combined with exhaust gas aftertreatment systems, such as TWC and LNT, allowing to enrich the mixture towards Φ values which are closer to stoichiometric conditions. In addition, also turbocharging is considered a suitable solution to improve the lean power density by pressure boosting. As far as the engine load control strategy is concerned, it is needed to distinguish between idling/very low loads and higher load values. For idling and very low loads, the mixture is extremely lean and this leads to a very high indicated mean effective

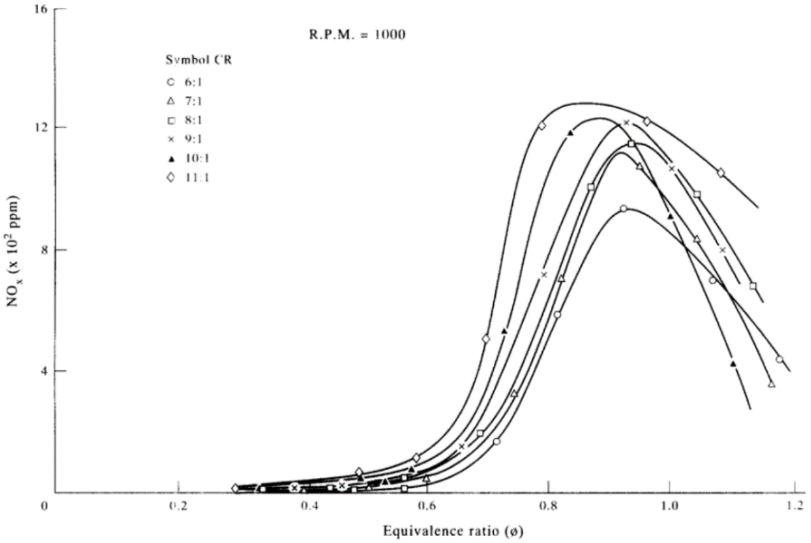

Figure 1-3: NOx emissions as a function of the equivalence ratio

pressure coefficient of variation (CoV_{imep}), in turn leading to lower combustion velocity and combustion stability due to the large amount of unburned hydrogen that would result from these conditions: for these reasons, at such loads, throttle control is used to enrich the mixture to limit the abovementioned issues. At higher loads, different strategies can be implemented. For example, it is possible to resort to throttled stoichiometric operation with a LNT, as far as the gaseous hydrogen present in the exhaust gas at stoichiometric conditions is a very efficient reducing agent. To increase the engine efficiency by reducing pumping losses, instead of throttling, EGR with a concentration ranging from 0% to 50% can be used to control the amount of fresh air in the engine. If the engine is turbocharged, for loads above the naturally aspirated (NA) WOT limit, control is possible by regulating the boost pressure while keeping a stoichiometric mixture.

As far as gaseous hydrogen storage is concerned, being it a gas with extremely low density, i.e. 0.089 kg/m^3 at p=1 bar and T=273 K, that is one order of magnitude lower than NG, a proper driving range can be achieved only by resorting to very high compression, i.e. p=700 bar. Another possibility, similarly to natural gas (CNG vs LNG), is to store the fuel in liquid form: the primary advantage of storing H_2 as a liquid is the higher energy density that can be kept on-board since, despite its lower heating value, that is 120 MJ/kg, compared to the 44 MJ/kg of gasoline, the very low hydrogen density with its stoichiometric air-fuel ratio, that is 34.5, leads to lower energy content with respect to gasoline. In any case, liquid storage implies the challenges of facing the energy penalty of hydrogen liquefaction, evaporation during long-term storage and the cost of on-board cryogenic dewars.

To conclude the section about the use of hydrogen as a fuel in internal combustion engines, it is worth to briefly discuss the question related to the attainable thermal efficiencies in such machines. The hydrogen RON (≥ 130), which is higher than the gasoline one and comparable to the one of NG, and its lower flammability limit are the characteristics that allow hydrogen-fueled engines to reach high thermal efficiencies. In *Figure 1-4*, it is presented a comparison between the brake thermal efficiencies as a function of the brake mean effective

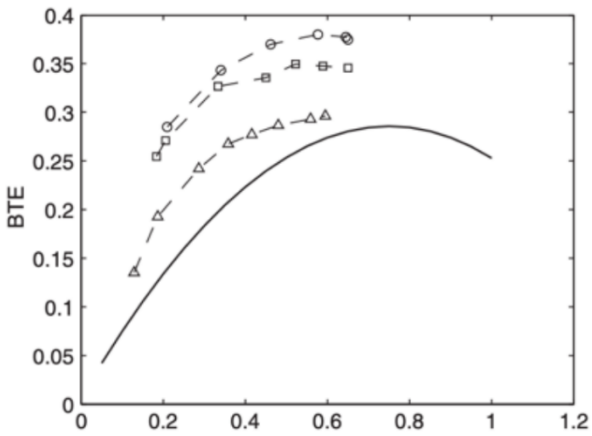

Figure 1-4: brake thermal efficiency as a function of bmep

pressure, evaluated in the same engine, of hydrogen and gasoline at different compression ratios. In particular, the bmep is normalized as $BMEP^* = BMEP/BMEP_{max,gasoline}$, ∘ and □ are related to hydrogen with CR=14.5 and CR=12.5 respectively; △ and – are related to hydrogen and gasoline respectively, with CR=9. It is noticeable that, if considering H_2 fueling, it is possible to attain higher efficiency for increasing values of compression ratio and to obtain higher efficiencies with respect to gasoline fueling at the same CR; the maximum efficiency is achieved at medium loads. The difference in the relative efficiency between hydrogen and gasoline at low loads in due to the need for throttling that, as previously mentioned, is implemented to limit the amount of unburned hydrogen that would be emitted with unthrottled operations at ultra-diluted conditions. The drop-off at high loads is due to increasing heat transfer losses. It has been shown that the heat lost to cylinder walls increases monotonically with increasing equivalence ratio due to the greater flame velocity, higher flame temperature (that is the same reason why NOx production increases at higher values of Φ) and decreasing quenching distance, which leads to narrow the thermal boundary layers. In fact, it has been found that at $\Phi = 0.4$ the energy lost by heat transfer to the walls accounted for 25% of the total heat release, while at $\Phi = 1$ the percentage increases to 45%. The conclusion is that, to improve H_2 engines' thermal efficiency, it is necessary to look for strategies allowing to minimize heat transfer losses to cylinder walls, such as charge stratification.

2. Combustion diagnostics in spark ignition engines

Combustion diagnostics in internal combustion engines refers to a procedure that starts from experimental data which must be investigated, interpreted and managed to extract detailed information about the combustion process; to this purpose, alongside the availability of experimental data, a model of the combustion system has to be defined as well. Combustion diagnostics in spark ignition internal combustion engines is said to be "pressure-based", since the primary experimental data to refer to is the in-cylinder pressure trace, that is the in-cylinder pressure time history that can be recorded during the real engine operation.

2.1. Single zone heat release analysis

This approach, which is based on the first law of thermodynamics for open systems and considers the combustion chamber content as a single zone, allows to extract from the in-cylinder data the heat release rate (HRR), that is the rate at which the chemical energy of the charge is released during the combustion process. The HRR is related to the in-cylinder pressure and to the instantaneous in-cylinder volume with parameters depending on the thermal capacity at constant volume and the ideal gas constant. By referring to the system depicted in *Figure 2-1* and applying the first law of thermodynamics for open systems:

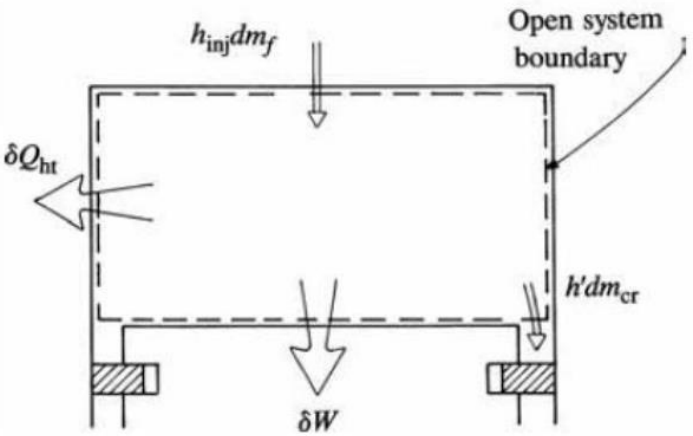

Figure 2-1: open system boundaries for the combustion chamber

(2.1) $$\delta Q_{ch} - \delta Q_{ht} = dU_s + \delta W + \sum_i h_i dm_i$$

The change in sensible energy of the charge dU_s is separated from the energy change due to the composition modification produced by the combustion: δQ_{ch} represents the chemical energy released by the combustion. $\delta W = pdV$ is the piston work and δQ_{ht} is the heat transfer to the combustion chamber walls. The mass flux term represents the flow across the system boundary and includes the flow into and out of the crevice regions, which is often neglected.

Assuming that $U_s = mu(T)$, being T the mean charge temperature and m the mass within the system boundaries, then:

(2.2) $$dU_s = mc_v(T)dT + u(T)dm$$

It is important to underline that the mean temperature determined from the ideal gas law is close to the mass-averaged in-cylinder temperature during combustion because the molecular weights of burned and unburned gases are basically the same. By neglecting the crevice flow, $dm = 0$, and by putting (2.2) into (2.1):

(2.3) $$\delta Q_{ch} - \delta Q_{ht} = mc_v(T)dT + pdV$$

By introducing the ideal gas law:

(2.4) $$\delta Q_{ch} - \delta Q_{ht} = \frac{c_v}{R} d(pV) + pdV = \frac{c_v}{R} Vdp + \frac{c_v}{R} pdV + pdV$$

And so:

(2.5) $$\delta Q_{ch} - \delta Q_{ht} = \frac{c_v}{R} Vdp + \frac{c_p}{R} pdV$$

Being the heat release rate referred to the crank variation, in the end it is obtained the following expression:

$$AHRR = \frac{dQ_{ch}}{d\theta} - \frac{dQ_{ht}}{d\theta} = \frac{1}{\gamma-1} V \frac{dp}{d\theta} + \frac{\gamma}{\gamma-1} p \frac{dV}{d\theta} \tag{2.6}$$

Now, some clarifications are needed. The apparent heat release rate $AHRR = \frac{dQ_{net}}{d\theta}$ is the net heat released during the combustion process and it is equal to the difference between the chemical energy released by the fuel and the heat transferred to the wall. It is clear that it can be calculated with (2.6) by knowing the in-cylinder pressure and the in-cylinder volume. On the other hand, the heat release rate $HRR = \frac{dQ_{ch}}{d\theta}$, that is the chemical energy released during the combustion, i.e. the gross heat released, can be calculated only if the term related to the heat transferred to the walls, $\frac{dQ_{ht}}{d\theta}$, is modeled.

According to these considerations, the integral of the gross heat release rate during the whole combustion process should be equal to the injected fuel mass multiplied by its lower heating value and it is called heat release (HR):

$$HR = \int_{SOC}^{EOC} dQ_{ch} = m_{f,inj} Q_{LHV} = \int_{SOC}^{EOC} \frac{1}{\gamma-1} V dp + \int_{SOC}^{EOC} \frac{\gamma}{\gamma-1} p dV + \int_{SOC}^{EOC} dQ_{ht} \tag{2.7}$$

Therefore, the percentage of the energy released by the combustion, which is referred to as "mass fraction burned" x_b, and that should be equal to 1 at EOC, is defined as:

$$x_b(\theta) = \frac{\int_{SOC}^{\theta} \frac{1}{\gamma-1} V dp + \int_{SOC}^{\theta} \frac{\gamma}{\gamma-1} p dV + \int_{SOC}^{\theta} dQ_{ht}}{m_{f,inj} Q_{LHV}} \tag{2.8}$$

However, in many practical applications, the term related to the heat transferred to the walls is neglected and the integral of the apparent heat release rate is normalized so that to give $x_b = 1$ at EOC:

(2.9) $$AHR = \int_{SOC}^{EOC} dQ_{net} = \int_{SOC}^{EOC} \frac{1}{\gamma-1} Vdp + \int_{SOC}^{EOC} \frac{\gamma}{\gamma-1} pdV$$

And so:

(2.10) $$x_b(\theta) = \frac{\int_{SOC}^{\theta} \frac{1}{\gamma-1} Vdp + \int_{SOC}^{\theta} \frac{\gamma}{\gamma-1} pdV}{\int_{SOC}^{EOC} dQ_{net}}$$

In *Figure 2-2*, the typical trend of x_b as a function of θ is reported. The crank angles at which the mass fraction burned (or the energy released by the combustion) is equal to 10%, 50% and 90% are normally used to characterize the combustion and they are referred to as MFB10, MFB50 and MFB90, respectively.

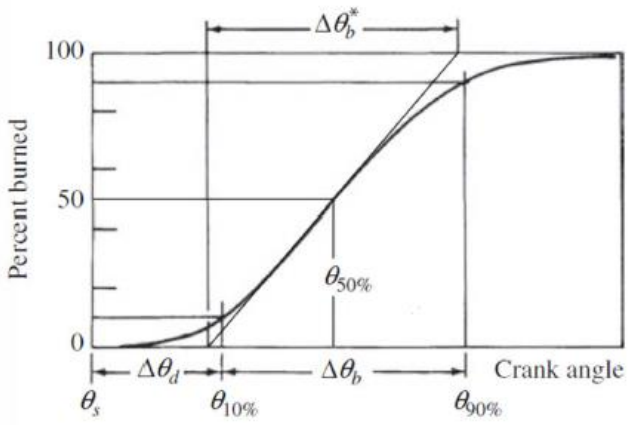

Figure 2-2: mass fraction burned as a function of crank angle

MFB10 represents an angle at which the flame development has completed ($\Delta\theta_d$= flame development angle) and the combustion through flame propagation can occur. MFB90 represents the angle at which the combustion process can be considered concluded, that is not set at $x_b = 1$ because in real experimental data usually x_b does not reach the ideal plateau that the curve displays when approaching $x_b = 1$. The crank angle interval between MFB10 and MFB90, $\Delta\theta_b$, is referred to as "rapid burning angle" and its typical value in spark ignition engines is about 60 CA°. MFB50, also referred to as "anchor angle", is the crank angle at which half of the fuel mass has burned and represents a sort of gravimetric center of combustion. It is used to characterize the phasing of the combustion process and, for a wide range of engine and operating conditions, MFB50 at maximum brake torque (MBT) timing occurs from 5 CA° to 7 CA° aTDC (after top dead center).

It is possible to define a combustion retard parameter as: $MFB50 - MFB50_{MBT}$. This parameter represents the extent, measured in crank angle degrees, to which the center of combustion process has been shifted from the crank angle at which the maximum torque is

developed and it has been found to be able to well correlate the effects of retarding the combustion process for different engines, fuels, air-fuel ratios, compression ratios, intake pressures and spark timings.

2.2. Multizone burning rate analysis

By means of the previously exposed single zone analysis, it is possible to evaluate the heat release rate HRR and the mass fraction burned x_b. If in-cylinder pressure and volume are available and x_b has been evaluated, it is possible to estimate the mass of burned and unburned gas and then, by applying the ideal gas law, it is possible to estimate a temperature. The point is that it is an average temperature, since only a single zone has been considered, and no distinction has been made between burned and unburned gas temperatures which, on the contrary, have to be distinguished. For this reason, a more refined approach can be implemented, that is the multizone burning rate analysis.

If considering a specific crank angle during the combustion process, the combustion chamber can be split in two big regions, the unburned gas one and the burned gas one. These two regions are separated by the flame front that, in this modelling approach, is not considered as a corrugated flame front but as a surface, in particular the portion of a sphere (the blue one in *Figure 2-3*), defined so that burned gas and unburned gas volumes are equal to the real ones at the considered crank angle. The burned gas region is in turn subdivided into several zones: the burned gas temperatures at a specific crank angle are not homogeneous, since the first particles involved in the combustion, that are the ones closest to the spark plug, reach higher temperatures because they are burned and then compressed by the gas particles which burn

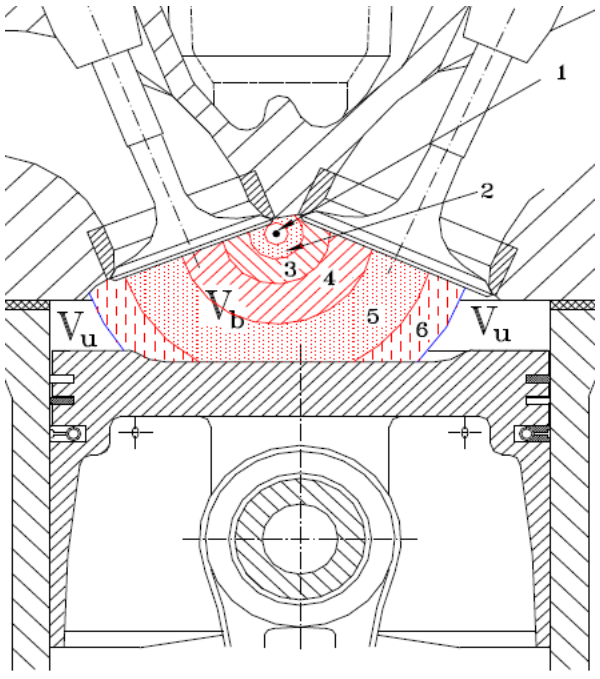

Figure 2-3: multizone analysis

later and expand. Therefore, in the combustion chamber, there is a temperature gradient with values decreasing with the distance from the spark plug. Since, as explained later on, independently from the chosen number of burned gas zones, each zone bores at a specific crank angle, even if at the end of the process there will be n zones, at each considered crank angle there is a different number of zones.

The first two equations of this model are the volume conservation and the mass conservation ones:

(2.11) $$dV = dV_u + \sum_{i=1}^{n-1} dV_{b,i} + dV_{b,n}$$

(2.12) $$dm = d\left(m_f + m_a + m_r\right) = dm_u + dm_{b,n} = 0$$

The combustion chamber volume is equal to the sum of the volumes of the regions in which it has been split, the unburned one and the burned ones.

The combustion chamber mass is equal to the sum of air, fuel and residual masses, equal to the sum of the mass of the unburned gas and the mass of the last zone of burned gas. Only the last zone is considered because it is assumed that, as soon as a new zone appears, it becomes the only one whose mass changes due to the grow of the mass of burned gas, while the previous zones keep having the same mass of burned gas they had when a new zone born (in any case, pressures and temperatures still vary). Moreover, (2.12) is equal to zero because, during the combustion, what changes is the mass of burned and unburned gas, but the overall charge mass does not change.

Then, being $x_b = m_b/m$, the masses of burned and unburned gas can be expressed as:

(2.13) $$m_b = x_b m$$

(2.14) $$m_u = (1 - x_b)m$$

In addition:

(2.15) $x_b = \sum_{i=1}^{n} x_{b,i}$

Where $x_{b,i} = m_{b,i}/m$.

The other equations of the model are the energy equations for all the considered zones, which are one for the unburned zone, n-1 for the burned zones but the last one and one for the nth burned zone.

(2.16) $-q_u A_u \frac{\partial \theta}{\omega} + V_u dp = (1 - x_b) m dh_u$

(2.17) $-q_{b,i} A_{b,i} \frac{\partial \theta}{\omega} + V_{b,i} dp = m x_{b,i} dh_{b,i}$

(2.18) $-q_{b,n} A_{b,n} \frac{\partial \theta}{\omega} + V_{b,n} dp = m x_{b,n} dh_{b,n} + m dx_b, n(h_{b,n} - h_u)$

The first term in all the equations represents the heat transfer to the walls where q is the heat flux of the considered zone and A is the corresponding surface which only accounts for the portions of the zones which are in contact with the walls.

Concerning the enthalpy-related terms, in (2.16) and (2.17) there is no mass exchange between the ith burned zone and the unburned one, the chemical composition does not change and therefore it is possible to write $dh_u = c_{p,u} dT_u$ and $dh_{b,i} = c_{p,b,i} dT_{b,i}$. In (2.18), since it has been said that the last zone n is the only one that exchanges mass with the unburned zone, there are two enthalpy terms: the first one is $dh_{b,n} = c_{p,b,n} dT_{b,n}$ and is related only to the enthalpy of the nth zone burned gas, the second one is $m dx_b, n(h_{b,n} - h_u)$ and is related to the mass exchange between the burned zone n and the unburned zone, which causes the chemical composition of zone n to vary, that is the reason why it is needed

to account for the enthalpy difference between burned gas of zone n and unburned gas. By analyzing the equations (2.16), (2.17) and (2.18), it appears that there are n+2 unknowns, i.e. $x_{b,n}$ (and consequently x_b, since it is given by the sum of the mass fraction burned in each zone), T_u, $T_{b,i}$ (which are n-1 temperatures) and $T_{b,n}$, for n+1 equations. This means that, to close the problem, an additional equation is needed: this is the equation expressing $x_{b,n}$, that is derived starting from the in-cylinder volume equation:

$$x_{b,n} = \frac{\frac{V}{m} - [(1-x_b)v_u + \sum_{i=1}^{n-1} x_{b,i} v_{b,i}]}{v_{b,n} - v_{b,u}} \tag{2.19}$$

The heat flux terms q are not unknowns because they are calculated by means of a sub-model in which they are a function of the temperature of the zone and of the heat transfer coefficient h:

$$q = h\left[T - T_w + K\frac{D}{v_p}\frac{d(T-T_w)}{dt}\right] \tag{2.20}$$

T_w is the wall temperature and it can be estimated through experimental correlations available in the literature, if the coolant temperature is known. v_p is the mean piston speed, D is the bore diameter and K a dimensionless quantity to be calibrated. The heat transfer coefficient h is expressed through a specific model, the well-known Woschni correlation, in which it depends on several known parameters and the only unknown is the temperature of the considered zone. According to these considerations, q contains only the unknown temperature of the considered zone, that has already been included in the previously exposed unknown count.

Resuming, by means of a single zone model it is possible to calculate HRR and x_b, while introducing a multizone model it is possible to calculate q and T of each zone as well. Due to this reason, since the level of NOx strongly depends on the temperature and the oxygen availability, if it is needed to model NOx formation, a multizone approach has to be used: since a fixed operating conditions is considered, the oxygen level does not change and so NOx formation depends only on the temperature. The real temperature in the burned gas zone is difficult to be experimentally measured and therefore it is estimated through a model in which it depends on the number of zones that has been selected. So, to determine a suitable maximum number of zones, a starting maximum number of zones is assumed, the model is applied to obtain the temperature of each burned gas zone and consequently, in the way which will be exposed later, to estimate the NOx level for each zone. Then, the average values of NOx over the considered number of zones are calculated: these values should match the experimental data. It follows that an iterative procedure must be followed to find a suitable maximum number of zones. In general, in SI engines, the maximum number of zones allowing to obtain accurate results ranges from 6 to 20.

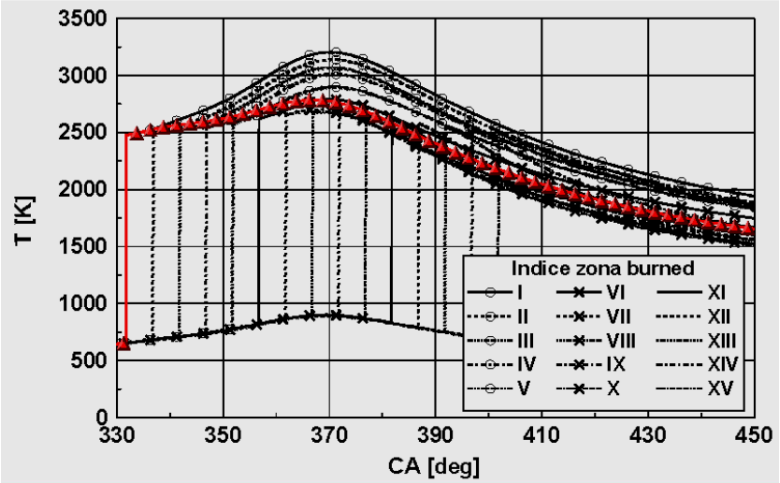

Figure 2-4: temperatures calculation in multizone analysis

As far as NOx formation is concerned, in SI engines the main responsible is the thermal mechanism, that can be described by means of different chemical reactions, the most important of which are presented below:

(2.21) $N_2 + O \rightarrow NO + N$

(2.22) $N + O_2 \rightarrow NO + O$

(2.23) $N + OH \rightarrow NO + H$

(2.24) $H + N_2O \rightarrow N_2 + OH$

(2.25) $O + N_2O \rightarrow N_2 + O_2$

(2.26) $$O + N_2O \rightarrow NO + NO$$

Moreover, it has been found that the differential equation describing the NO rate of formation is the following one:

(2.27) $$\frac{d[NO]_i}{dt} = 2\left[1 - \left(\frac{[NO]_i}{[NO]_{i,eq}}\right)^2\right]\left(\frac{R_1}{1+\frac{[NO]_i}{[NO]_{i,eq}}\frac{R_1}{R_2+R_3}} + \frac{R_6}{1+\frac{R_6}{R_4+R_5}}\right)$$

The terms R_i are related to the velocities of forward and reverse reactions which, at equilibrium, are equal. For sake of simplicity, it is reported only the one related to equation (2.21):

(2.28) $$R_1 = k_1^+[N_2]_e[O]_e = k_1^-[NO]_e[N]_e$$

k is the constant written according to the Arrhenius expression:

(2.29) $$k = AT^b e^{-\frac{E}{RT}}$$

Where E is the activation energy, R is the universal gas constant, T is the temperature and A and b appears in the so called steric factor. The exponential term indicates that, unless the temperature is sufficiently high if compared with the activation energy, the velocity of the reaction is low. In particular, the first reaction (2.21) has a very high activation energy and, unless a sufficiently high temperature is reached, the reaction is not going to start. Since the first reaction produces the N needed for the following reactions to occur, they won't occur as well.

The differential equation describing the NO rate of formation over time depends on several concentrations, some of which are time dependent, some others are not because they reach extremely fast the equilibrium condition. Actually, most of these factors reaches extremely fast the equilibrium condition, in particular the ones connected to the combustion process (e.g. N_2, O and O_2): they can be considered at equilibrium because there are so many radicals produced during the combustion process that, if few of them are involved in the NO production, they will be immediately replaced by other atoms of the same type produced by the combustion. Then, being the N rate of formation described by means of another differential equation, the only unknown of (2.27) is [NO].

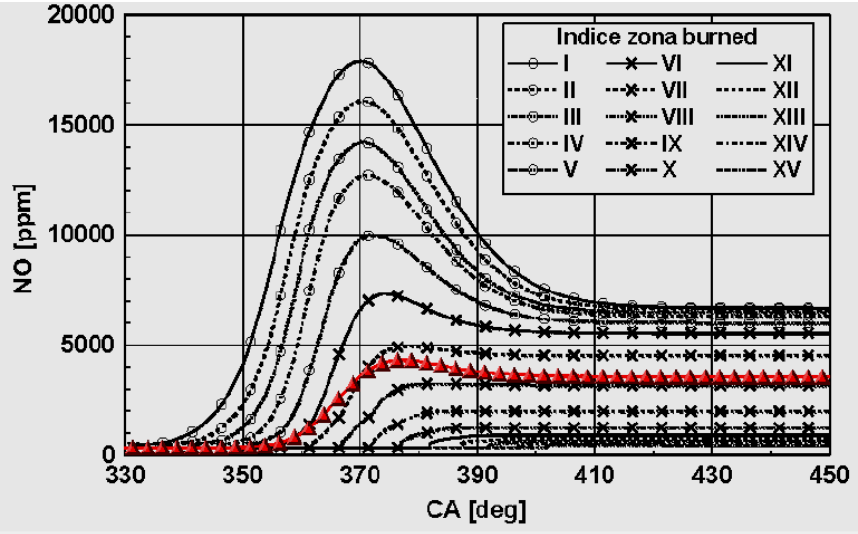

Figure 2-5: NOx concentrations in multizone analysis

The differential equation describing the rate of formation of NO is decoupled from the diagnostic model, since the diagnostic model provides temperature and oxygen concentration for each zone: the described chemical model is applied and the differential equation is solved time step by time step to get, in the end, the time history of NO levels. As previously mentioned, a suitable maximum number of zones is found when the average NO concentration, i.e. the red curve in *Figure 2-5*, matches the experimental data.

Once detailed how the maximum number of zones must be chosen, it still remains to clarify which is the criterion by which the instants at which each zone has to bore are chosen. Several approaches can be used. The simplest and most accurate one consists firstly in launching a single zone simulation of the model to calculate x_b and then in selecting the number of zones to be implemented, information according to which x_b is consistently split. For instance, if the maximum selected number of zones is 10, x_b is split in 10 as well and therefore a new zone bores when x_b increases of 0.1. After that, the NOx levels are calculated as previously explained to assess if the maximum number of zones is suitable or

not. If it is not, another number of zones is chosen and the calculations are performed iteratively, until the average NO levels match the experimental ones.

The last topic to be addressed in the context of the multizone burning rate approach is the flame propagation analysis: in particular, it is needed to estimate the burning speed S_b, the mean expansion speed of the burned gas u_b and the mean speed of the unburned gas ahead of the flame front u_g.

Starting from the available data, the in-cylinder pressure p and the total mass in the combustion chamber m are experimentally available, while the temperature of each burned gas zone $T_{b,i}$, the mass fraction burned of each zone $x_{b,i}$ and the temperature of the unburned gas T_u have been calculated by means of the multizone analysis.

The burning speed can be expressed by means of the following equation:

$$S_b = \frac{dm_b/dt}{\rho_u A_b} \tag{2.30}$$

Since $x_{b,i}$ and m are known, it is possible to evaluate what follows:

$$m_{b,i} = mxb_i \quad \rightarrow \quad m_b = \sum_{i=1}^{n} m_{b,i} \quad \rightarrow \quad dm_b/dt \tag{2.31}$$

Then, by knowing p and T_u it is possible to compute the density of the unburned gas as:

$$\rho_u = \frac{p}{RT_u} \tag{2.32}$$

What is still missing is A_b. As previously explained, V_b is not the real corrugated flame front but a volume of a portion of a sphere, centered in the spark plug, defined so that the volume of burned and unburned gas on its sides are equal to the real one; A_b is the surface corresponding to V_b. Since the temperature of each burned gas region $T_{b,i}$ and the pressure time history p are known, it is possible to estimate the density of each burned gas zone:

(2.33) $$\rho_{b,i} = \frac{p}{RT_{b,i}}$$

$m_{b,i}$ has been calculated in (2.31) and $\rho_{b,i}$ in (2.33) and therefore it is possible to compute the volume of each burned gas zone as:

(2.34) $$V_{b,i} = \frac{m_{b,i}}{\rho_{b,i}}$$

Finally:

(2.35) $$V_b = \sum_{i=1}^{n} V_{b,i}$$

To calculate the surface A_b corresponding to the volume V_b, the corresponding radius r_b is needed. This calculation can be easily made by CAD. So A_b is calculated by coupling the outcome of the previously detailed diagnostic model, i.e. V_b with a CAD model of the combustion chamber in which, for each value of the crank angle, it is derived a look-up table in which, for each possible value of V_b, the corresponding values of A_b and r_b are calculated.

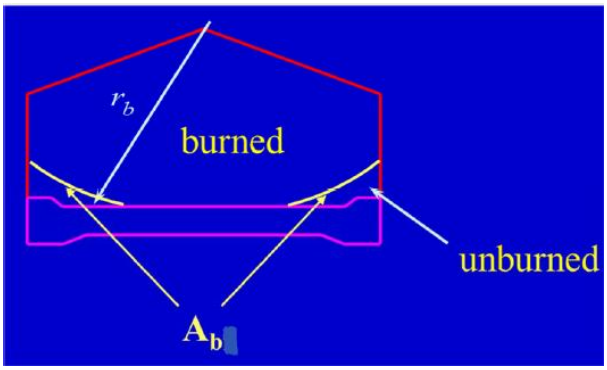

Figure 2-6: combustion chamber scheme

Once calculated S_b, it is possible to calculate the mean expansion speed of the burned gas by means of the following expression:

(2.36) $$\frac{u_b}{S_b} = \frac{\rho_u/\rho_b}{1+x_b\left(\frac{\rho_u}{\rho_b}-1\right)} = \frac{\rho_u}{\rho_b}(1-y_b)+y_b$$

All the terms appearing in such expression are known, except the volume fraction burned y_b, that can be calculated as:

$$y_b = \left[1 + \frac{\rho_b}{\rho_u}\left(\frac{1}{x_b} - 1\right)\right]^{-1} \quad (2.37)$$

Last, the velocity of the unburned gas is calculated by difference:

$$u_g = u_b - S_b \quad (2.38)$$

An example of the results of such analysis are presented in *Figure 2-7*. In the plots at the bottom of the figure, it is represented also a trend of S_L, which is the laminar burning speed that can be estimated by knowing the fuel, the air-fuel ratio, the pressure and the temperature, and S_b. As expected, the burning speed results to be magnified due to the presence of turbulences with respect to S_L. Moreover, this ratio is extremely important because most of the predictive models for combustion, which will be detailed in chapter 3, starts from the prediction of S_b/S_L. It means that the outcome of this diagnostic approach is very useful to validate or to tune any combustion sub-model that can be used in a predictive way.

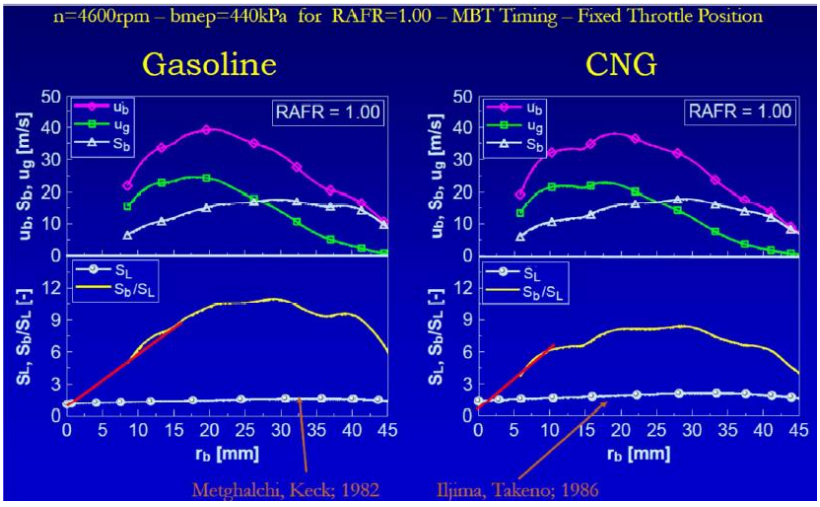

Figure 2-7: analysis of flame propagation

3. Combustion modeling in spark ignition engines

Combustion modeling and combustion diagnostics have got the same thermodynamics background, in the sense that in both cases the combustion chamber is split into a number of burned gas zone and an unburned gas zone, as discussed in chapter 2. The main difference is that, while in combustion diagnostics the in-cylinder pressure time history is experimentally known and it is used to carry out the calculations to characterize the combustion by means of quantities like the mass fraction burned, the temperatures of the different zones, the heat transfer to the walls, the NOx formation and the flame speed, in combustion modeling the pressure is not known and it has to be estimated, by using as input a combustion sub-model that is needed to estimate the mass fraction burned $x_{b,n}$.

In addition to the previously exposed equations (2.16), (2.17) and (2.18), in combustion modeling is also needed the equation for the calculation of the in-cylinder pressure:

$$p = \frac{m}{V}\left[(1 - x_b)R_u T_u + \sum_{i=1}^{n} x_{b,i}\, R_{b,i} T_{b,i}\right] \tag{3.1}$$

As mentioned, to calculate the pressure, it is needed a combustion sub-model. Combustion sub-models, which are detailed in the following, can be divided into models in which the combustion process is specified as input, like the Wiebe function, and models which predict the rate of fuel burning, like the entrainment-based burning law and the fractal approach. These last assume that the overall flame shape is approximated as a portion of a sphere centered at the spark plug. In addition, it is important to describe the different phases of the combustion process from the basic flow and the critical flow features by means of the in-cylinder turbulences. The dependency of the flame chemistry on air-fuel ratio are incorporated into the mixture's laminar flame speed.

3.1. Wiebe function

The Wiebe function is a combustion sub-model in which the burning rate is imposed. Since the typical shape of the curve related to the mass fraction burned is well-known, it has been found that it can be satisfactorily expressed by means of the Wiebe function:

$$x_b = 1 - \exp\left[-a\left(\frac{\theta-\theta_{SOC}}{\Delta\theta}\right)^{m+1}\right] \tag{3.2}$$

In this expression there are two parameters that are experimentally based, i.e. the start of combustion crank angle θ_{SOC} and the combustion duration $\Delta\theta$, and two coefficients a and m, that has to be identified. In particular, to properly identify this expression, a database of experimental data is needed: if an engine has to be simulated in several operating points, for each point θ_{SOC} and $\Delta\theta$ are needed, and the abovementioned coefficients have to be tuned so that the outcome of the Wiebe function matches the outcome of the diagnostic approach.

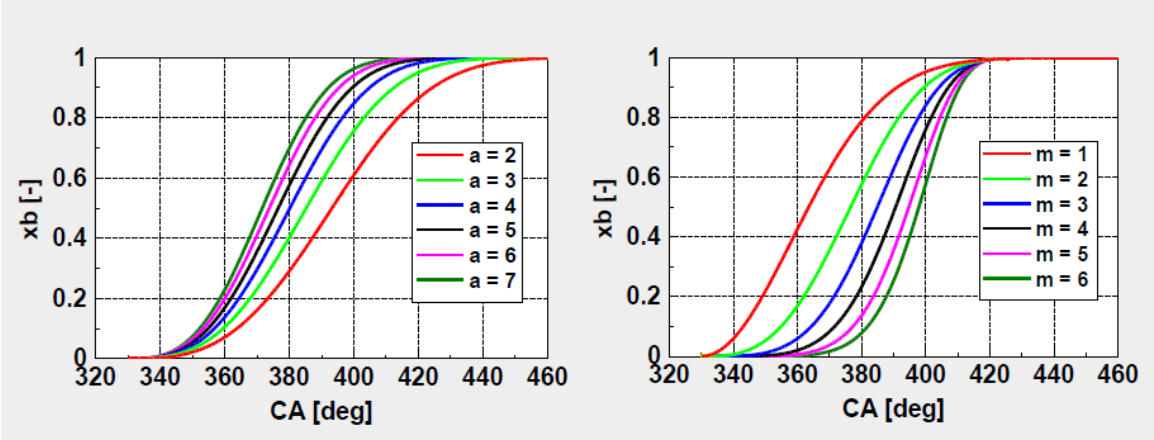

Figure 3-1: Wiebe function parameters' tuning

The effect of the coefficients a and m on the shape of the curve is depicted in *Figure 3-1*.

This approach, that is combustion-imposed, is based on the assumption that any change in the engine under investigation does not significantly affect the combustion process. The Wiebe function is very useful for certain applications, e.g. turbomatching and performance-oriented analyses, and it is widely used in the literature.

3.2. Entrainment-based burning law

Before starting to discuss such combustion sub-model, it is worth to briefly recall the structure of a turbulent SI engine flame.

The actual combustion process, in spark ignition engines, takes place in a turbulent flow field. The turbulent flame is a wrinkled thin reaction sheet laminar flame. In *Figure 3-2* it is possible to see the average leading and trailing boundaries of the flame, which are the black solid lines, with the wrinkled flame sheet in between (with a thickness of 0.1-0.2 mm) and the mean flame location, that is the dashed line. The average distance between the leading and the trailing boundaries of the wrinkled laminar flame is called turbulent flame brush (with a thickness of 1-2 mm). The mean flame contour moves forward into the unburned mixture ahead of the flame at the turbulent flame speed S_b (in *Figure 3-2* it is called S_T) while locally, each part of the wrinkled rection-sheet flame, moves normally into the unburned mixture ahead of it at the laminar flame speed S_L.

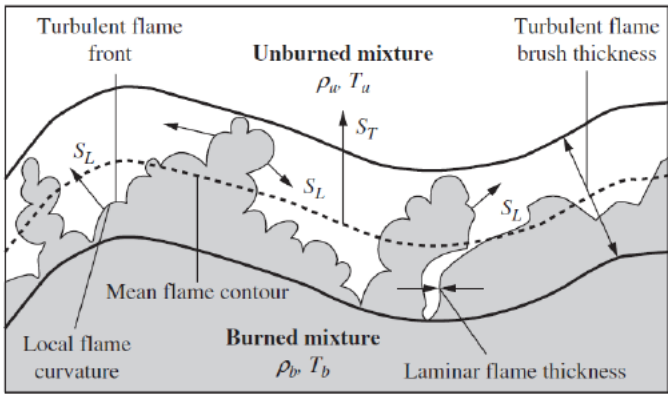

Figure 3-2: structure of the turbulent SI engine flame

Back to the entrainment-based burning law, it is assumed that the unburned mixture is entrained into the thick turbulent flame brush and that, as the unburned mixture crosses the flame surface, a portion burns immediately and another portion burns within the turbulent brush. This last portion forms peninsulas/islands, each of which is surrounded by a thin reaction sheet, and these inclusions burn at a rate determined by their characteristic size and local burning velocity S_L.

According to these considerations, the mixture burning rate is made up of two contributions: the laminar flame propagation and the burning of the mass entrained in the turbulent brush that still has to burn:

$$\frac{dm_b}{dt} = \rho_u A_f S_L + \frac{m_e - m_b}{\tau_b} \tag{3.3}$$

Where A_f is the flame front area, i.e. the spherical surface of radius r_f coinciding with the leading edge of the flame, and m_e is the mass entrained into the turbulent flame brush that still has to burn. τ_b is the characteristic time that has to be determined so as to apply this combustion sub-model.

The second term of (3.3) can be justified by considering that the entrained unburned mixture crosses the flame surface for two reasons: on one side, due to the molecular diffusion of the laminar reaction-sheet, which propagates the reaction-sheet flame forward at the laminar burning speed S_L, and on the other side due to the turbulent convection, that displays a characteristic transport speed u_T:

$$\frac{dm_e}{dt} = \rho_u A_f S_L + \rho_u A_f u_T (1 - e^{-\frac{t}{\tau_b}}) \tag{3.4}$$

Where u_T is the turbulent entrainment speed and $\tau_b = L_T/S_L$ is the characteristic burning time of the yet-to-burn mixture entrained into the flame brush, being L_T the characteristic length scale of the turbulent fluid motion. The exponential term allows for the flame early development flame, that is the time needed to the laminar flame to develop into a turbulent flame. According to these considerations, the mass within the turbulent flame brush is given by:

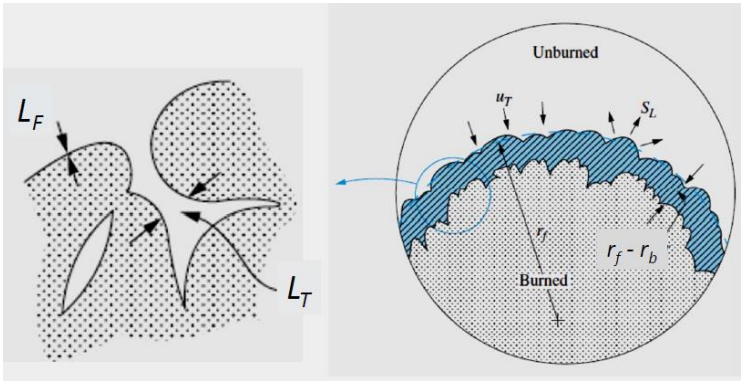

Figure 3-3: turbulent flame brush

$$m_e - m_b = \rho_u (V_f - V_b) \tag{3.5}$$

The scale of the unburned mixture pockets within the flame, depicted in *Figure 3-3*, is given by:

(3.6) $$L_T = \frac{V_f - V_b}{A_L - A_f}$$

Where A_L is the laminar burning area, that is the surface area that the flame would had if it burned locally at the laminar flame speed, which is formally identical to the definition of A_b given in (2.30):

(3.7) $$A_L = \frac{dm_b/dt}{\rho_u S_L}$$

Then, putting together (3.5) and (3.6):

(3.8) $$m_e - m_b = \rho_u (V_f - V_b) L_T$$

If dividing (3.8) by the characteristic burning time of the yet-to-burn mixture entrained into the flame brush, the second term of (3.3) is thus obtained.

To resume, the main equations of this combustion sub-model, whose meaning and derivations have been explained earlier, are the following ones:

(3.3) $$\frac{dm_b}{dt} = \rho_u A_f S_L + \frac{m_e - m_b}{\tau_b}$$

(3.4) $$\frac{dm_e}{dt} = \rho_u A_f S_L + \rho_u A_f u_T (1 - e^{-\frac{t}{\tau_b}})$$

3.3. Fractal model

As previously explained, A_L is the surface of the actual corrugated flame front, which is actually a thin wrinkled laminar flame sheet which moves orthogonally with respect to the unburned gas at the laminar flame speed S_L; A_b is a surface defined as a portion of a sphere centered in the spark plug so that the volumes of burned and unburned gases comprised between A_L and A_b result to be equal.

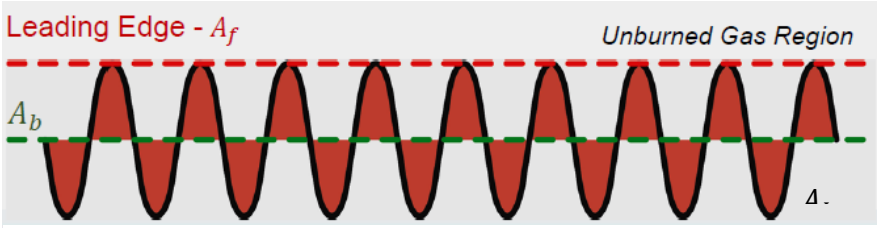

Figure 3-4: flame front characteristic surfaces

According to such geometric considerations, it is possible to write down the rate of change of the burned gas mass with time as:

$$\frac{dm_b}{dt} = \rho_u S_L A_L = \rho_u S_b A_b \tag{3.5}$$

Consequently:

$$\frac{S_b}{S_L} = \frac{A_L}{A_b} \tag{3.6}$$

This last equation indicates the fact that $S_b > S_L$ due to the corrugation effect given by the turbulences. The fractal approach aims at directly modeling the ratio given by (3.6):

$$\frac{S_b}{S_L} = \frac{A_L}{A_b} = \left(\frac{\varepsilon_o}{\varepsilon_i}\right)^{D-2} \tag{3.7}$$

The ratio between turbulent and laminar flame speed is modeled as the ratio between two characteristic lengths, which will be defined in the following, to the power of a function of D, that is called fractal dimension. This means that the underlying hypothesis of this model is that the geometry of a corrugated flame front is fractal. A fractal geometry, like illustrated in the Kock curve depicted in *Figure 3-5*, is a structure that exhibits similar patterns at increasingly smaller scales, according to a property which is called "self-similarity".

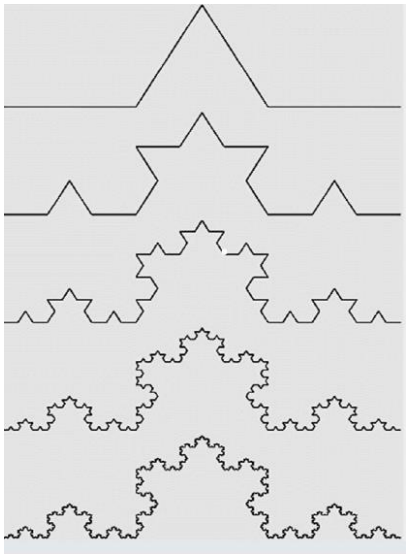

Figure 3-5: Kock curve

The fractal dimension D applied to the fractal combustion sub-model is not actually a constant as the rigorous mathematical definition would require, but it is a function of the corrugation effect, recalling that u' is the turbulence intensity:

(3.8) $$D = \frac{2}{1+\frac{u'}{S_L}} + \frac{2.35}{\frac{S_L}{u'}}$$

If $S_L = u'$, the corrugation effect is very small, if $u' \gg S_L$, the corrugation effect is much more significant and consequently the fractal dimension of the corrugated flame front will change.

The outer and inner cutoff length scales, that are the two length scales between which the flame geometry can be considered fractal, can be defined as the integral and the Kolmogorov length scale of turbulences, respectively:

(3.9) $$\varepsilon_o = L_i = C_L(h_{min} + S_P)$$

(3.10) $$\varepsilon_i = \eta = L_i \left(\frac{u' L_i}{\nu}\right)^{-\frac{3}{4}}$$

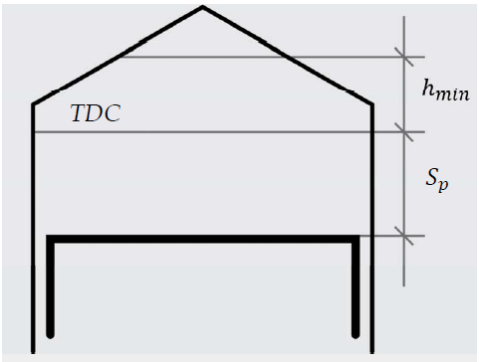

Figure 3-6: combustion chamber characteristic dimensions

The expression of ε_i directly comes from the Kolmogorov theory; on the other hand, ε_o, that is equal to the integral length scale, is a function of the maximum geometrical dimensions of the combustion chamber by means of characteristics dimensions, as depicted in *Figure 3-6*, being $h_{min} = const$ and $S_P = S_P(\theta)$; C_L is a parameter that has to be tuned so that to match the experimental data.

By substituting (3.9) and (3.10) in (3.7), it is obtained the following equation:

$$\frac{S_b}{S_L} = \left\{ \frac{C_L(h_{min}+S_P)}{C_L(h_{min}+S_P)\left[\frac{u' C_L(h_{min}+S_P)}{\nu}\right]^{-\frac{3}{4}}} \right\}^{D-2} \tag{3.11}$$

It is important to notice that, in order to correctly estimate the ratio expressed by the equation (3.11), it is needed to know the quantity u', that appears explicitly at the denominator and implicitly in the exponent D; this fact is similar to what happens in the entrainment based burning law, in which it is needed to estimate u_T, which is set equal to u' as a first approximation. This means that these models, aiming at simulating and reproducing the effects of turbulences on the flame front, need as input a turbulence-related characteristic, that is usually the turbulence intensity u'.

This is an important difference with respect to the Wiebe function, in which a lot of experimental data are needed, but there is no need to have any knowledge about the turbulent flow field. Therefore, the Wiebe function has the drawback not to be so predictive in some practical cases, e.g. if a change of fuel or induction system geometry is requested, since it is based on the assumption that whichever change in the engine configuration does not affect the combustion process, since the burning rate is imposed.

On the other hand, with the entrainment based burning law and the fractal approach, it is possible to gain the capability of being predictive but, in addition to the combustion sub-model, it is needed a turbulence sub-model as well.

If looking at an example, *Figure 3-7*, in which the results of (3.11) are compared to experimental results, it is possible to notice that the mean value of S_b/S_L is well kept, but there is no modulation.

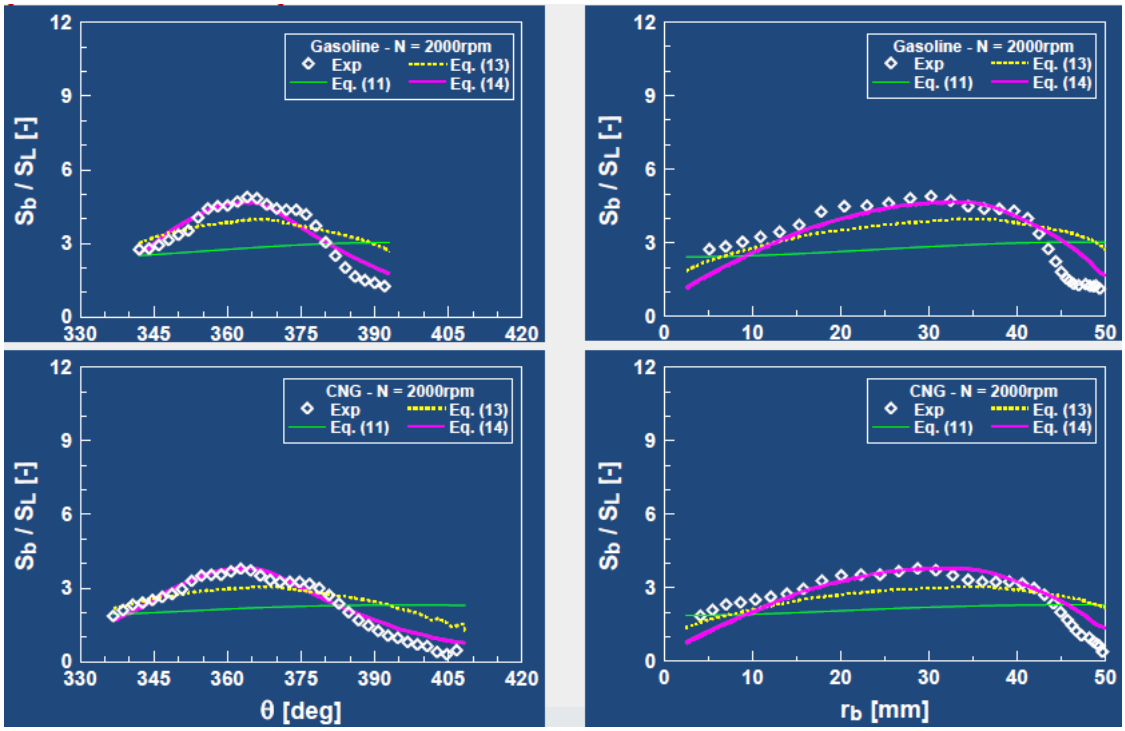

Figure 3-7: fractal models

Equation (3.11) can be modified in some ways that allow to achieve results which are much closer to the experimental ones. For example, by introducing a first modification, it is possible to write equation (3.12), that in the figure legend is referred to as Eq.(13):

$$\frac{S_b}{S_L} = \left\{ \frac{C_L\sqrt{A_b}}{C_L(h_{min}+S_P)\left[\frac{u' C_L(h_{min}+S_P)}{\nu}\right]^{-\frac{3}{4}}} \right\}^{D-2} \tag{3.12}$$

In equation (3.11) it has been considered $\varepsilon_o = L_i \propto (h_{min} + S_P)$, but this choice could be questionable. If some parameters, e.g. injection timing, are changed, even by considering the same engine at the same crank angle, the flame front could be located at different positions while ε_o would remain equal, which is not correct. If it is imagined to start from a certain injection timing providing a certain flame front dimension and passing to a new injection timing providing a larger flame front dimension, in the latter case eddies with larger length scales can corrugate the flame front with respect to the previous case. Due to

this, it has been thought to be more meaningful to relate the outer cutoff length scale with a characteristic dimension of the flame front, rather than a characteristic dimension of the combustion chamber. This is why in equation (3.12) it is considered $\varepsilon_o = C_L\sqrt{A_b}$.

If looking at *Figure 3-7*, in which equation (3.12) is labeled Eq.(13), the simulation results are much closer to the experimental ones with respect to equation (3.11).

A further improvement is achievable by introducing equation (3.13):

$$\frac{S_b}{S_L} = \left(\frac{\rho}{\rho_0}\right)^a \left\{ \frac{C_L\sqrt{A_b}}{C_L(h_{min}+S_P)\left[\frac{u' C_L(h_{min}+S_P)}{\nu}\right]^{-\frac{3}{4}}} \right\}^{D-2} \tag{3.13}$$

With respect to (3.12), it has been introduced the term $\left(\frac{\rho}{\rho_0}\right)^a$, where a is a parameter which has to be tuned, ρ is the density of the unburned gas at the considered crank angle, ρ_0 is the density of the unburned gas at a reference crank angle, which is normally the one at which there is the spark discharge. This ratio tries to account for the fact that S_L is the laminar burning speed and, when turbulences corrugate the flame front, depending on the combustion regime, there can be a region (i.e. corrugated flamelets) in which the main effect of the turbulences is to corrugate the flame front, or regions in which the turbulences apart from corrugating the flame front, can also enhance the heat transfer inside the flame front, thus changing its structure. This effect can be accounted by considering the ratio between the unburned gas densities, since it increases during the combustion. Looking at *Figure 3-7*, it is clear that with equation (3.13), labeled as Eq.(14), the experimental results are matched even better with respect to the previous equations.

As mentioned earlier when discussing the differences between the Wiebe function and the latter two discussed combustion sub-models, in both entrainment-based burning law and fractal model there is a parameter related to turbulences, that is the turbulence intensity u', that must be estimated: this can be done by means of a model which is able to reproduce the turbulence inside the cylinder. The most used approach used to simulate the in-cylinder turbulence generation is a model that considers the rate of change of the mean flow kinetic energy K and the rate of change of the turbulent kinetic energy k:

(3.14) $$\frac{dK}{dt} = \frac{1}{2}\dot{m}_i v_i^2 - P - K\frac{\dot{m}_0}{m}$$

(3.15) $$\frac{dk}{dt} = P - m\varepsilon - k\frac{m_0}{m}$$

Considering the mean flow kinetic energy rate of change, (3.14), the first term is the product between the intake mass flow rate and the square of a representative velocity across the inlet valve, that is a term related to the intake charge. P is the turbulent kinetic energy production within the combustion chamber and ε is the turbulent kinetic energy dissipation per unit mass.

In order to properly estimate P and ε, a CFD analysis would be needed. In some cases, there is the possibility to resort to semi-empirical equations like the following ones:

(3.16) $$P = 0.3307 c_\beta \frac{K}{L_i}\left(\frac{k}{m}\right)^{\frac{1}{2}}$$

(3.17) $$\varepsilon \cong \frac{u'^3}{L_i}$$

c_β is a parameter that should be tuned with a comparison with the results of a CFD computation: if these results are not available, there exists some standard values.

Basically, the computation of S_b requires the evaluation of both in-cylinder turbulence generation and the flame-turbulence interaction: in this case, it has been illustrated a turbulence model based on a zero-dimensional energy cascade from mean flow to viscous eddies dissipation.

4. Methodology and results: CNG

The project starts from the results of a research activity previously carried out by CRF, AVL and Politecnico di Torino, conducted on a CNG 4 in-line cylinders direct injection spark ignition turbocharged engine whose characteristics are reported in *Table 4-1*. Not all the geometric characteristics are presented for sake of confidentiality.

Displacement	[cm^3]	1368
Connecting rod length	[mm]	128.95
Wrist pin to crank offset	[mm]	1
TDC clearance height	[mm]	1
Compression ratio	[/]	12.6
Fuel	CNG	
Air supply	Turbocharged	
Intake valve lift	VVA	
Exhaust valve lift	Mechanical	

Table 4-1: engine characteristics

Starting from the geometric characteristics of the real engine and the turbocharger, it has previously been developed a model within the GT-POWER environment and, based on the experimental data, one of the several objectives of the abovementioned research activity was that of implementing the so called “three pressure analysis” (TPA) so as to verify the fluid dynamic behavior of the simulation model. Just to clarify the starting point of the current project, since the TPA was not part of the present work, a brief explanation of the TPA procedure is needed. Thanks to the available experimental data, among which several pressure and temperature values in different engine points, the injection law, the spark timing and valve lift profiles, boundary conditions could be set within the model. Then, the

model takes as input three experimentally available measured pressure cycles, i.e. cylinder, intake and exhaust ones, and produces a combustion law (e.g. burning rate) which is able to simulate a pressure cycle which is superimposable to the real one. Since the simulation converges when the intake manifold pressure matches the experimental one, a turbocharger controller is needed: when the boost pressure increases beyond acceptable values due to the increase of the rotational speed, the wastegate valve opens so that to discharge part of the exhaust gas driving the turbine to that to limit the previously mentioned speed and pressure increase. The wastegate valve is opened to different extents by the simulation model so that the intake manifold pressure is able to match the experimental one. Among the results of the described simulation procedure, the quantities which will be used as input for the present work are those related to the combustion such as anchor angle, combustion duration and Wiebe exponent. This procedure has been applied to different engine map points and spark advance tests performed at WOT, from which eight have been selected to carry out the present project.

4.1. Wiebe function implementation and model calibration

As mentioned in the introductive chapter, with the aim of subsequently switching to hydrogen fueling, the first step of the project starts from the outcomes of the previously carried out TPA analysis by keeping CNG fueling and aims at employing some of its results so that to implement a Wiebe function combustion model. The working points on which the discussed analysis has been conducted are divided between 5 engine map operating points, resumed in *Table 4-2*, and 3 points coming from detonation tests at wide open throttle (WOT) conditions with a sweep on spark advance in which no detonating cycles have been detected due to a not too advanced spark discharge (the maximum pressure registered in the combustion chamber increases with the spark advance, and more and more increased pressure peaks are likely to lead to the knock phenomenon), resumed in *Table 4-3*:

Working point	Bmep [bar]	Speed [rpm]
(1)	4	2000
(2)	8	2000
(3)	13	2500
(4)	3	3000
(5)	5	4000

Table 4-2: engine map operating points

Working point	Bmep [bar]	Speed [rpm]	Spark advance (CA° bTDC)
(6)	17	2000	7
(7)	17	2000	7.59
(8)	17	2000	8.16

Table 4-3: spark advance sweep tests

The first objective was to take the outputs of the previously developed TPA simulation models in terms of Wiebe exponent, combustion duration $\Delta\theta_{10\%-90\%}$ and anchor angle $\theta_{50\%}$, the last one representing a sort of combustion gravimetric center and, by keeping the same simulation model, to use them as input to develop a parallel model in which, so as to detach from experimental pressure cycle, the combustion characteristics were imposed. Theoretically speaking, even if the Wiebe function is a non-predictive sub-model in which the combustion is imposed, by implementing the same parameters coming from a model which was able to correctly reproduce the fluid-dynamic performance and behavior of the real engine, the results should have been consistent with the previously obtained one, i.e. they should have well matched the experimental results. Nonetheless, that was not the case and a model calibration, by acting on the Wiebe function parameter, was needed so that the new parallel model could be able to match the experimental results as well. For sake of confidentiality, all the results related to both experimental and simulated pressure cycles have been normalized. In the following, a comparison between the results coming from a straightforward application of the TPA models' outcomes and the calibrated results is presented. Despite the pressure cycles' calibration has been performed for each cylinder for each working point, for sake of simplicity only the results related to the first cylinder for each working point are presented. The calibration methodology is explained and discussed after the results' presentation.

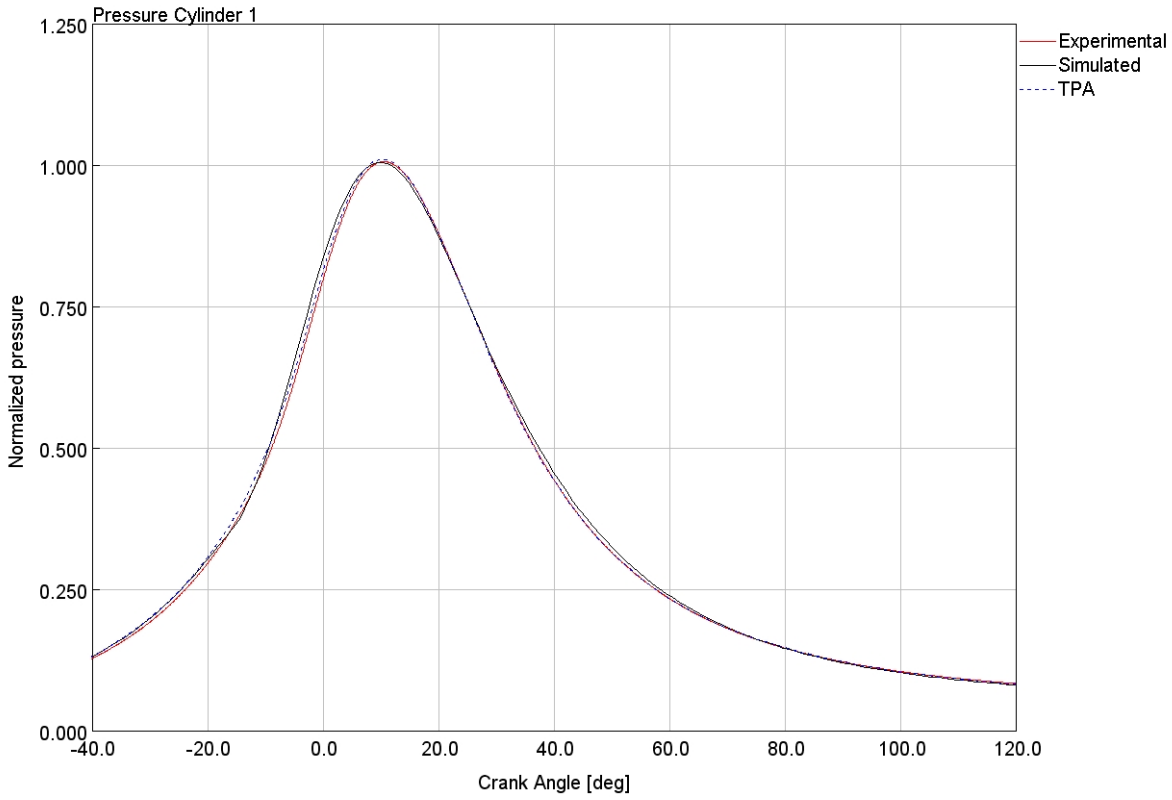

Figure 4-1: pressure cycle cyl 1, working point (1), comparison between experimental, simulated and TPA data

Working point (1)	[]	Exp	Sim	TPA
Intake Manifold Pressure	[bar]	1.024	1.024	1.024
Intake Manifold Temperature	[K]	312	310	309
Fuel Flow Rate	[kg/h]	2.28	2.15	2.14
Air Flow Rate	[kg/h]	39	37	37
Turbine Inlet Pressure	[bar]	1.071	1.057	1.057
Turbine Inlet Temperature	[K]	826	940	950
Turbine Outlet Pressure	[bar]	1.010	0.998	0.998
Turbine Outlet Temperature	[K]	672	927	927
PFP cylinder 1	[bar]	29.87	29.85	29.98
CA at PFP cylinder 1	[deg]	10.7	9.96	10.63

Table 4-4: working point (1), comparison between experimental, simulated and TPA parameters

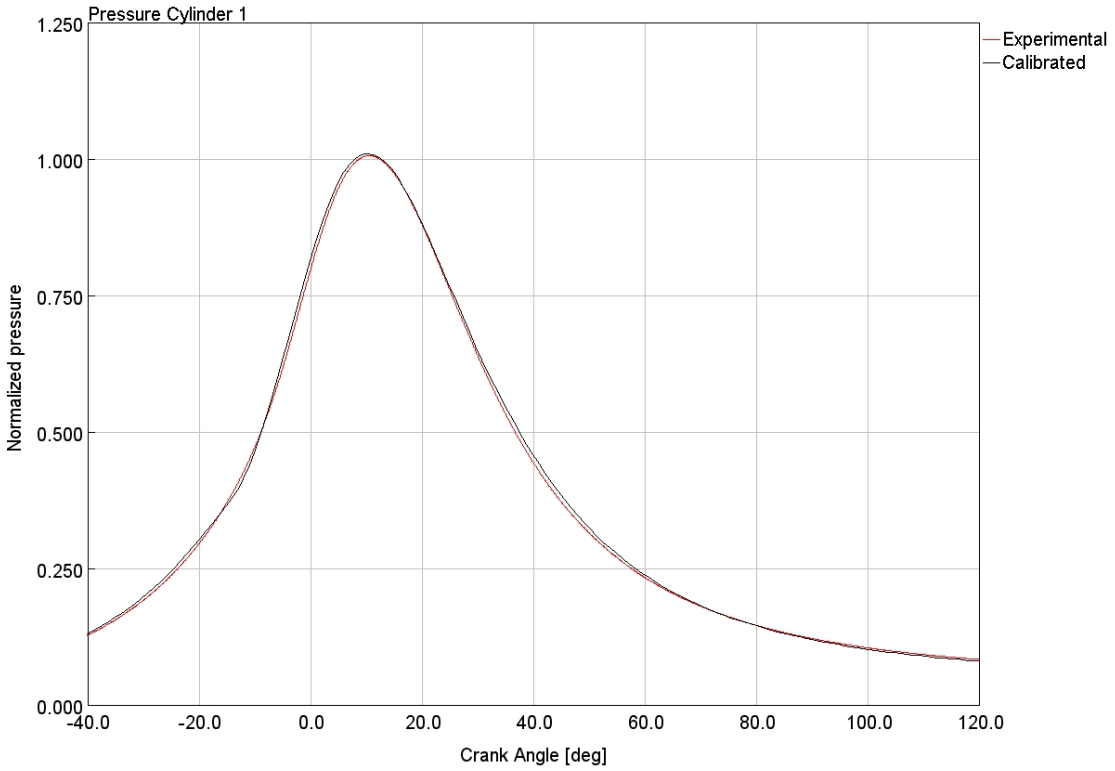

Figure 4-2: pressure cycle cyl 1, working point (1), comparison between experimental and simulation calibrated data

Working point (1)	[]	Experimental	Calibrated
Intake Manifold Pressure	[bar]	1.024	1.024
Intake Manifold Temperature	[K]	312	310
Fuel Flow Rate	[kg/h]	2.28	2.15
Air Flow Rate	[kg/h]	39	37
Turbine Inlet Pressure	[bar]	1.071	1.058
Turbine Inlet Temperature	[K]	826	931
Turbine Outlet Pressure	[bar]	1.010	0.998
Turbine Outlet Temperature	[K]	672	918
PFP cylinder 1	[bar]	29.87	29.98
CA at PFP cylinder 1	[deg]	10.7	10.43

Table 4-5: working point (1), comparison between experimental and simulation calibrated data

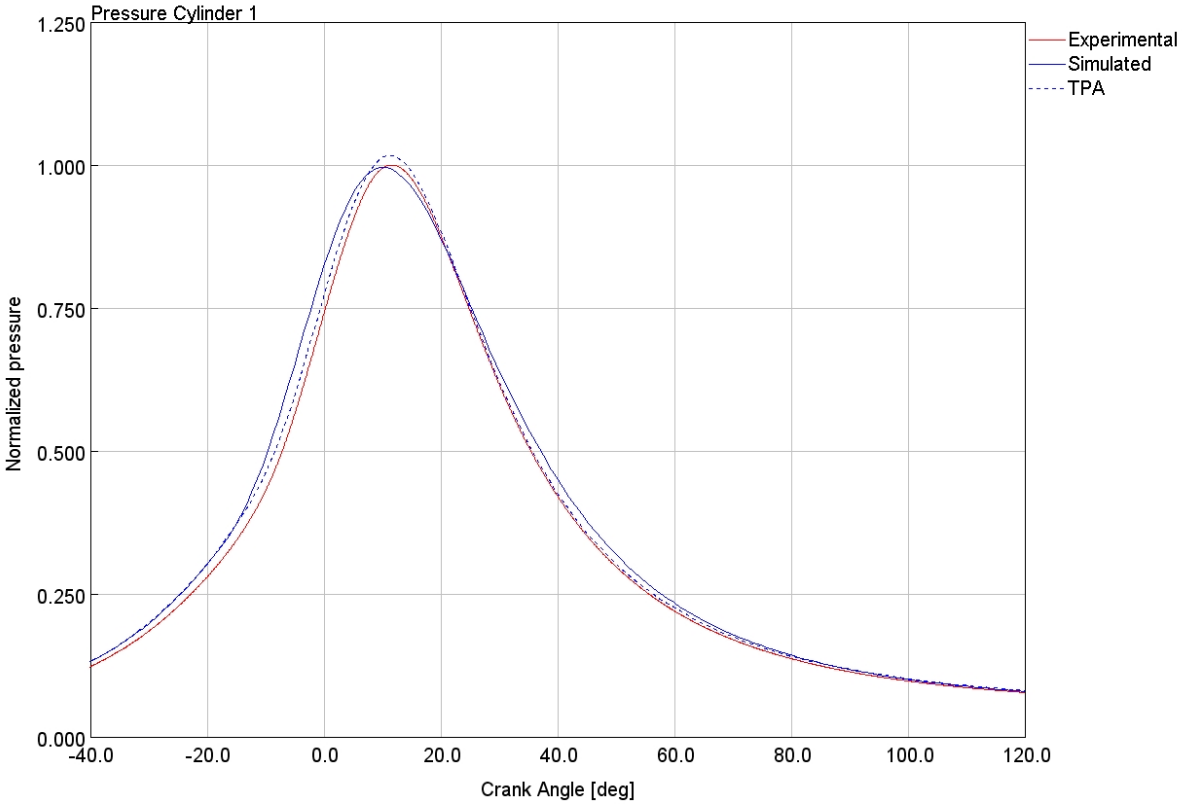

Figure 4-3: pressure cycle cyl 1, working point (2), comparison between experimental, simulated and TPA data

Working point (2)	[]	Exp	Sim	TPA
Intake Manifold Pressure	[bar]	1.147	1.147	1.147
Intake Manifold Temperature	[K]	311	310	310
Fuel Flow Rate	[kg/h]	3.91	3.86	3.86
Air Flow Rate	[kg/h]	67	66	66
Turbine Inlet Pressure	[bar]	1.186	1.171	1.170
Turbine Inlet Temperature	[K]	891	980	998
Turbine Outlet Pressure	[bar]	1.028	0.995	0.995
Turbine Outlet Temperature	[K]	746	957	974
PFP cylinder 1	[bar]	54.79	54.57	55.68
CA at PFP cylinder 1	[deg]	11.7	10.04	11.38

Table 4-6: working point (2), comparison between experimental, simulated and TPA parameters

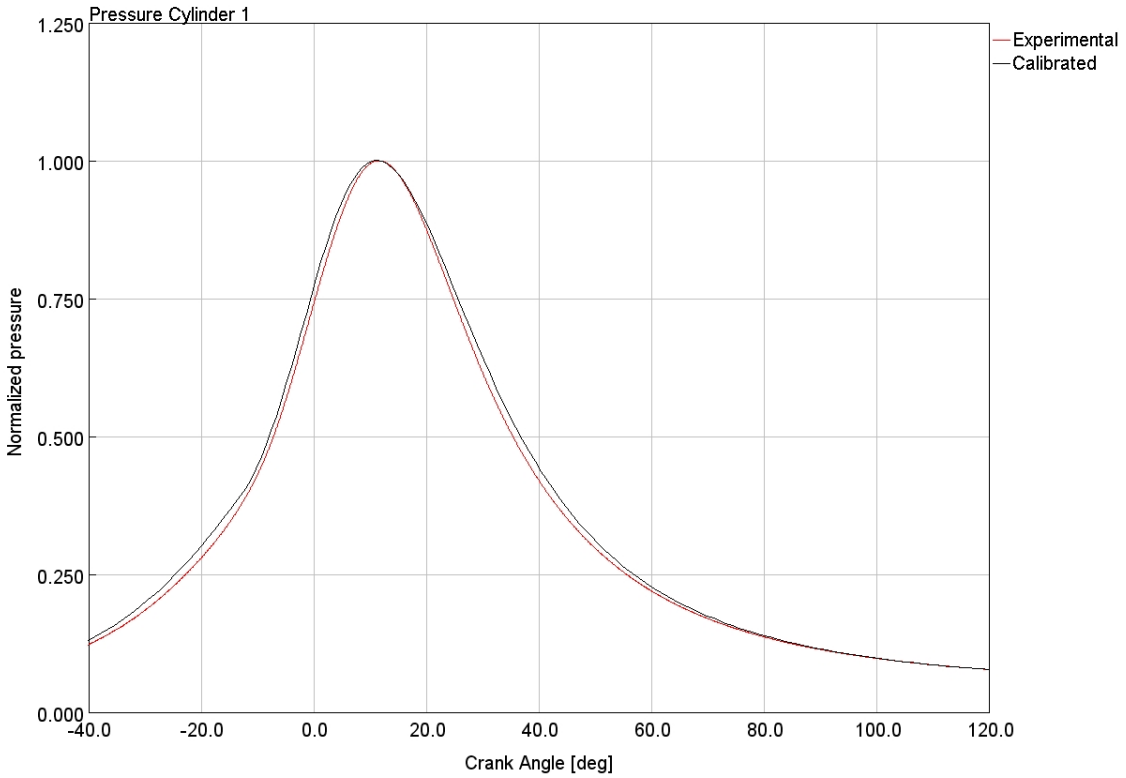

Figure 4-4: pressure cycle cyl 1, working point (2), comparison between experimental and simulation calibrated data

Working point (2)	[]	Experimental	Calibrated
Intake Manifold Pressure	[bar]	1.147	1.147
Intake Manifold Temperature	[K]	311	310
Fuel Flow Rate	[kg/h]	3.91	3.87
Air Flow Rate	[kg/h]	67	66
Turbine Inlet Pressure	[bar]	1.186	1.172
Turbine Inlet Temperature	[K]	891	970
Turbine Outlet Pressure	[bar]	1.028	0.995
Turbine Outlet Temperature	[K]	746	946
PFP cylinder 1	[bar]	54.79	54.79
CA at PFP cylinder 1	[deg]	11.7	11.23

Table 4-7: working point (2), comparison between experimental and simulation calibrated data

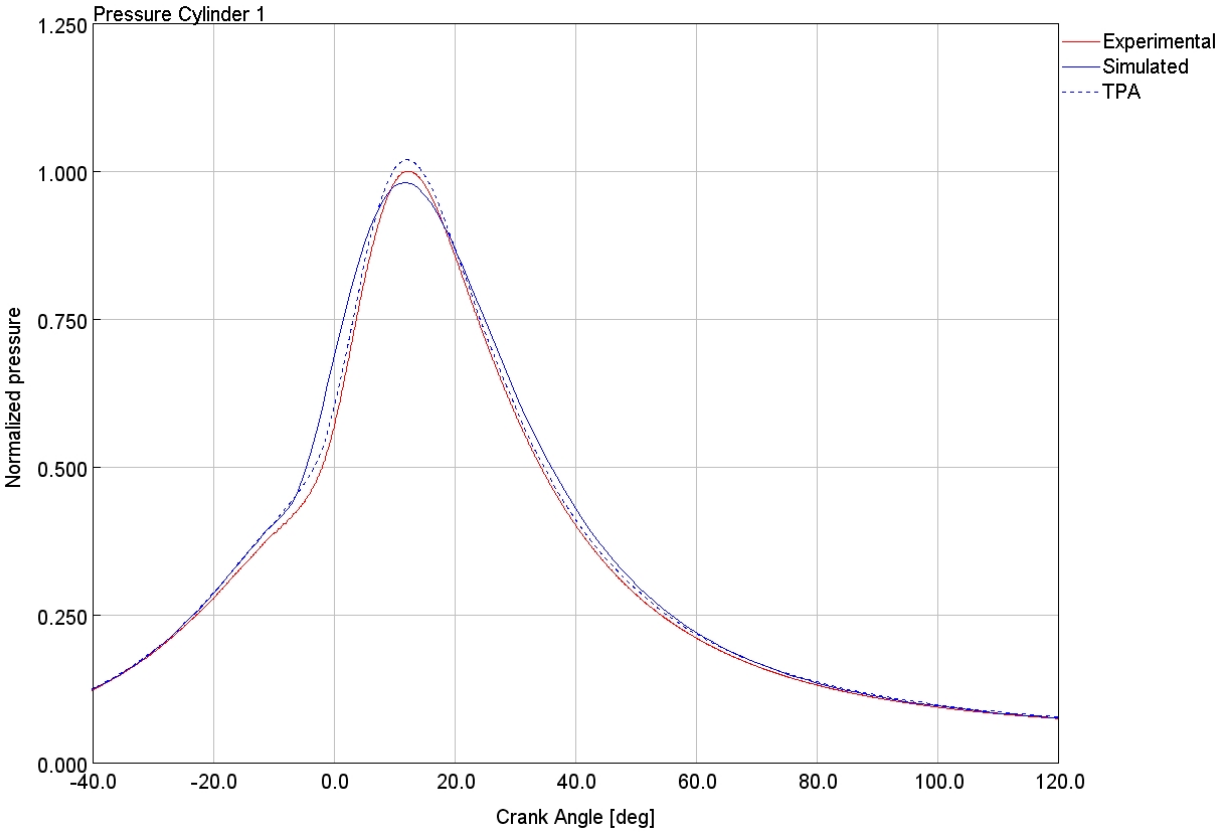

Figure 4-5: pressure cycle cyl 1, working point (3), comparison between experimental, simulated and TPA data

Working point (3)	[]	Exp	Sim	TPA
Intake Manifold Pressure	[bar]	1.279	1.279	1.279
Intake Manifold Temperature	[K]	313	310	310
Fuel Flow Rate	[kg/h]	7.68	7.57	7.56
Air Flow Rate	[kg/h]	131	129	129
Turbine Inlet Pressure	[bar]	1.394	1.377	1.375
Turbine Inlet Temperature	[K]	974	1058	1091
Turbine Outlet Pressure	[bar]	1.067	1.024	1.026
Turbine Outlet Temperature	[K]	861	1022	1053
PFP cylinder 1	[bar]	90.30	88.58	92.09
CA at PFP cylinder 1	[deg]	12.30	11.66	12.36

Table 4-8: working point (2), comparison between experimental, simulated and TPA parameters

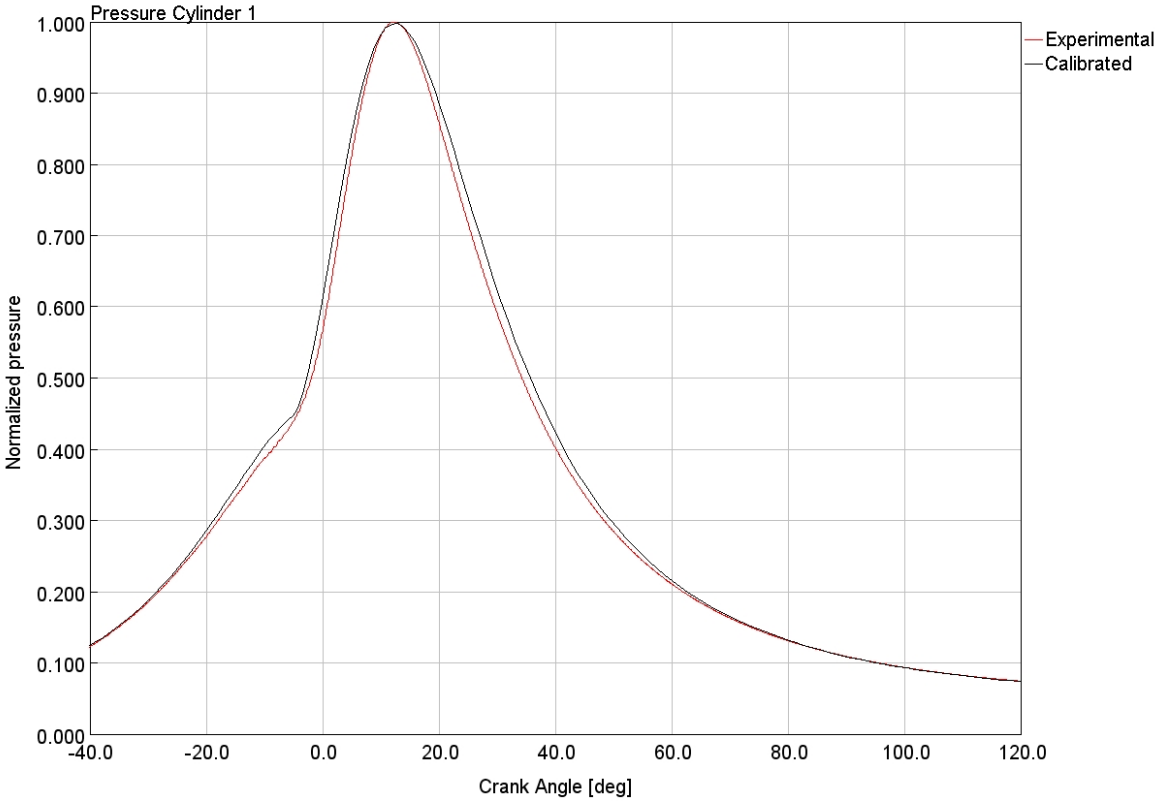

Figure 4-6: pressure cycle cyl 1, working point (3), comparison between experimental and simulation calibrated data

Working point (3)	[]	Experimental	Calibrated
Intake Manifold Pressure	[bar]	1.279	1.279
Intake Manifold Temperature	[K]	313	310
Fuel Flow Rate	[kg/h]	7.68	7.58
Air Flow Rate	[kg/h]	131	129
Turbine Inlet Pressure	[bar]	1.394	1.377
Turbine Inlet Temperature	[K]	974	1050
Turbine Outlet Pressure	[bar]	1.067	1.023
Turbine Outlet Temperature	[K]	861	1014
PFP cylinder 1	[bar]	90.30	90.12
CA at PFP cylinder 1	[deg]	12.30	12.36

Table 4-9: working point (3), comparison between experimental and simulation calibrated data

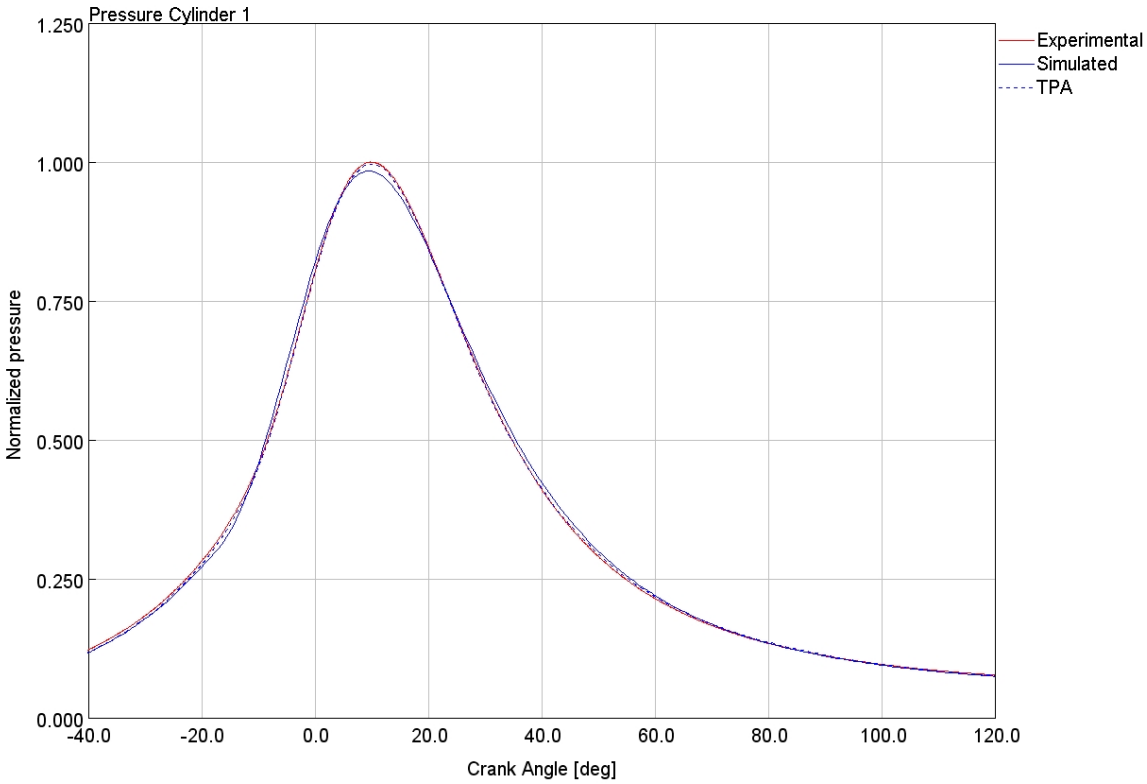

Figure 4-7: pressure cycle cyl 1, working point (4), comparison between experimental, simulated and TPA data

Working point (4)	[]	Exp	Sim	TPA
Intake Manifold Pressure	[bar]	1.056	1.058	1.058
Intake Manifold Temperature	[K]	313	312	312
Fuel Flow Rate	[kg/h]	2.93	2.73	2.73
Air Flow Rate	[kg/h]	50	47	47
Turbine Inlet Pressure	[bar]	1.12	1.09	1.09
Turbine Inlet Temperature	[K]	879	1008	1015
Turbine Outlet Pressure	[bar]	1.018	0.997	0.997
Turbine Outlet Temperature	[K]	708	991	997
PFP cylinder 1	[bar]	27.46	27.02	27.34
CA at PFP cylinder 1	[deg]	9.80	9.76	9.75

Table 4-10: working point (4), comparison between experimental, simulated and TPA parameters

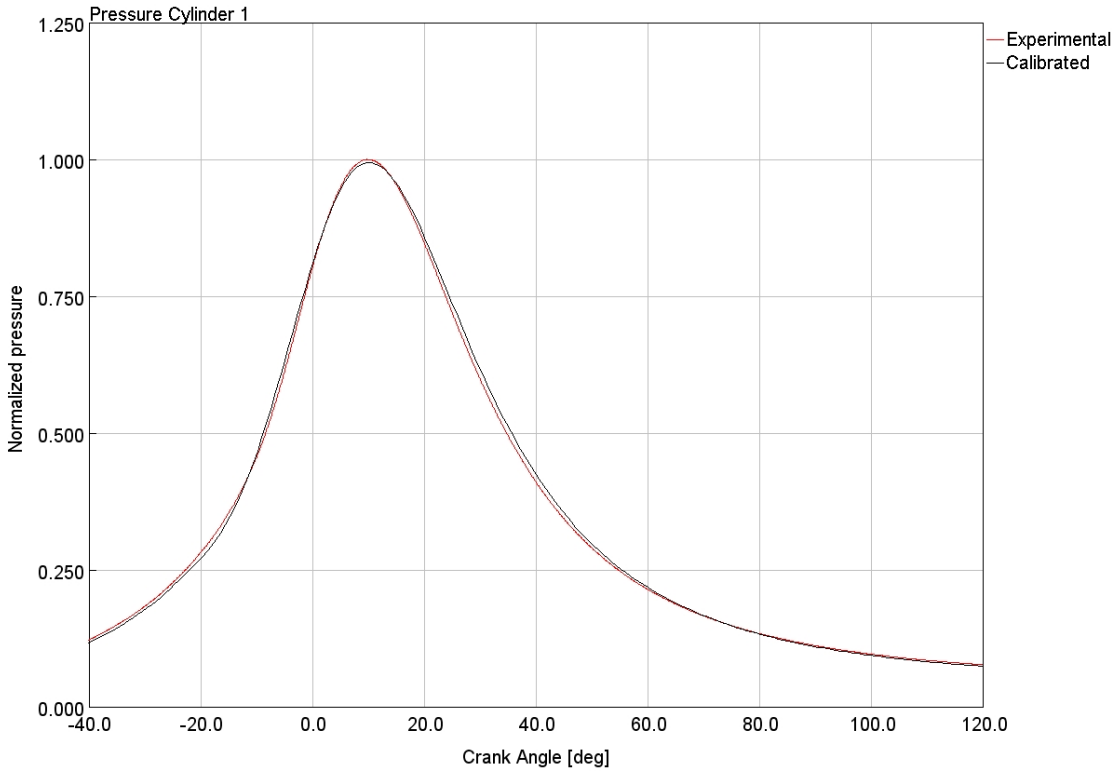

Figure 4-8: pressure cycle cyl 1, working point (4), comparison between experimental and simulation calibrated data

Working point (4)	[]	Experimental	Calibrated
Intake Manifold Pressure	[bar]	1.056	1.058
Intake Manifold Temperature	[K]	313	312
Fuel Flow Rate	[kg/h]	2.93	2.74
Air Flow Rate	[kg/h]	50	47
Turbine Inlet Pressure	[bar]	1.12	1.09
Turbine Inlet Temperature	[K]	879	999
Turbine Outlet Pressure	[bar]	1.018	0.997
Turbine Outlet Temperature	[K]	708	981
PFP cylinder 1	[bar]	27.46	27.29
CA at PFP cylinder 1	[deg]	9.80	10.31

Table 4-11: working point (4), comparison between experimental and simulation calibrated data

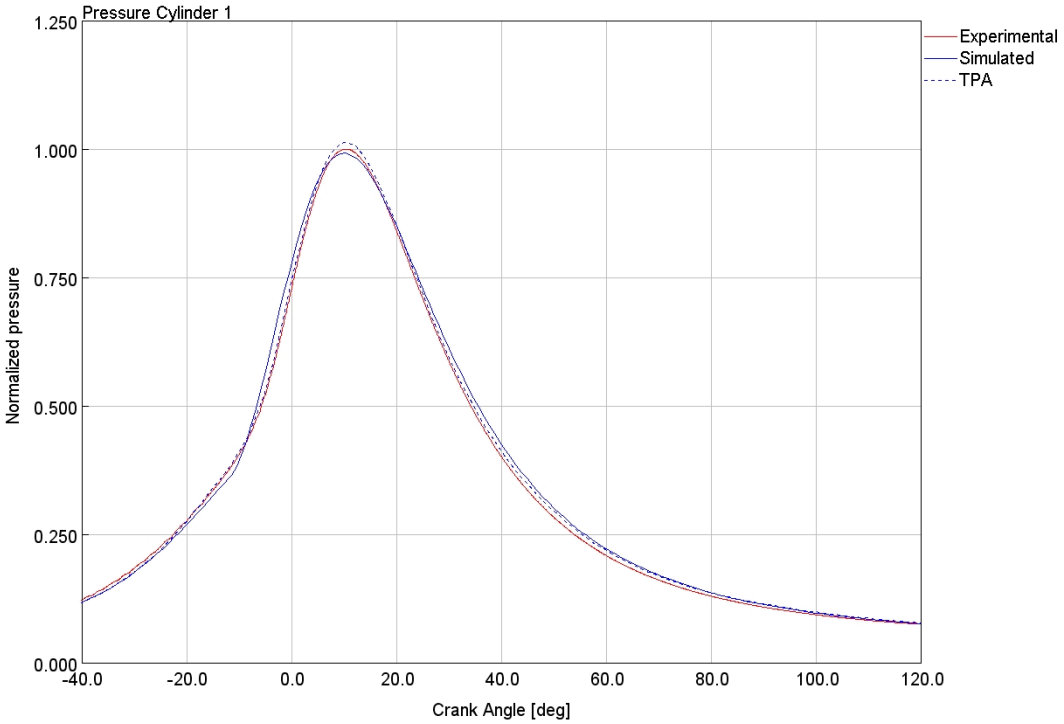

Figure 4-9: pressure cycle cyl 1, working point (5), comparison between experimental, simulated and TPA data

Working point (5)	[]	Exp	Sim	TPA
Intake Manifold Pressure	[bar]	1.225	1.225	1.225
Intake Manifold Temperature	[K]	316	315	315
Fuel Flow Rate	[kg/h]	5.97	5.71	5.71
Air Flow Rate	[kg/h]	103	99	99
Turbine Inlet Pressure	[bar]	1.339	1.367	1.267
Turbine Inlet Temperature	[K]	982	1098	1108
Turbine Outlet Pressure	[bar]	1.067	1.012	1.013
Turbine Outlet Temperature	[K]	855	1070	1080
PFP cylinder 1	[bar]	43.41	43.05	43.94
CA at PFP cylinder 1	[deg]	10.20	9.90	10.01

Table 4-12: working point (5), comparison between experimental, simulated and TPA parameters

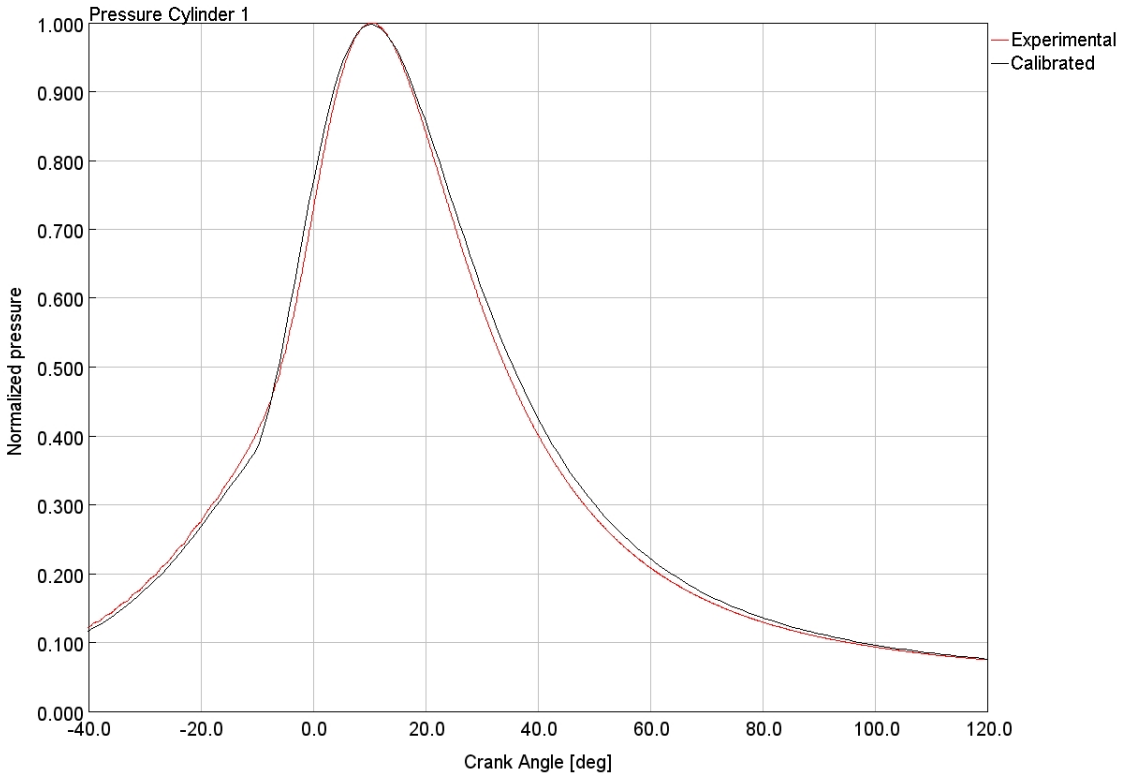

Figure 4-10: pressure cycle cyl 1, working point (5), comparison between experimental and simulation calibrated data

Working point (5)	[]	Experimental	Calibrated
Intake Manifold Pressure	[bar]	1.225	1.225
Intake Manifold Temperature	[K]	316	315
Fuel Flow Rate	[kg/h]	5.97	5.71
Air Flow Rate	[kg/h]	103	99
Turbine Inlet Pressure	[bar]	1.339	1.267
Turbine Inlet Temperature	[K]	982	1085
Turbine Outlet Pressure	[bar]	1.067	1.011
Turbine Outlet Temperature	[K]	855	1057
PFP cylinder 1	[bar]	43.41	43.32
CA at PFP cylinder 1	[deg]	10.20	10.44

Table 4-13: working point (5), comparison between experimental and simulation calibrated data

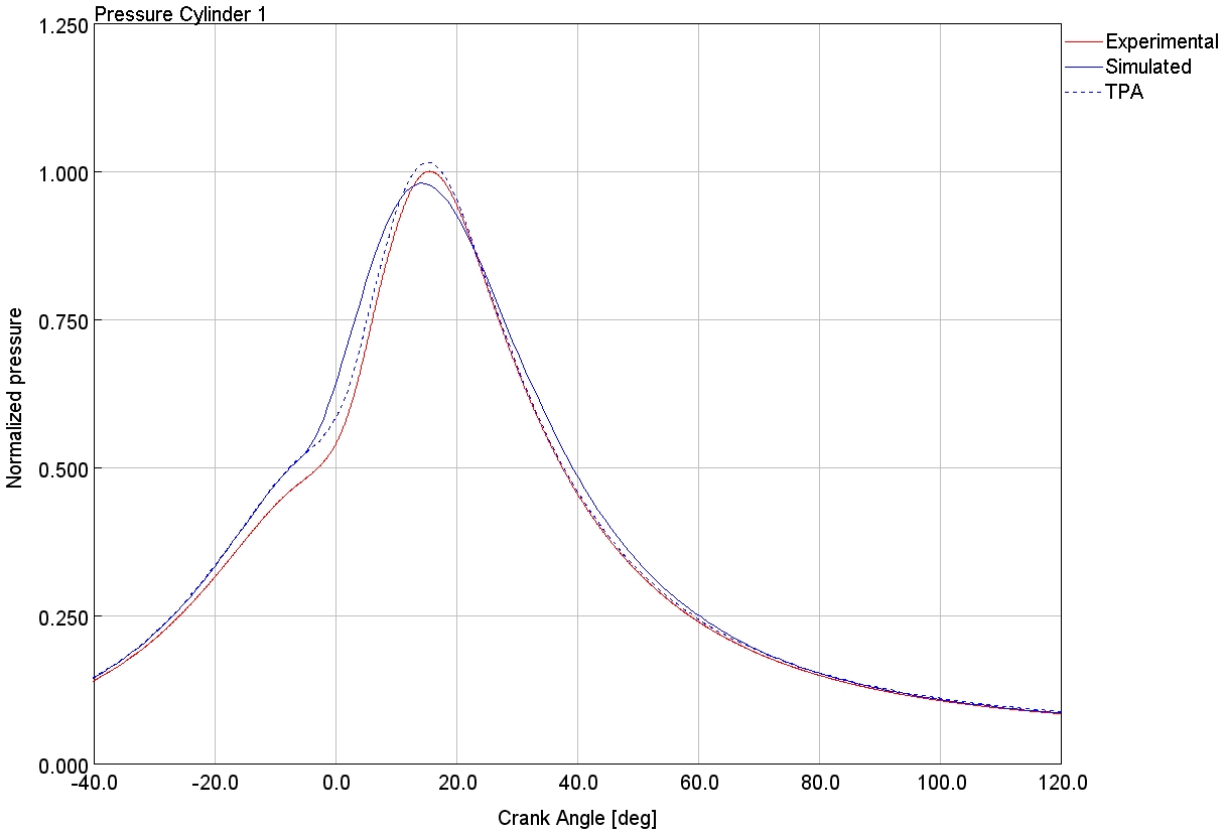

Figure 4-11: pressure cycle cyl 1, working point (6), comparison between experimental, simulated and TPA data

Working point (6)	[]	Exp	Sim	TPA
Intake Manifold Pressure	[bar]	1.741	1.741	1.741
Intake Manifold Temperature	[K]	349	354	354
Fuel Flow Rate	[kg/h]	8.01	7.78	7.77
Air Flow Rate	[kg/h]	136	132	132
Turbine Inlet Pressure	[bar]	1.673	1.619	1.615
Turbine Inlet Temperature	[K]	994	1077	1092
Turbine Outlet Pressure	[bar]	1.067	1.023	1.024
Turbine Outlet Temperature	[K]	875	1010	1025
PFP cylinder 1	[bar]	106.36	104.20	107.92
CA at PFP cylinder 1	[deg]	15.50	14.32	15.50

Table 4-14: working point (6), comparison between experimental, simulated and TPA parameters

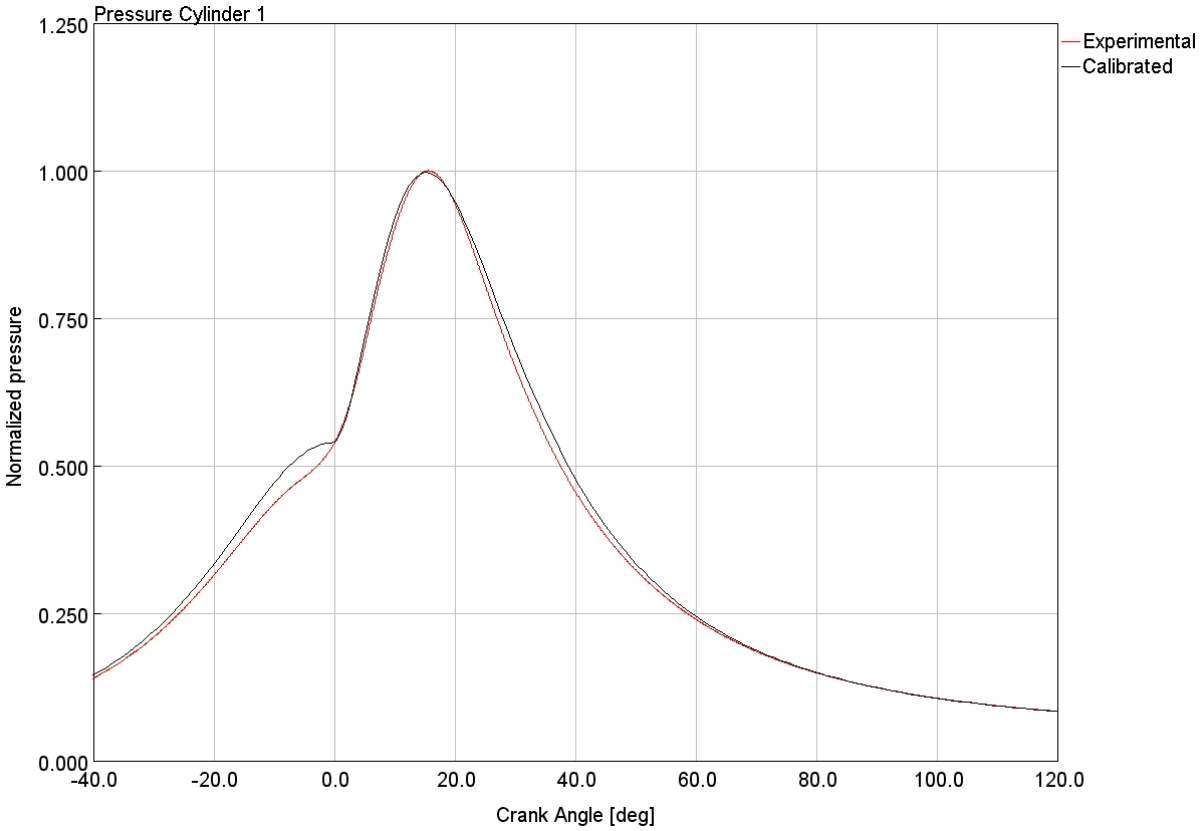

Figure 4-12: pressure cycle cyl 1, working point (6), comparison between experimental and simulation calibrated data

Working point (6)	[]	Experimental	Calibrated
Intake Manifold Pressure	[bar]	1.741	1.741
Intake Manifold Temperature	[K]	349	354
Fuel Flow Rate	[kg/h]	8.01	7.79
Air Flow Rate	[kg/h]	136	132
Turbine Inlet Pressure	[bar]	1.673	1.622
Turbine Inlet Temperature	[K]	994	1069
Turbine Outlet Pressure	[bar]	1.067	1.022
Turbine Outlet Temperature	[K]	875	1002
PFP cylinder 1	[bar]	106.36	106.06
CA at PFP cylinder 1	[deg]	15.50	15.31

Table 4-15: working point (6), comparison between experimental and simulation calibrated data

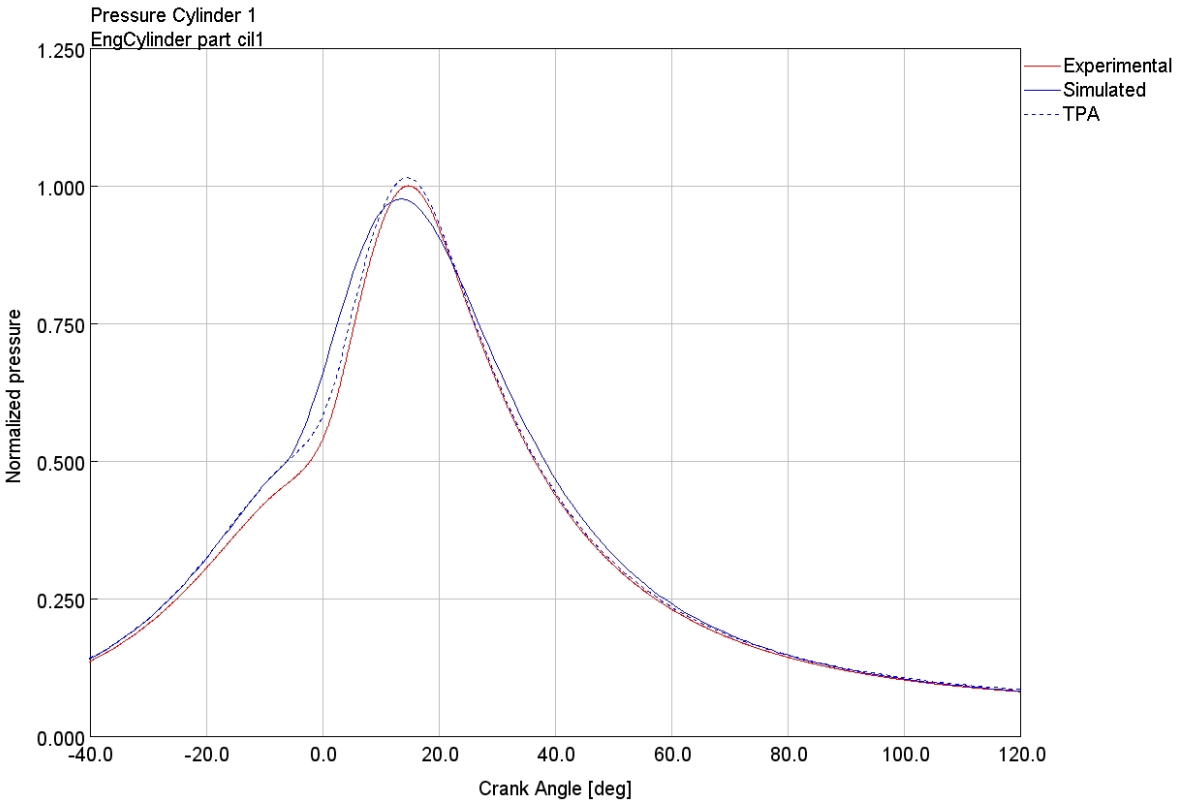

Figure 4-13: pressure cycle cyl 1, working point (7), comparison between experimental, simulated and TPA data

Working point (7)	[]	Exp	Sim	TPA
Intake Manifold Pressure	[bar]	1.728	1.728	1.728
Intake Manifold Temperature	[K]	350	354	354
Fuel Flow Rate	[kg/h]	7.94	7.72	7.71
Air Flow Rate	[kg/h]	135	131	131
Turbine Inlet Pressure	[bar]	1.663	1.611	1.606
Turbine Inlet Temperature	[K]	990	1066	1085
Turbine Outlet Pressure	[bar]	1.066	1.022	1.023
Turbine Outlet Temperature	[K]	872	999	1018
PFP cylinder 1	[bar]	108.73	106.14	110.31
CA at PFP cylinder 1	[deg]	14.80	13.54	14.52

Table 4-16: working point (7), comparison between experimental, simulated and TPA parameters

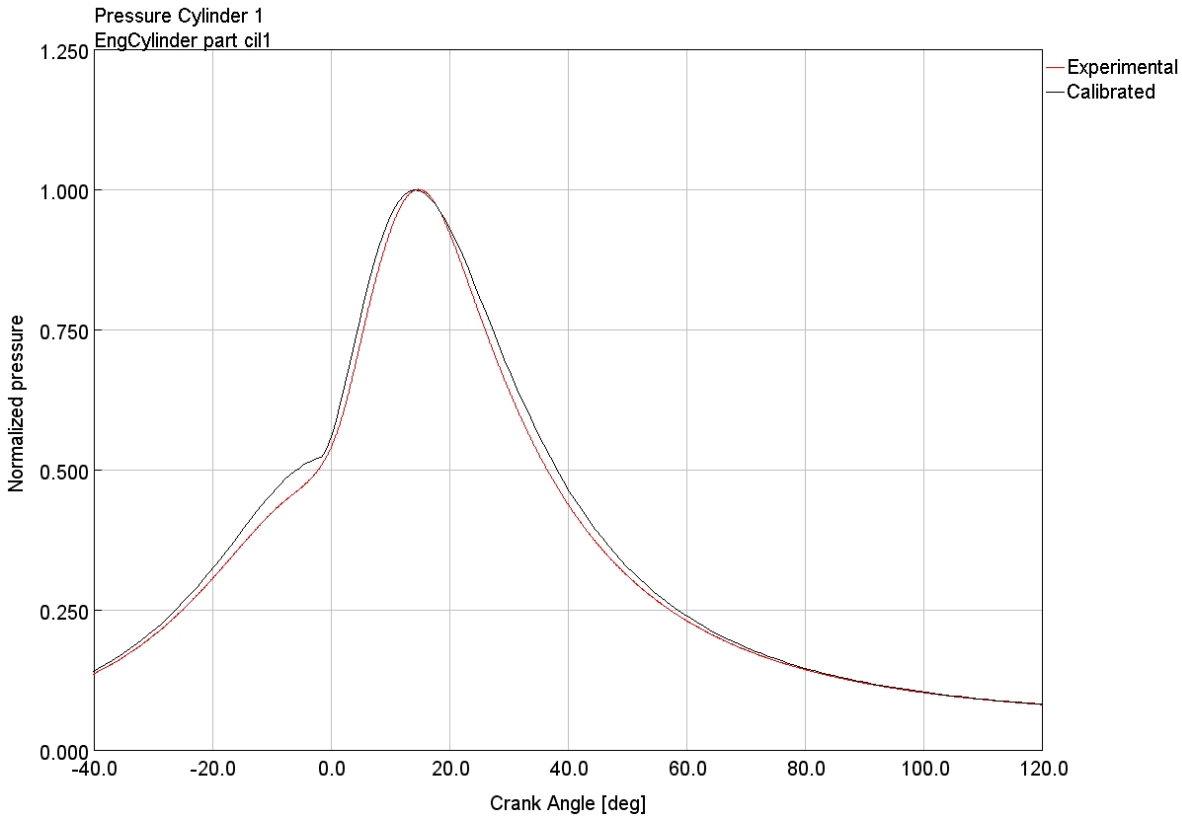

Figure 4-14: pressure cycle cyl 1, working point (7), comparison between experimental and simulation calibrated data

Working point (7)	[]	Experimental	Calibrated
Intake Manifold Pressure	[bar]	1.728	1.728
Intake Manifold Temperature	[K]	350	354
Fuel Flow Rate	[kg/h]	7.94	7.72
Air Flow Rate	[kg/h]	135	131
Turbine Inlet Pressure	[bar]	1.663	1.613
Turbine Inlet Temperature	[K]	990	1060
Turbine Outlet Pressure	[bar]	1.066	1.021
Turbine Outlet Temperature	[K]	872	994
PFP cylinder 1	[bar]	108.73	108.62
CA at PFP cylinder 1	[deg]	14.80	14.22

Table 4-17: working point (7), comparison between experimental and simulation calibrated data

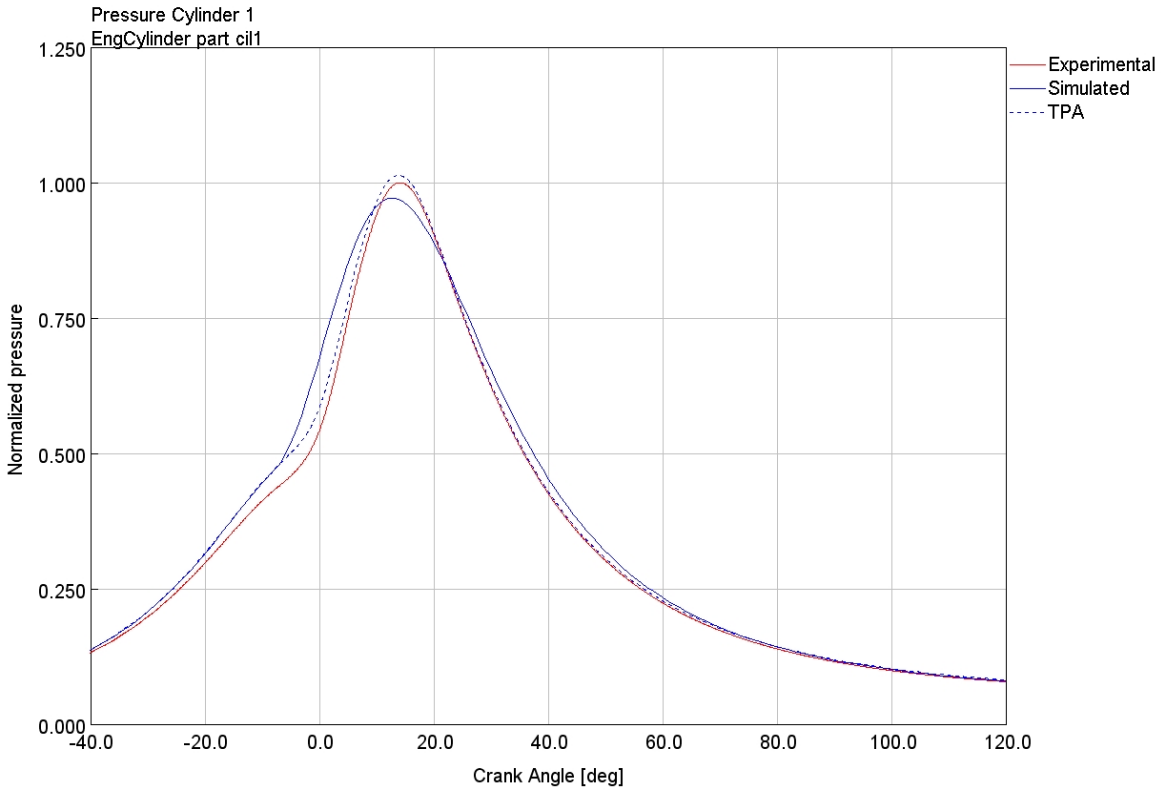

Figure 4-15: pressure cycle cyl 1, working point (8), comparison between experimental, simulated and TPA data

Working point (8)	[]	Exp	Sim	TPA
Intake Manifold Pressure	[bar]	1.717	1.717	1.717
Intake Manifold Temperature	[K]	350	354	354
Fuel Flow Rate	[kg/h]	7.88	7.67	7.66
Air Flow Rate	[kg/h]	134	130	130
Turbine Inlet Pressure	[bar]	1.654	1.605	1.600
Turbine Inlet Temperature	[K]	987	1059	1077
Turbine Outlet Pressure	[bar]	1.065	1.021	1.022
Turbine Outlet Temperature	[K]	869	993	1011
PFP cylinder 1	[bar]	110.74	107.53	112.23
CA at PFP cylinder 1	[deg]	14.10	12.79	13.78

Table 4-18: working point (8), comparison between experimental, simulated and TPA parameters

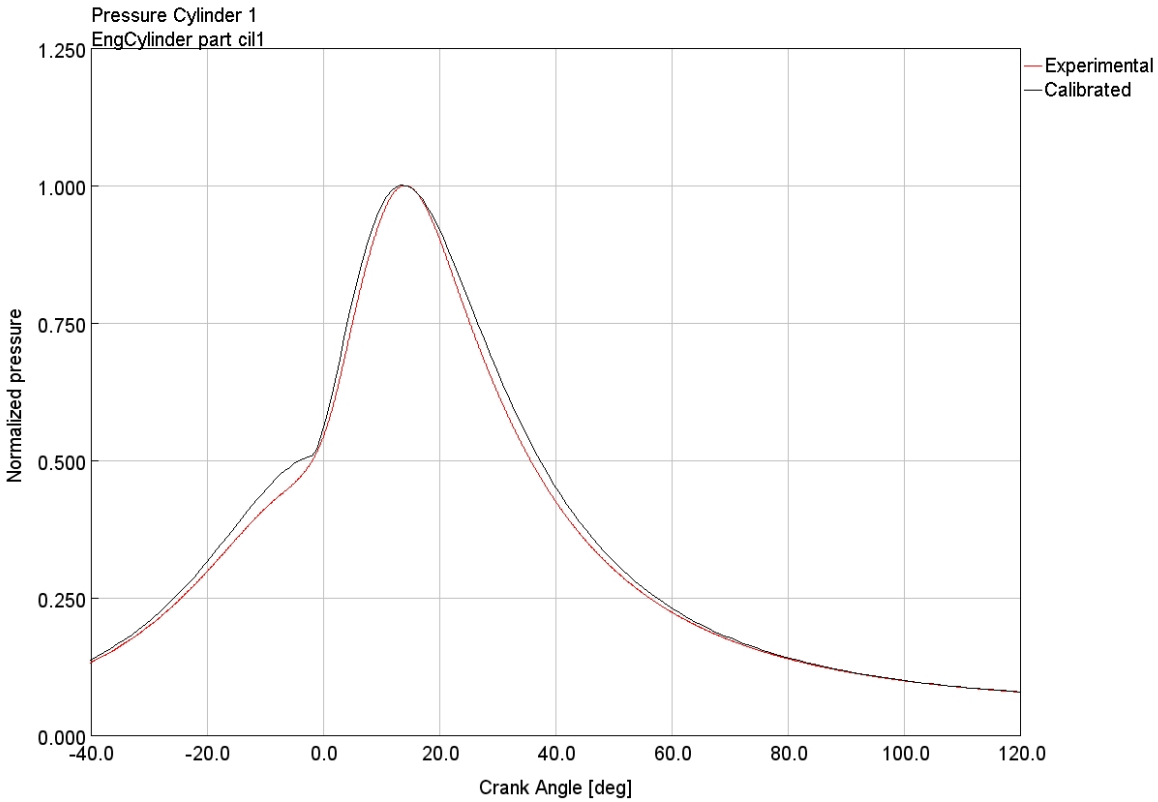

Figure 4-16: pressure cycle cyl 1, working point (8), comparison between experimental and simulation calibrated data

Working point (8)	[]	Experimental	Calibrated
Intake Manifold Pressure	[bar]	1.717	1.717
Intake Manifold Temperature	[K]	350	354
Fuel Flow Rate	[kg/h]	7.88	7.67
Air Flow Rate	[kg/h]	134	130
Turbine Inlet Pressure	[bar]	1.654	1.607
Turbine Inlet Temperature	[K]	987	1051
Turbine Outlet Pressure	[bar]	1.065	1.020
Turbine Outlet Temperature	[K]	869	985
PFP cylinder 1	[bar]	110.74	110.80
CA at PFP cylinder 1	[deg]	14.10	13.70

Table 4-19: working point (8), comparison between experimental and simulation calibrated data

The GT-POWER model needed to be calibrated and employed to carry out the simulations is depicted in *Figure 4-17*.

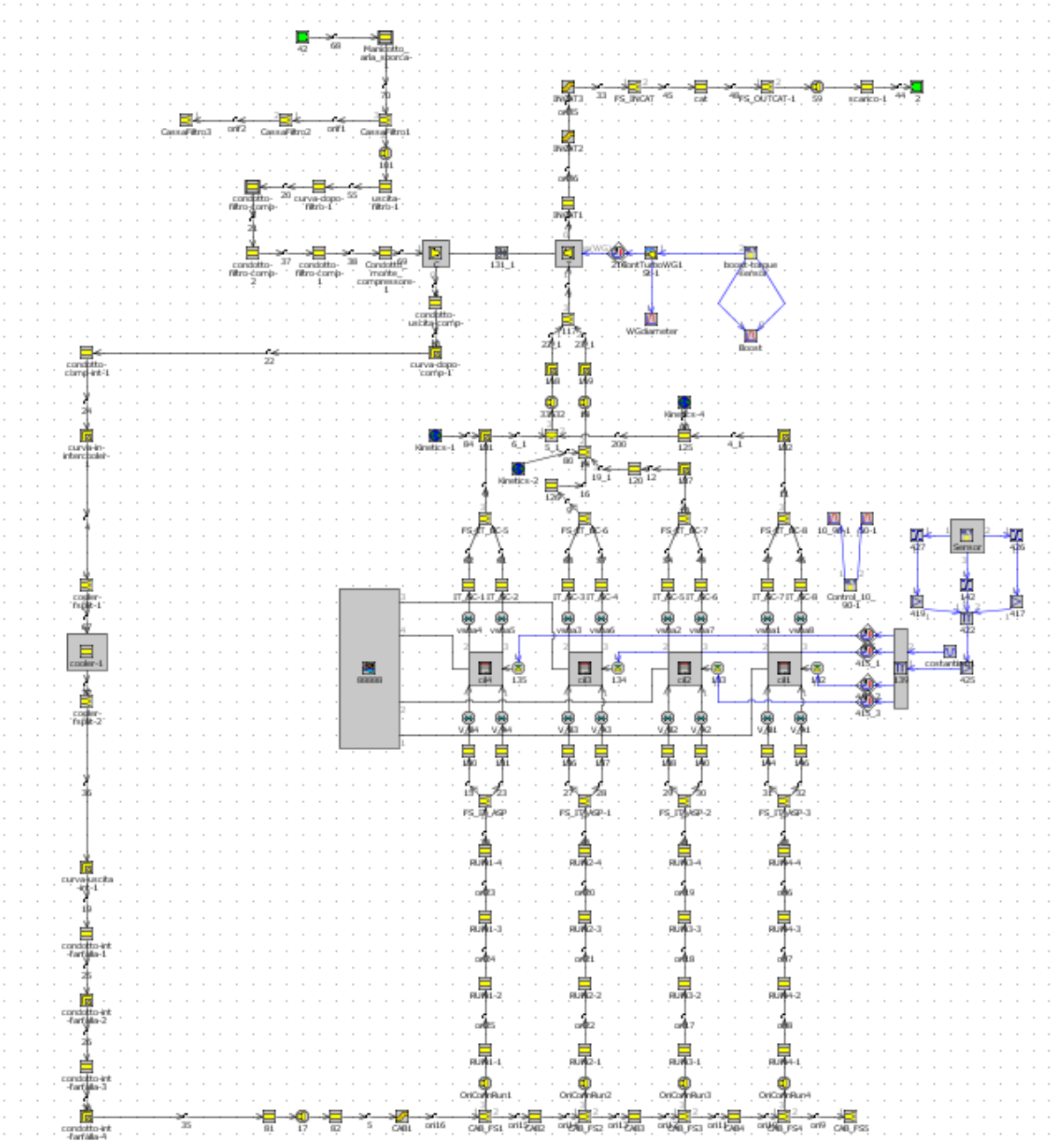

Figure 4-17: GT-POWER model

As previously explained, for each considered working point, the outputs of the formerly carried out TPA have been employed as inputs for the new model in which the combustion process has been modeled by means of Wiebe functions.

In particular, for each of the four cylinders, the Wiebe exponent, the combustion duration $\Delta\theta_{10\%-90\%}$ and the anchor angle MFB50 have been collected, presented in *Table 4-20* and *Table 4-21* and used for a first simulation run.

Working point (1)	Cyl 1	Cyl 2	Cyl 3	Cyl 4
MFB50 [deg]	8.07	7.33	6.23	6.63
$\Delta\theta$ 10-90% [deg]	35.97	35.72	32.57	37.14
m	0.9	0.94	0.99	0.87
Working point (2)	Cyl 1	Cyl 2	Cyl 3	Cyl 4
MFB50 [deg]	7.88	7.08	7.62	7.76
$\Delta\theta$ 10-90% [deg]	34.35	33.2	30.74	34.06
m	1.16	1.25	1.36	1.3
Working point (3)	Cyl 1	Cyl 2	Cyl 3	Cyl 4
MFB50 [deg]	7.73	7.77	7.99	7.88
$\Delta\theta$ 10-90% [deg]	25.47	26.29	22.25	26.84
m	0.74	0.67	0.72	0.63
Working point (4)	Cyl 1	Cyl 2	Cyl 3	Cyl 4
MFB50 [deg]	5.75	5.92	6.19	7.38
$\Delta\theta$ 10-90% [deg]	33.25	30.73	31.32	42.41
m	0.98	1.16	1.08	0.84

Table 4-20: Wiebe parameters from TPA, working points (1) to (4)

Working point (5)	Cyl 1	Cyl 2	Cyl 3	Cyl 4
MFB50 [deg]	5.6	7.66	9.02	5.95
$\Delta\theta$ 10-90% [deg]	29.37	33.38	30.28	38.56
m	0.67	0.5	0.74	0.5
Working point (6)	Cyl 1	Cyl 2	Cyl 3	Cyl 4
MFB50 [deg]	11.52	11.39	11.01	10.99
$\Delta\theta$ 10-90% [deg]	25.22	24.74	21.99	24.97
m	0.98	0.9	0.98	0.86
Working point (7)	Cyl 1	Cyl 2	Cyl 3	Cyl 4
MFB50 [deg]	10.57	10.62	10.41	10.35
$\Delta\theta$ 10-90% [deg]	25.77	25.16	22.08	25.49
m	0.95	0.88	0.94	0.85
Working point (8)	Cyl 1	Cyl 2	Cyl 3	Cyl 4
MFB50 [deg]	9.81	9.89	9.41	9.55
$\Delta\theta$ 10-90% [deg]	26.44	25.61	22.32	25.66
m	0.92	0.83	0.91	0.86

Table 4-21: Wiebe parameters from TPA, working points (5) to (8)

Even if these parameters coming from TPA, as noticeable from the previously presented results, were able to model a combustion process that generated pressure cycles which are very close to the experimental ones, apart from some numerical errors occurred between -20 °CA and 0 °CA (i.e. TDC firing), when switching to the parallel model in which the Wiebe functions are implemented using the same parameters, the pressure cycles were not corresponding anymore. The reason is that the Wiebe function is a simplified combustion sub-model with a well-defined shape given by its equation, while the real mass fraction burned profile could not exactly match such a defined shape. Due to this reason, it has been

necessary to calibrate the model in an iterative way, by acting on the same abovementioned Wiebe parameters and on the fraction of fuel burned at the end of the combustion process.

In particular, the effects of the different parameters on the Wiebe function shape and, consequently, on the pressure cycle, have been analyzed. The anchor angle has been kept the same in all cases to maintain the same gravimetric center of combustion; on the other hand, by shortening the combustion duration, it was possible to increase the slope of the central part of the function and therefore to increase the peak firing pressure, due to a faster combustion. The speed of combustion can also be tuned by acting on the Wiebe exponent, provided that higher values of m means faster combustion process; finally, the other parameter to be tuned, in some case, is a, which defines the combustion degree of completeness, in the sense of percentage of fuel effectively burned during the combustion process with respect to the total mass of injected fuel. By means of an iterative procedure, it has been possible to effectively calibrate the model against the available experimental data and to obtain pressure cycles reasonably close to the real ones, as it is possible to notice from the results presented above. The considered parameters result to be acceptably close to the experimental ones as well, except from the inlet and outlet turbine temperatures: for reasons that should be investigated, the model does not accurately reproduce the exhaust gas flow across the turbine, resulting in simulated temperature drops which are unacceptably lower and with temperature values which are unacceptably higher with respect to the real ones. To solve this issue, it has been tried to set a parameter present in GT-POWER, called “heat transfer multiplier”, to each part composing the exhaust system: this parameter is used to scale the heat transfer rate between the fluid and the walls. Unfortunately, neither adopting very large values of this parameter (that, in any case, would have meant fluid dynamic inconsistency) has been possible to solve the turbine related problem. So as to present the extent of this issue, which should be addressed in the future, the differences in temperature drops across the turbine between experimental and simulated values are presented in *Table 4-22*.

Working point (1)	[]	Experimental	Calibrated
Turbine Inlet Temperature	[K]	826	931
Turbine Outlet Temperature	[K]	672	918
ΔT=Tin-Tout	[K]	154	13
Relative difference exp-cal	[%]	100	8.44
Working point (2)	[]	Experimental	Calibrated
Turbine Inlet Temperature	[K]	891	970
Turbine Outlet Temperature	[K]	746	946
ΔT=Tin-Tout	[K]	145	24
Relative difference exp-cal	[%]	100	16.55
Working point (3)	[]	Experimental	Calibrated
Turbine Inlet Temperature	[K]	974	1050
Turbine Outlet Temperature	[K]	861	1014
ΔT=Tin-Tout	[K]	113	36
Relative difference exp-cal	[%]	100	31.86
Working point (4)	[]	Experimental	Calibrated
Turbine Inlet Temperature	[K]	879	999
Turbine Outlet Temperature	[K]	708	981
ΔT=Tin-Tout	[K]	171	18
Relative difference exp-cal	[%]	100	10.53

Working point (5)	[]	Experimental	Calibrated
Turbine Inlet Temperature	[K]	982	1085
Turbine Outlet Temperature	[K]	855	1057
ΔT=Tin-Tout	[K]	127	28
Relative difference exp-cal	[%]	100	22.05
Working point (6)	[]	Experimental	Calibrated
Turbine Inlet Temperature	[K]	994	1069
Turbine Outlet Temperature	[K]	875	1002
ΔT=Tin-Tout	[K]	119	67
Relative difference exp-cal	[%]	100	56.30
Working point (7)	[]	Experimental	Calibrated
Turbine Inlet Temperature	[K]	990	1060
Turbine Outlet Temperature	[K]	872	994
ΔT=Tin-Tout	[K]	118	66
Relative difference exp-cal	[%]	100	55.93
Working point (8)	[]	Experimental	Calibrated
Turbine Inlet Temperature	[K]	987	1051
Turbine Outlet Temperature	[K]	869	985
ΔT=Tin-Tout	[K]	118	66
Relative difference exp-cal	[%]	100	55.93

Table 4-22: temperature drops differences between experimental and simulated values

As it is possible to notice from the results presented in *Table 4-22*, across the different working points, the simulated temperature drops across the turbine ranges from 8.44% to 56.30% with respect to the experimental values. It is likely to be a problem of either the turbocharger model or the turbocharger controller, which has not been implemented by means of a classical PID controller but with a specific template available in the GT-POWER library. Further future steps should address the problem of the fluid dynamic turbocharger behavior.

In *Table 4-23* and *Table 4-24*, the parameters adopted within the Wiebe function that allowed for the model calibration are reported.

Working point (1)	Cyl 1	Cyl 2	Cyl 3	Cyl 4
MFB50 [deg]	8.07	7.33	6.23	6.63
$\Delta\theta$ 10-90% [deg]	34	30	32	31
m	0.9	1.5	0.99	1.1
Working point (2)	Cyl 1	Cyl 2	Cyl 3	Cyl 4
MFB50 [deg]	7.88	7.08	7.62	7.76
$\Delta\theta$ 10-90% [deg]	29	28.5	29	28
m	1.16	0.9	1.36	1.1
Working point (3)	Cyl 1	Cyl 2	Cyl 3	Cyl 4
MFB50 [deg]	7.73	7.77	7.99	7.88
$\Delta\theta$ 10-90% [deg]	21	20	22.25	19
m	0.74	0.67	0.72	0.8
Working point (4)	Cyl 1	Cyl 2	Cyl 3	Cyl 4
MFB50 [deg]	5.75	5.92	6.19	7.38
$\Delta\theta$ 10-90% [deg]	31	28	31.32	28

m	1.4	1.8	1.08	1.2

Table 4-23: Wiebe parameters, calibrated model, working points (1) to (4)

Working point (5)	Cyl 1	Cyl 2	Cyl 3	Cyl 4
MFB50 [deg]	5.6	7.66	9.02	5.95
$\Delta\theta$ 10-90% [deg]	28	27	32	26
m	0.67	1	0.74	0.5
Working point (6)	Cyl 1	Cyl 2	Cyl 3	Cyl 4
MFB50 [deg]	11.52	11.39	11.01	10.99
$\Delta\theta$ 10-90% [deg]	20	19	19	18
m	0.68	0.75	0.68	0.9
Working point (7)	Cyl 1	Cyl 2	Cyl 3	Cyl 4
MFB50 [deg]	10.57	10.62	10.41	10.35
$\Delta\theta$ 10-90% [deg]	21.5	20.5	20.5	19.5
m	0.65	0.6	0.6	0.7
Working point (8)	Cyl 1	Cyl 2	Cyl 3	Cyl 4
MFB50 [deg]	9.81	9.89	9.41	9.55
$\Delta\theta$ 10-90% [deg]	21	20	20	19.5
m	0.62	0.6	0.61	0.7

Table 4-24: : Wiebe parameters, calibrated model, working points (5) to (8)

4.2. Injector template modification

The subsequent step is concerned with the modification of the injector template for the reasons illustrated in the following. With the injector template implemented in the original model, that was the “InjProfileConn” from the GT-POWER library, it was possible to specify the rail pressure, the crank angle associated to the start of injection and the one associated to the end of injection, with the consequence of having a fixed injection duration. By employing such template, it was possible neither to specify the injector delivery rate nor, at least within the template settings, the desired air-fuel ratio. Moreover, the air flow rate on the base of which the model should have calculated the fuel flow rate for a given air-fuel ratio was not directly specifiable as well. So as to calculate the fuel flow rate with a fixed injection duration, it was implemented a part of the model which was directly importing the air flow rate and the crankshaft rotational speed from the “cranktrain” template; after the needed unit conversions (mass flow rates from kg/h to mg/s and rotational speed from rpm to cycles/s), the model was calculating the air mass flow aspirated during each engine cycle in mg/cycle and dividing it by four to obtain the intake air mass for each cylinder, for each cycle. Once these operations were performed, the desired air-fuel ratio was imposed by means of another template and the previously obtained air mass was divided by the air-fuel ratio so as to get the necessary fuel mass that, at this point, was imposed to each injector by means of an “actuator” template. The part of the model performing the above explained procedures is presented in *Figure 4.18*.

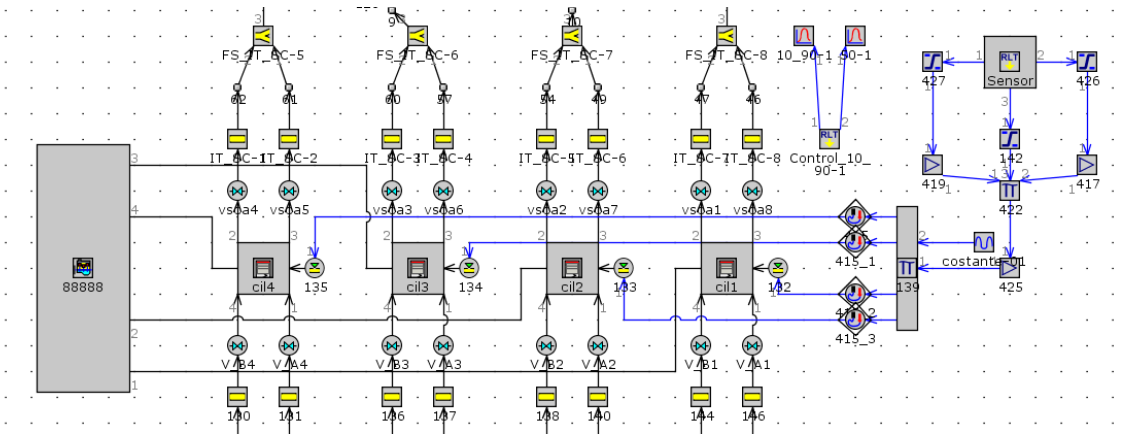

Figure 4-18: old model injector template

This part of the model, apart from being uselessly heavy, was not guaranteeing a sufficient flexibility degree in terms of injection law imposition and analysis, in the sense that it was not allowing to specify the injector delivery rate and to let the model calculate the injection duration on the base of the air flow rate aspirated and on the specified air-fuel ratio.

For this reason, the above-described part of the model has been deleted and a new injector template, called "InjAFSeqConn", has been implemented: this template guarantees the possibility to directly specify the desired injector delivery rate, the desired air-fuel ratio and also the template which has to work as air mass flow sensor. In this case, as air mass flow sensor it has been selected the template immediately upwards the intake manifold portion from which the different runners start to branch towards the cylinders. Apart from the definition of the injector geometric characteristics and of the illustrated parameters, also the crank angle associated to the start of injection or, alternatively, the end of injection, is specified and the cylinder template to which each injector has to refer are specified as well. The so-modified model is presented in *Figure 4-19*.

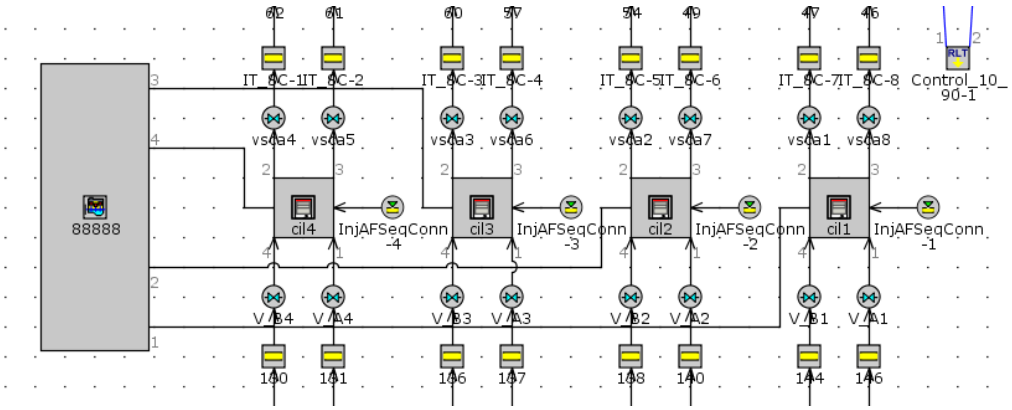

Figure 4-19: new model injector template

The outcome of this modification is a more flexible model in which the injection duration is not fixed anymore, but it is calculated on the base of the aspirated air flow rate, of the specified air-fuel ratio and of the fuel flow rate, in turn calculated on the base of the air flow rate and of the air-fuel ratio. As far as the injection timing is concerned, what is specified is either the crank angle associated to the start of injection or the crank angle associated to the end of injection.

4.3. PFI model development

The last step related to CNG fueling is concerned with the development of a model in which the injection is switched from DI to PFI. This has been done with the perspective, for future developments, to perform PFI 3D CFD simulation of the reference engine with a fully premixed charge. Even though a fully premixed charge could be also achieved by anticipating the injection timing and keeping the DI model so that the air-fuel mixture has enough time to achieve a proper mixing, it has been considered more realistic to develop a true PFI model.

In doing so, only working point (6), that is at full load, has been taken into account, since the procedure to obtain such modification is the same for each operating point. The objective was to achieve performances comparable to the corresponding DI engine model, starting from the consideration that the same air flow rate had to be achieved. Since switching from DI to PFI means to get a reduction in volumetric efficiency, which is a phenomenon observed whichever fuel is considered and it is more pronounced when considering gaseous fuels since, due to their lower density, they have the possibility to displace a larger volume in the cylinder leaving a lower volume for the intake air, this operation was done by operating a boost pressure sweep until the same air flow rate value of the DI model was achieved. The so-developed model, in which the injector has been moved into the intake ports, is presented in *Figure-4-20*.

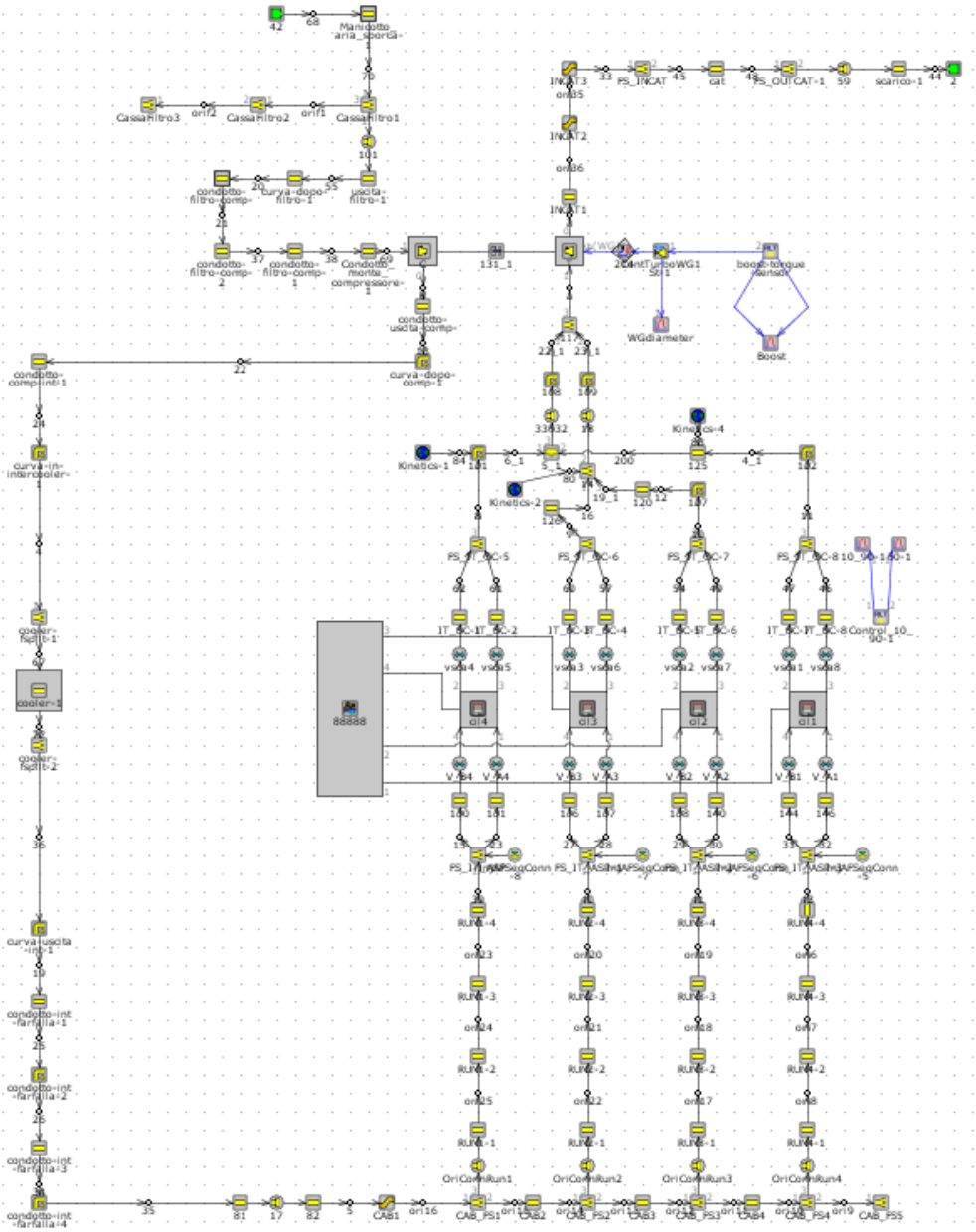

Figure 4-20: PFI CNG engine model

As it is possible to notice in *Table 4-25*, the same air flow rate has been achieved by increasing the target boost pressure from $p_{boost,DI} = 1.741\ bar$ to $p_{boost,PFI} = 1.868\ bar$ and, by so doing, the same performance of the DI engine model has been achieved.

Working point (6)	[]	CNG old	CNG PFI
Intake Manifold Pressure	[bar]	1.741	1.868
Intake Manifold Temperature	[K]	354	354
Fuel Flow Rate	[kg/h]	7.79	7.72
Air Flow Rate	[kg/h]	132	132
Target Boost Pressure	[bar]	1.741	1.868
Actual Boost Pressure	[bar]	1.741	1.868
Turbine Inlet Pressure	[bar]	1.622	1.694
Turbine Inlet Temperature	[K]	1069	1021
Turbine Outlet Pressure	[bar]	1.022	1.020
Turbine Outlet Temperature	[K]	1002	987
Wastegate Diameter	[mm]	6.18	4.11
PFP cylinder 1	[bar]	106.06	105.59
CA at PFP cylinder 1	[deg]	15.31	15.30
Brake Torque	[Nm]	189.83	190.06
Brake Power	[HP]	53.32	53.38
Volumetric Efficiency (manifold)	[%]	94	88
BMEP	[bar]	17.44	17.46

Table 4-25: CNG DI vs PFI models performances

As previously mentioned, the performances of the two models are absolutely comparable, with a predictable decrease in volumetric efficiency when switching from DI to PFI.

5. Methodology and results: hydrogen

This chapter is devoted to the explanation of the methodology which has been followed to switch from CNG fueling to H_2 fueling within the reference engine. For first, a stoichiometric mixture has been maintained, to assess which are the differences in terms of performances between a CNG-air stoichiometric mixture and an H_2-air stoichiometric mixture adopted in the same engine; secondly, a switch between a stoichiometric mixture and a lean mixture, in particular with $\lambda = 2$ has been realized and, with this configuration, the final objective was that of optimizing the engine performances.

The choice of the abovementioned lean relative air-fuel ratio to optimize the engine performances has been made according to the considerations exposed in chapter 1.2. Due to its chemical characteristics, a stoichiometric hydrogen-air mixture would lead to very high NOx production and to higher risk of preignition and backfire events, with the consequences of achieving larger noxious emissions and a higher risk of compromising the engine functioning, eventually leading to the engine failure.

A comparison between the characteristics of CNG, hydrogen and the two most common hydrocarbon-based fuels in reported in *Figure 5-1*.

Property	Hydrogen	CNG	Gasoline	Diesel
Carbon content (mass%)	**0**	75 [e]	84	86
Lower heating value (MJ/kg)	**119.7**	45.8	44.8	42.5
Density [a,b] (kg/m^3)	**0.089**	0.72	730–780	830
Volumetric energy content [a,b] (MJ/m^3)	**10.7**	33.0	33×10^3	35×10^3
Molecular weight	2.016	16.043 [e]	~110	~170
Boiling point [a] (K)	20	111 [e]	298–488	453–633
Auto-ignition temperature (K)	**858**	813 [e]	~623	~523
Minimum ignition energy in air [a,d] (mJ)	**0.02**	0.29	0.24	0.24
Stoichiometric air/fuel mass ratio	34.5	17.2 [e]	14.7	14.5
Stoichiometric volume fraction in air (%)	29.53	9.48	~2 [f]	-
Quenching distance [a,c,d] (mm)	**0.64**	2.1 [e]	~2	-
Laminar flame speed in air [a,c,d] (m/s)	**1.85**	0.38	0.37–0.43	0.37–0.43 [g]
Diffusion coefficient in air [a,b] (m^2/s)	8.5×10^{-6}	1.9×10^{-6}	-	-
Flammability limits in air (vol%)	4–76	5.3–15	1–7.6	0.6–5.5
Adiabatic flame temperature [a,c,d] (K)	2480	2214	2580	~2300

[a] at 1 bar, [b] at 273 K, [c] at 298 K, [d] at stoichiometry, [e] methane, [f] vapor and [g] n-heptane.

Figure 5-1: comparison between different fuels

5.1. Hydrogen-air stoichiometric mixture

With the aim of switching from CNG to hydrogen, three significative working points have been chosen, instead of the previously considered eight, which are reported in *Table 5-1*.

Working point	Bmep [bar]	Speed [rpm]
(1)	4	2000
(3)	13	2500
(6)	17	2000

Table 5-1: hydrogen engine working points

At the very beginning, the model featuring the old injector templates was adopted and, for each working point and according to the different characteristics of the considered fuels, the air-fuel ratio has been changed from $\alpha_{st,CNG} = 17.2$ to $\alpha_{st,H2} = 34.5$ and the rail pressure has been doubled. If the rail pressure was kept the same as the one used for CNG, due to the different chemical characteristics of the fuels, the injected flow rate would have been much lower with subsequent increased injection durations: thus, the rail pressure has been doubled not to have too extended injection durations. For example, the rail pressure used for CNG in working point (6) was $p_{rail,CNG} = 16\ bar$ and therefore it has been imposed $p_{rail,H2} = 32\ bar$. A reference value for DI CNG engines is $p_{rail,CNG} = 20\ bar$, however it is possible to find in the literature several studies that reports usable rail pressure for hydrogen fueling up to $p_{rail,H2} = 100\ bar$, therefore the employed values are kept within an acceptable range.

This has been done so as to extrapolate from the first simulations the injector delivery rates that would have to be employed, as a first approximation, when switching to the model featuring the latter injector templates in which, as previously explained, it is possible to impose the injector delivery rate itself, while the injection duration is directly calculated by the model on the base of the other relevant parameters.

The results of the so-set simulations are presented in the following, where the results related to the pressure cycles, the intake air mass flow rates and the exhaust mass flow rates, for sake of simplicity, are referred to cylinder 1 only.

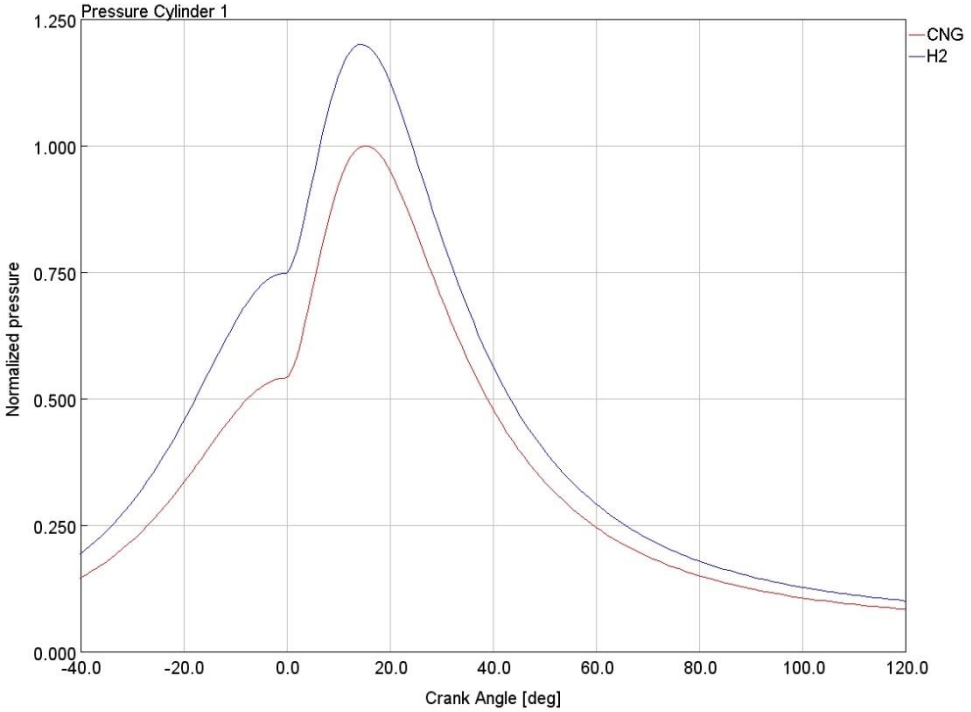

Figure 5-2: pressure cycle, CNG vs H2, working point (6)

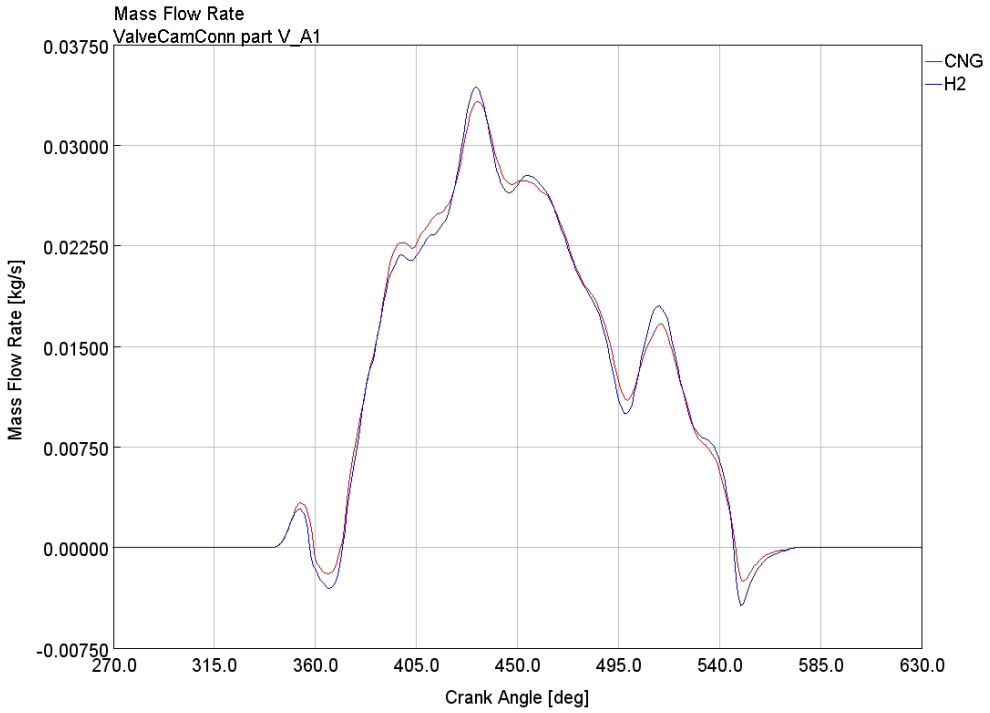

Figure 5-3: intake mass flow rate, CNG vs H2, working point (6)

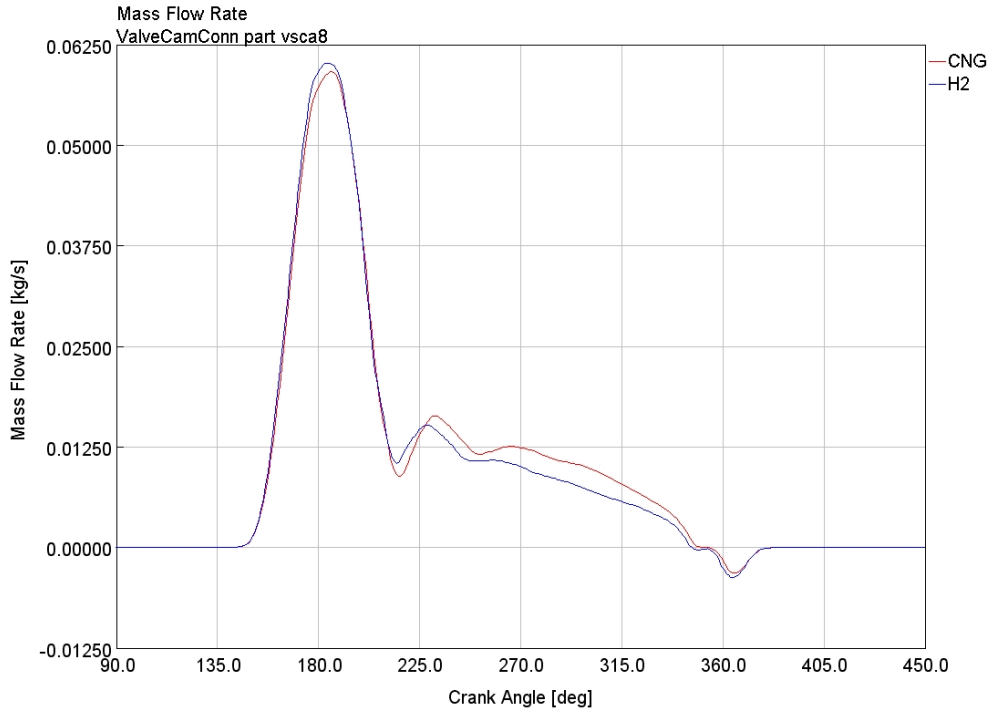

Figure 5-4: exhaust mass flow rate, CNG vs H2, working point (6)

Working point (6)	[]	Calibrated CNG	H2
Intake Manifold Pressure	[bar]	1.741	1.741
Intake Manifold Temperature	[K]	354	354
Fuel Flow Rate	[kg/h]	7.79	3.81
Air Flow Rate	[kg/h]	132	129
Target Boost Pressure	[bar]	1.741	1.741
Actual Boost Pressure	[bar]	1.741	1.741
Turbine Inlet Pressure	[bar]	1.622	1.566
Turbine Inlet Temperature	[K]	1069	1150
Turbine Outlet Pressure	[bar]	1.022	1.032
Turbine Outlet Temperature	[K]	1002	1085

Wastegate Diameter	[mm]	6.18	8.92
PFP cylinder 1	[bar]	106.06	127.33
CA at PFP cylinder 1	[deg]	15.31	14.52
Brake Torque	[Nm]	189.83	215.26
Brake Power	[HP]	53.32	60.46
Volumetric Efficiency (manifold)	[%]	94	92.2
BMEP	[bar]	17.44	19.77

Table 5-2: working point (6), CNG vs H2

As it is possible to notice by looking at the presented results, the air flow rate remains similar while the fuel flow rate changes accordingly to the hydrogen stoichiometric air-fuel ratio, which is about twice the CNG stoichiometric air-fuel ratio. The target boost pressure is reached as well and the turbocharger behaves properly, net of the previously explained temperature-drop related issues. The wastegate valve, in the hydrogen case, opens 2.74 mm more with respect to CNG, since the exhaust gas reaches higher temperatures and carries higher enthalpy. The intake and exhaust mass flow rates are extremely close for both fuels since the same valve lift profile has been maintained. The peak firing pressure increases of about 20%, the brake torque increases of about 13.4%, as well as the power and the brake mean effective pressure, obviously. This behavior, which is similar to the one observed in working point (3), can be easily justified by the following consideration. The specific constants of hydrogen, methane and air are reported in equations (5.1), (5.2) and (5.3).

(5.1) $$\bar{R}_{H2} = 4157 \frac{J}{kmolK}$$

(5.2) $$\bar{R}_{CH4} = 519 \frac{J}{kmolK}$$

(5.3) $$\bar{R}_{air} = 287 \frac{J}{kmolK}$$

If the specific constants of hydrogen-air and methane-air mixtures are calculated, with reference to stoichiometric conditions, (5.4) and (5.5) are obtained.

(5.4) $$\bar{R}_{H2-air} = \frac{34.5 \cdot 287 + 1 \cdot 4157}{35.5} \approx 396 \frac{J}{kmolK}$$

(5.5) $$\bar{R}_{CH4-air} = \frac{17.2 \cdot 287 + 1 \cdot 519}{18.2} \approx 300 \frac{J}{kmolK}$$

If assuming the perfect gas law to be applicable, if considering the same volume and temperature values, since both fuels are injected at the same temperature and the engine displacement is the same, being the pressure directly proportional to the gas constant, and being torque and power proportional to the pressure, the previously exposed results are justified. In the following, the results related to working points (3) and (1) are reported and discussed.

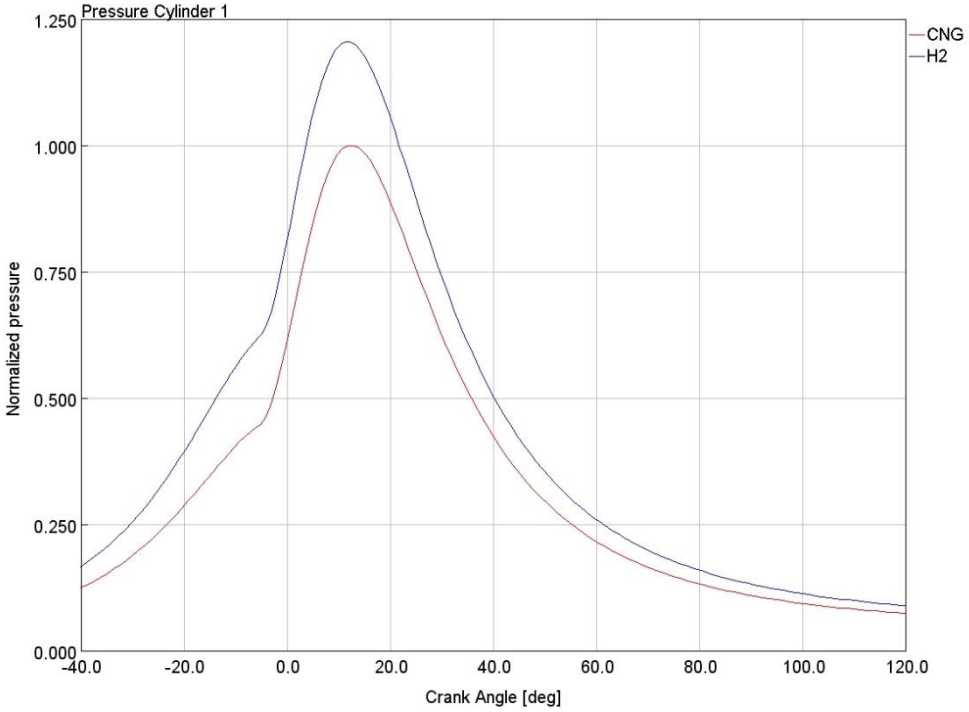

Figure 5-5: pressure cycle, CNG vs H2, working point (3)

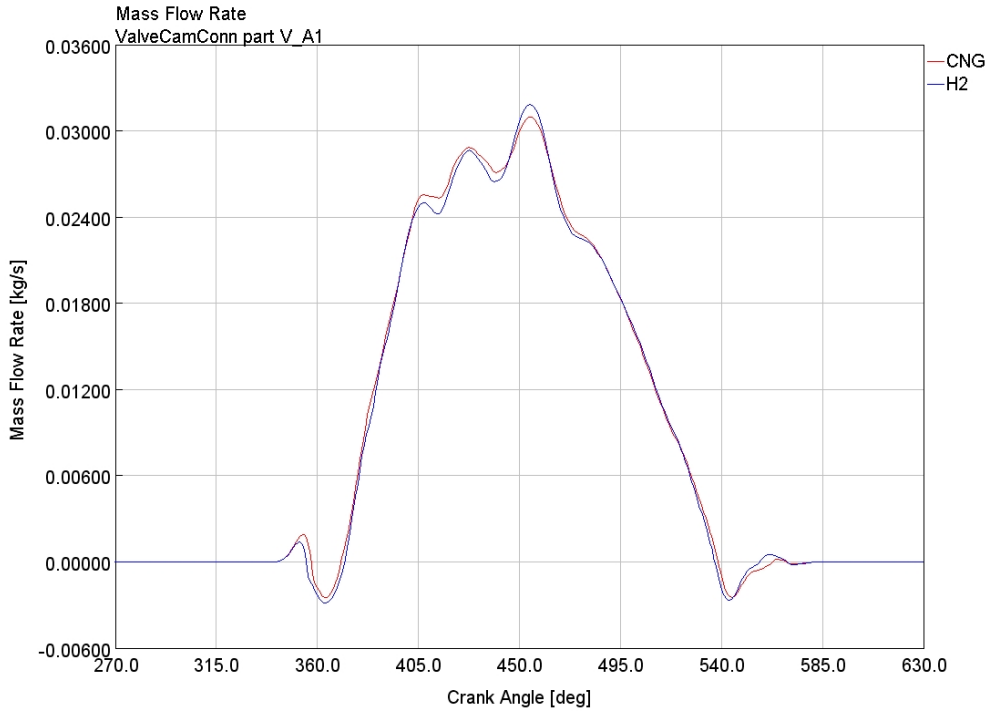

Figure 5-6: intake mass flow rate, CNG vs H2, working point (3)

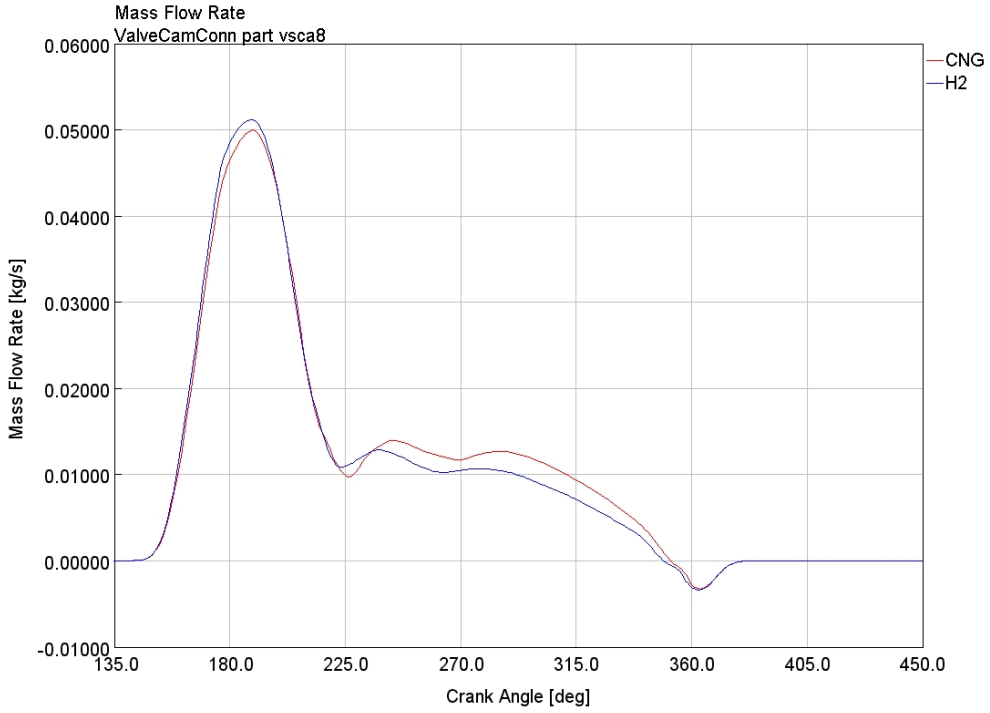

Figure 5-7: exhaust mass flow rate, CNG vs H2, working point (3)

Working point (3)	[]	Calibrated CNG	H2
Intake Manifold Pressure	[bar]	1.279	1.279
Intake Manifold Temperature	[K]	310	310
Fuel Flow Rate	[kg/h]	7.58	3.74
Air Flow Rate	[kg/h]	129	127
Target Boost Pressure	[bar]	1.279	1.279
Actual Boost Pressure	[bar]	1.279	1.279
Turbine Inlet Pressure	[bar]	1.377	1.361
Turbine Inlet Temperature	[K]	1050	1074
Turbine Outlet Pressure	[bar]	1.023	1.038
Turbine Outlet Temperature	[K]	1014	1095
Wastegate Diameter	[mm]	10.65	12.39
PFP cylinder 1	[bar]	90.12	108.55
CA at PFP cylinder 1	[deg]	12.36	11.79
Brake Torque	[Nm]	145.65	167.43
Brake Power	[HP]	51.14	58.78
Volumetric Efficiency (manifold)	[%]	87.7	86.3
BMEP	[bar]	13.38	15.38

Table 5-3: working point (3), CNG vs H2

Concerning working point (3), the considerations made while discussing the results related to working point (6) still hold.

In this case, with hydrogen, the PFP increases of about 20.5%, while the brake torque, brake power and bmep increase of about 14.9% with respect to CNG.

Concerning the increased pressure over the cycle and by referring to both working points (6) and (3), it has to be pointed out that, even if in the plots it is not reported the full engine cycle but only a portion in the vicinity of TDCF, the in-cylinder pressure with a hydrogen-air mixture starts to increase with respect to the CNG-air one at exactly start of injection (SOI) crank angle, consistently with the previously made considerations.

As far as working point (1) is concerned, some issues arose, as it is possible to notice in the results presented in the following. In particular, by adopting the injection delivery rate that came out from the simulations performed with the old injector template, the problems were related to the behavior of the turbocharger group and, as explained later on, solved by acting on the turbocharger controller template.

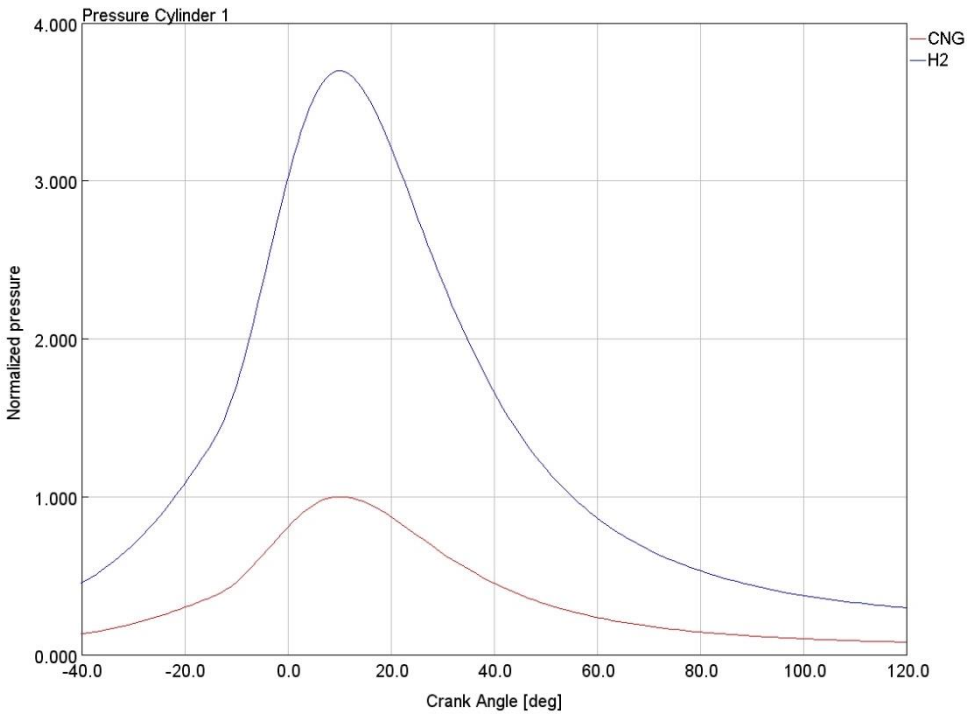

Figure 5-8: pressure cycle, CNG vs H2, working point (1)

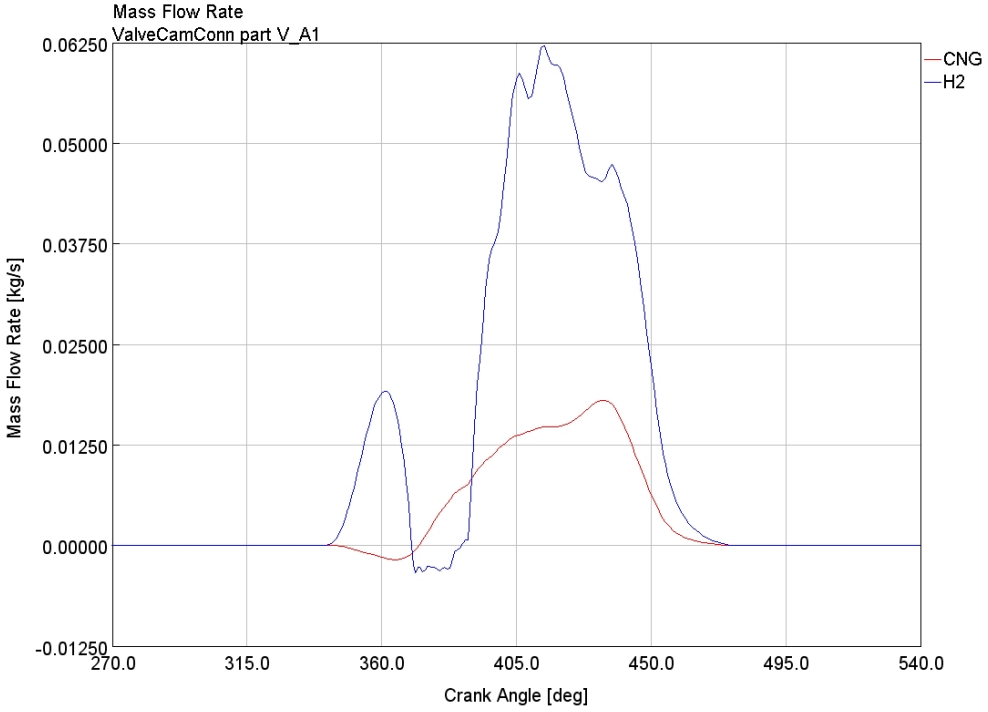

Figure 5-9: intake mass flow rate, CNG vs H2, working point (1)

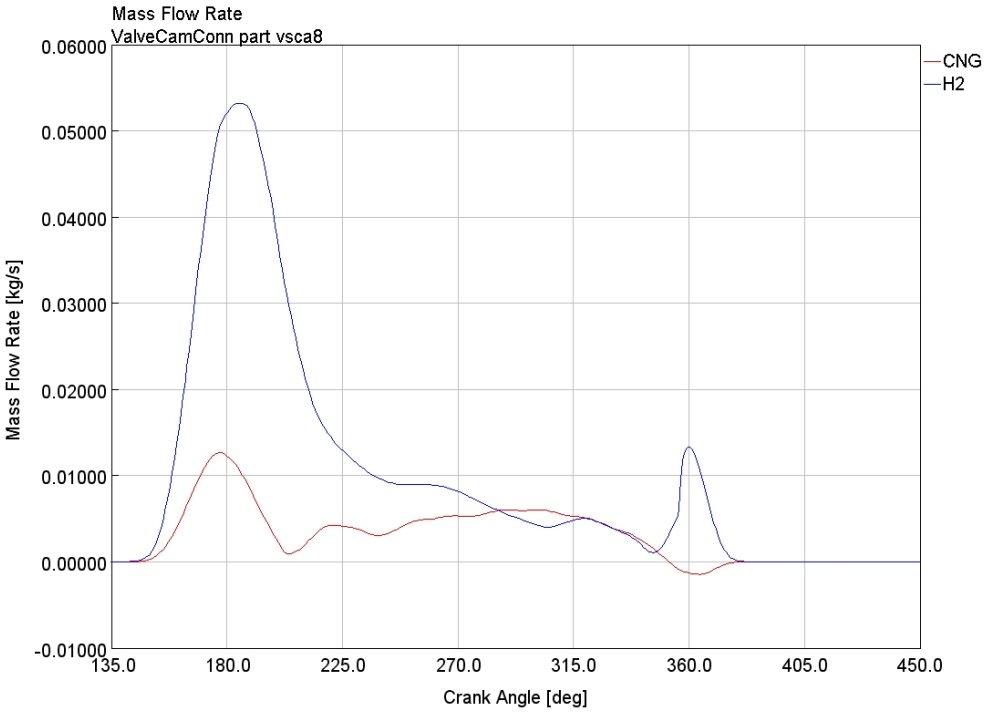

Figure 5-10: exhaust mass flow rate, CNG vs H2, working point (1)

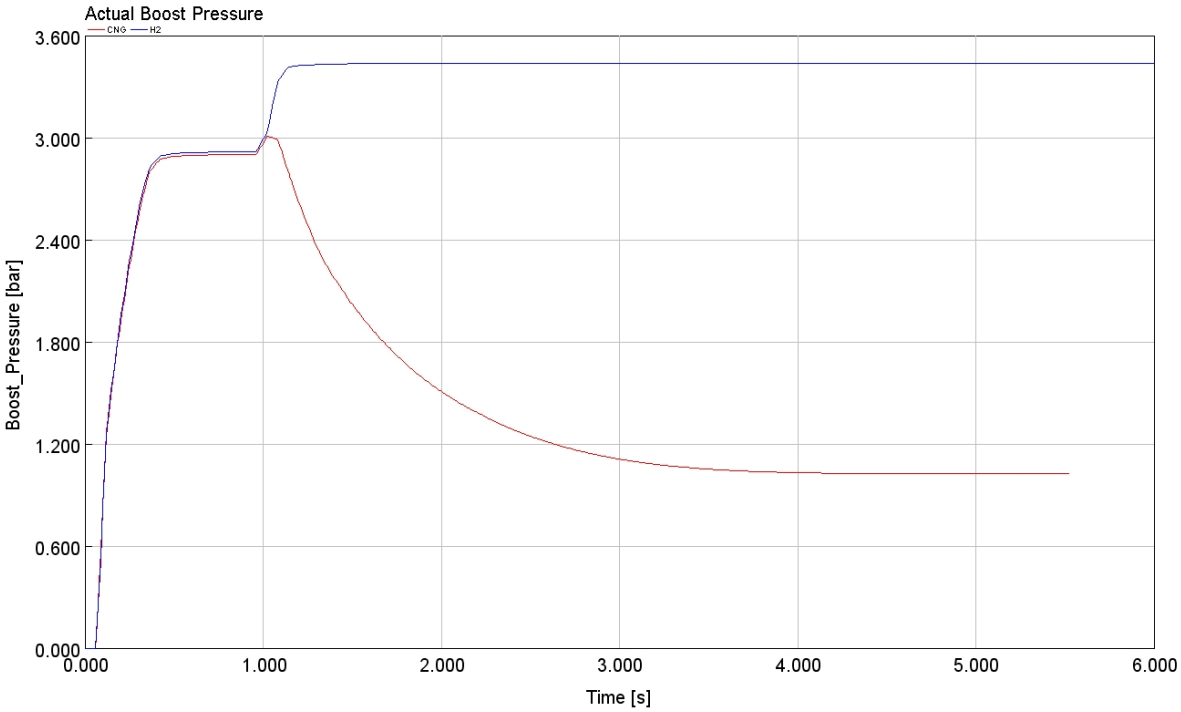

Figure 5-11: actual boost pressure, CNG vs H2, working point (1)

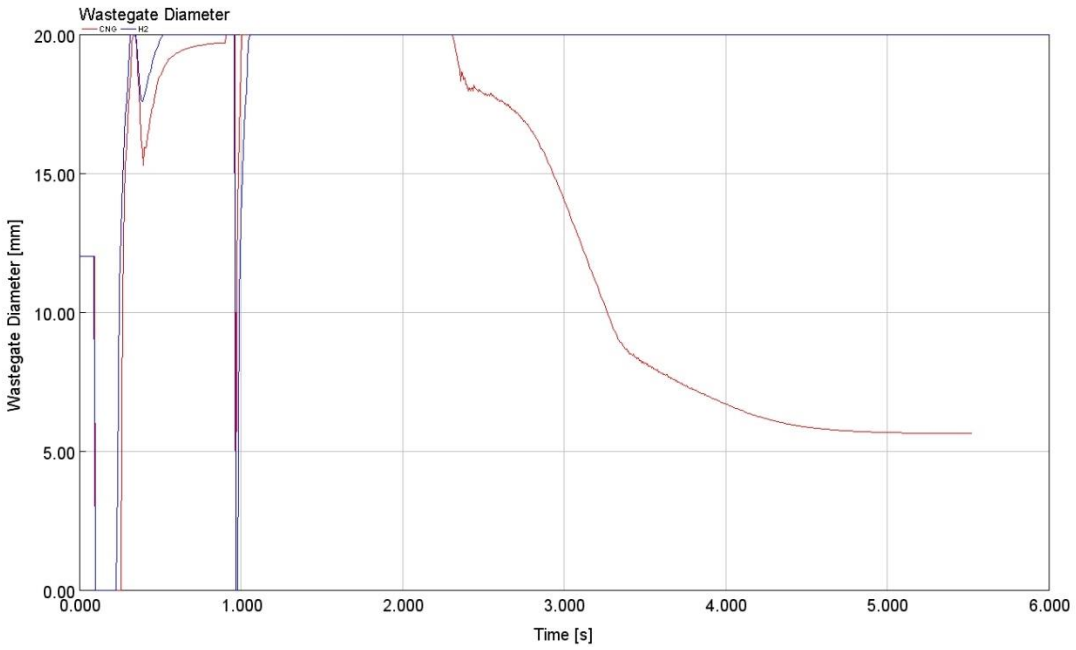

Figure 5-12: wastegate diameter, CNG vs H2, working point (1)

Working point (1)	[]	Calibrated CNG	H2
Intake Manifold Pressure	[bar]	1.024	3.435
Intake Manifold Temperature	[K]	310	310
Fuel Flow Rate	[kg/h]	2.15	3.75
Air Flow Rate	[kg/h]	37	127.6
Target Boost Pressure	[bar]	1.024	1.024
Actual Boost Pressure	[bar]	1.024	3.435
Turbine Inlet Pressure	[bar]	1.058	1.214
Turbine Inlet Temperature	[K]	931	1012
Turbine Outlet Pressure	[bar]	0.998	1.058
Turbine Outlet Temperature	[K]	918	1002
Wastegate Diameter	[mm]	5.63	20
PFP cylinder 1	[bar]	29.98	110.87

CA at PFP cylinder 1	[deg]	10.43	10.1
Brake Torque	[Nm]	43.4	214.6
Brake Power	[HP]	12.19	60.28
Volumetric Efficiency (manifold)	[%]	39.3	40.3
BMEP	[bar]	4	19.7

Table 5-4: working point (1), CNG vs H2

As it is possible to notice by looking at the previously reported results, switching from CNG to hydrogen leads to completely unacceptable results. The boost pressure provided by the turbocharger increases of about 235.45% with respect to the target one, the wastegate is saturated in open position, the peak firing pressure results to be 270% higher with respect to CNG and brake torque, brake power and bmep increases of about 394.5%. Moreover, despite the intake and exhaust valve lift profiles and the injector delivery rate is the same of the CNG cases, the outcomes are completely different. Before getting the conclusion that all these problems were related to the turbocharger controller template, studies about injector delivery rate sweeps and intake valve lift profiles have been carried out. For sake of completeness, the results of such analyses are reported in the following. Since in the end it came out that the problems were related neither to the delivery rate, nor the valve lift profile, only the results related to pressure cycles, normalized with respect to CNG, are presented. Later on, after the discussion about the turbocharger controller template, the final results are presented in terms of both pressure cycle and performances.

The injector delivery rate for this working point, coming from the previous model and leading to the previously presented results, was $\dot{m}_{inj} = 5.72\ g/s$.

A first sweep of delivery rate between $\dot{m}_{inj} = 2\ g/s$ and $\dot{m}_{inj} = 5.5\ g/s$ has been performed, so as to assess which could be the delivery rate interval in which the simulation started not to behave consistently, as presented in *Figure 5-13* and *Figure 5-14*.

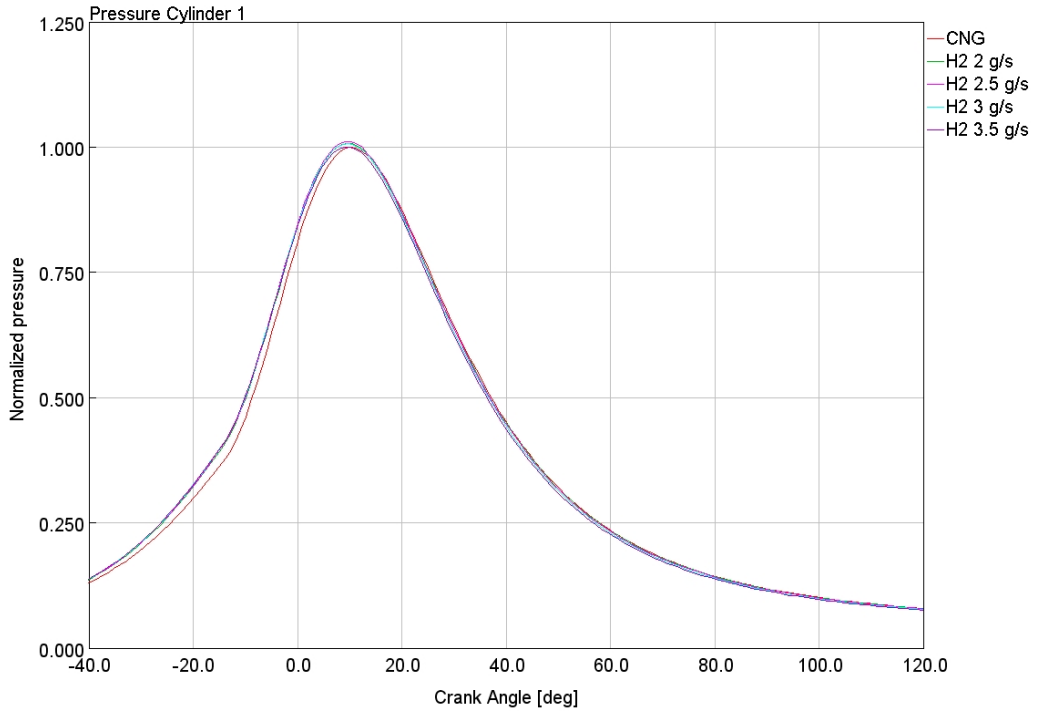

Figure 5-13: injector delivery rate sweep 2-3.5 g/s, working point (1)

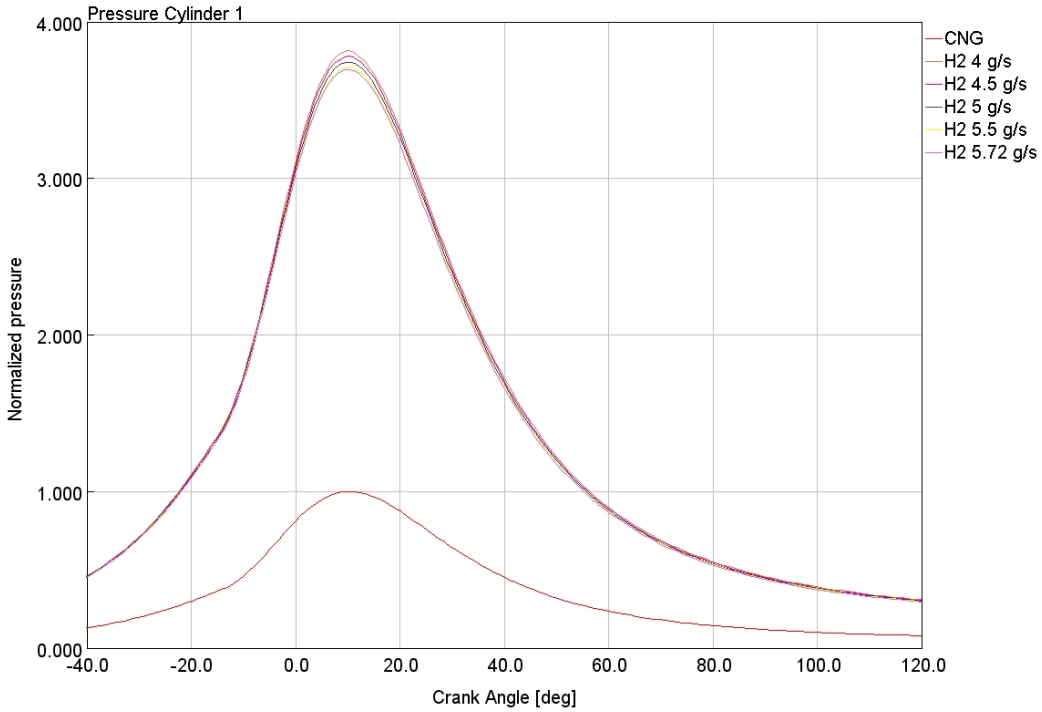

Figure 5-14: injector delivery rate sweep 4-5.72 g/s, working point (1)

Since the model seemed to start behaving unacceptably in an injector delivery rate interval comprised between $\dot{m}_{inj} = 3.5\ g/s$ and $\dot{m}_{inj} = 4\ g/s$, a more refined sweep between these two values have been performed. The results are presented in *Figure 5-15* and *Figure 5-16*.

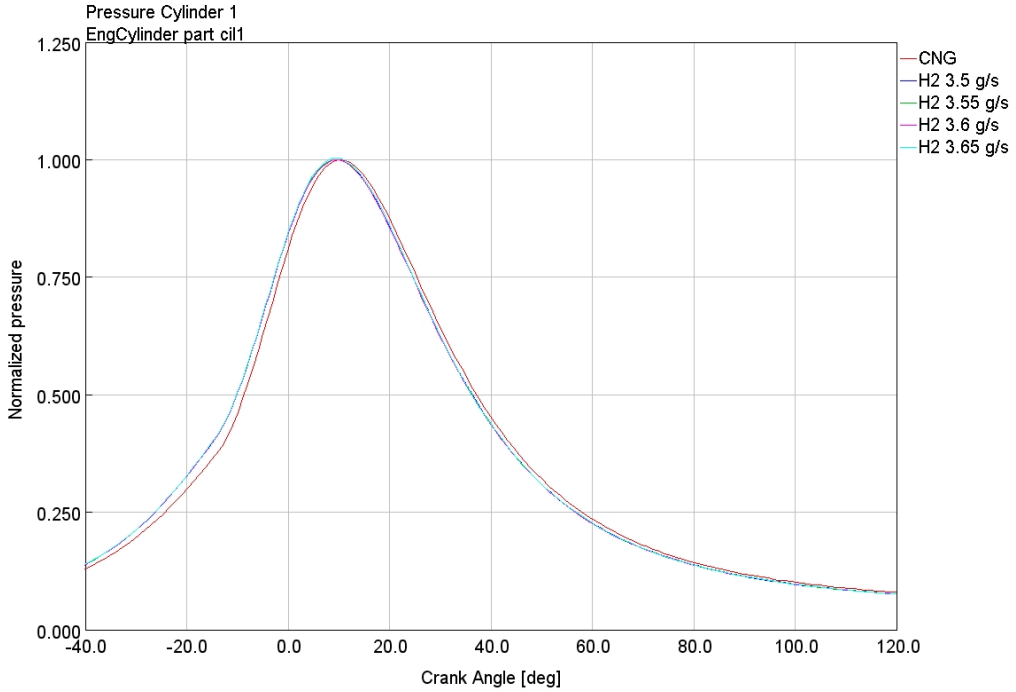

Figure 5-15: injector delivery rate sweep 3.5-65 g/s, working point (1)

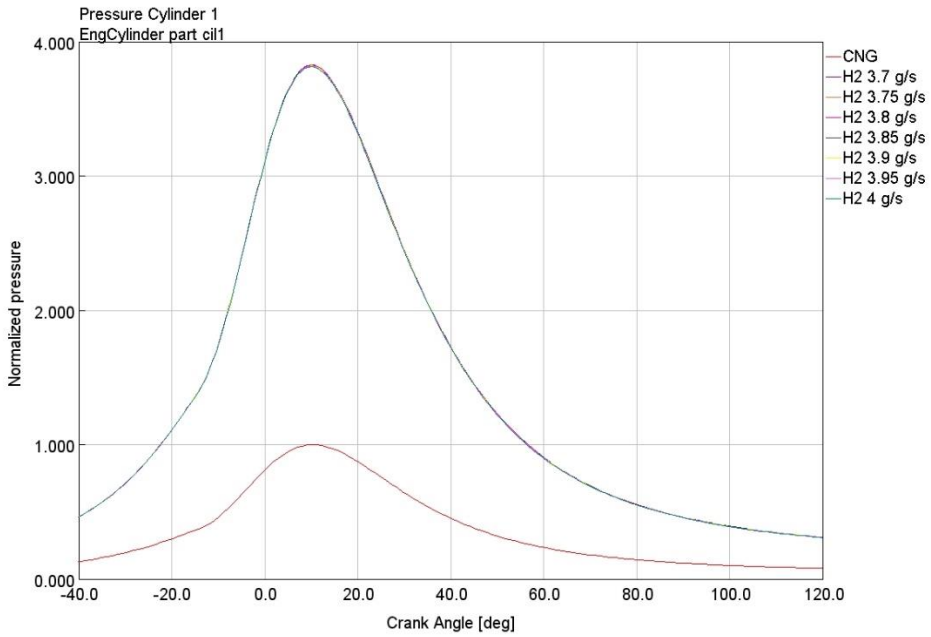

Figure 5-16: injector delivery rate sweep 3.7-4 g/s, working point (1)

As a consequence of such more refined sweep, it resulted that the injector delivery rate value that leads the model to behave in an unacceptable way is comprised between $\dot{m}_{inj} = 3.65\ g/s$ and $\dot{m}_{inj} = 3.7\ g/s$. At this point, since the reasons why such behavior was influenced by the injector delivery rate were not clear, it has been considered not significant to perform a further sweep refinement, but other analyses have been carried out. As previously mentioned, in particular, a sweep on the valve lift profile has been performed as well, as presented in *Figure 5-17* and *Figure 5-18*.

Such results are presented as follows. The pressure values are normalized with respect to the CNG, which displays its baseline intake valve lift profile. Each profile displays the same IVO but has different maximum lift and IVC values. For sake of confidentiality, the baseline profile has been labeled as $H_2\ ref$ (and it is the same of CNG case) and is characterized by its own IVC: the other profiles are labeled as $H_2\ ref \pm x$, where x is the difference between the baseline IVC and the IVC of the considered case.

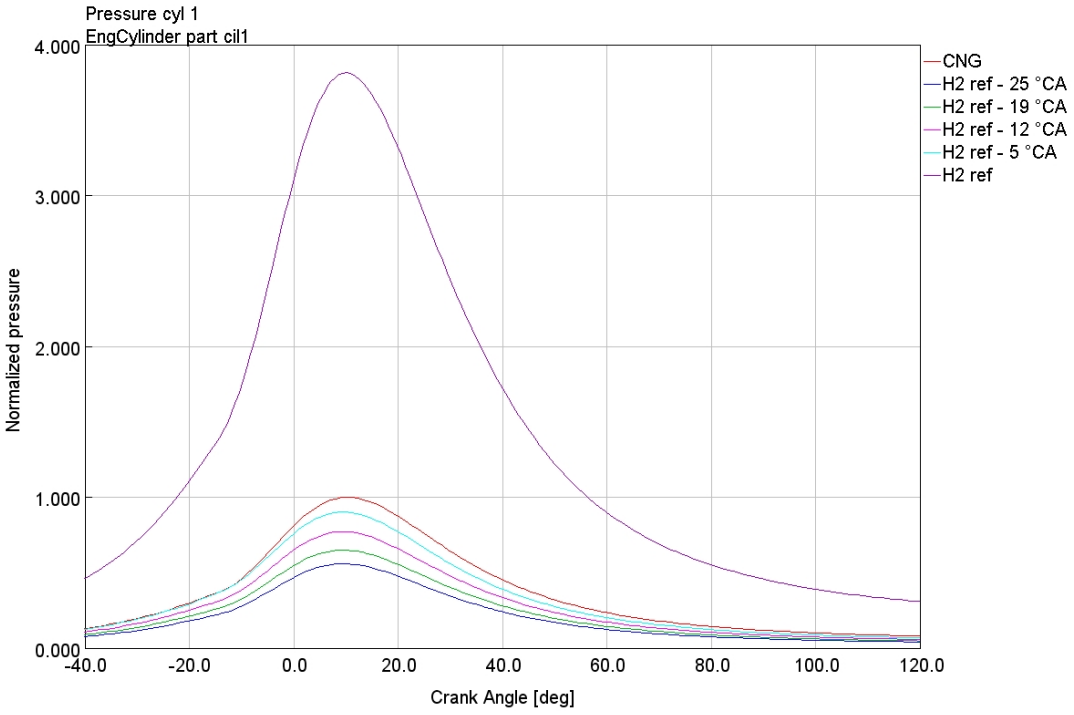

Figure 5-17: intake valve lift profile sweep, earlier IVC, working point (1)

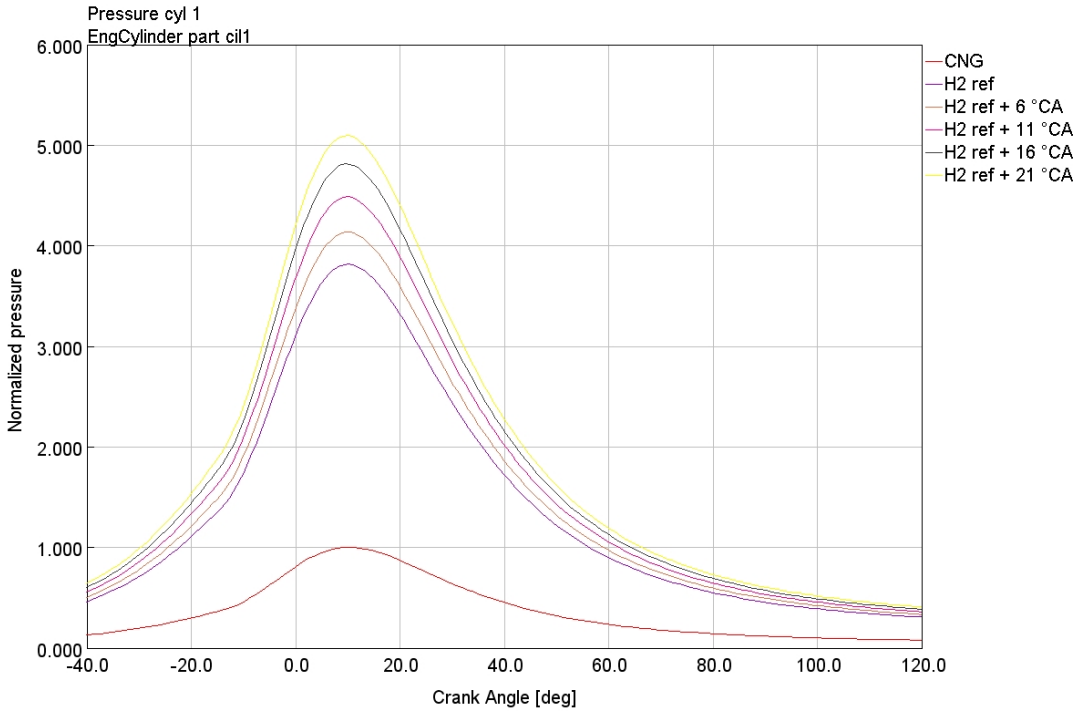

Figure 5-18: intake valve lift profile sweep, later IVC, working point (1)

It is possible to notice that the earlier is IVC, the lower is the pressure, even with respect to the CNG case. The comparison between the pressure cycle of CNG and hydrogen with the same intake valve lift profile is the same as presented in *Figure 5-8*. On the other hand, the latter is IVC, the higher is the pressure.

Even though all the problems were related to the turbocharger controller and solved by acting on it, these analyses have been useful to understand in which way it is possible to modify the stoichiometric hydrogen engine behavior in terms of pressure cycles and performances by acting on the delivery rate of the injectors and on the intake valve lift profiles.

In the GT-POWER model employed for the development of the thesis, the turbocharger is controlled by means of a template present in the library, that is called "ControllerTurboWG", rather than by a classic PID controller, even if it should work similarly.

In such a template, it is possible to set the variable that has to be controlled, which in this case is the boost pressure, and the desired target value. Moreover, the turbocharger group parameters such as minimum and maximum wastegate diameter, maximum revolution

speed, maximum opening and closing rate, as well as the convergence criteria can be set. By further analyzing the template, it is possible to find a parameter that is called "aggressiveness factor", that is defined as "*a multiplier to the measured error that gets reported to the controller".* This means that it has the same function that the gain *K* assumes in the context of a classic PID controller, that is the correction of the error measured by the controller that the output variable is as close as possible to the reference one that, in this case, is the boost pressure. The value originally set for the aggressiveness factor was equal to 1, that means that the control action is equal to the error itself.

By decreasing the aggressiveness factor to values lower than 1 the controller starts behaving properly because the error is finally corrected and the signals stabilized. By setting the aggressiveness factor to 0.8, which has been found to be the best value, the simulation results become consistent with the expected ones, both in terms of pressure cycles and performances, whichever injector delivery rate has been chosen. For first, a simulation ranging from the lowest value of the previously acceptable range, i.e. $\dot{m}_{inj} = 3.5\ g/s$, to the original one, i.e. $\dot{m}_{inj} = 5.72\ g/s$, has been performed. The results of these simulations, in terms of pressure cycles, are presented in *Figure 5-19.*

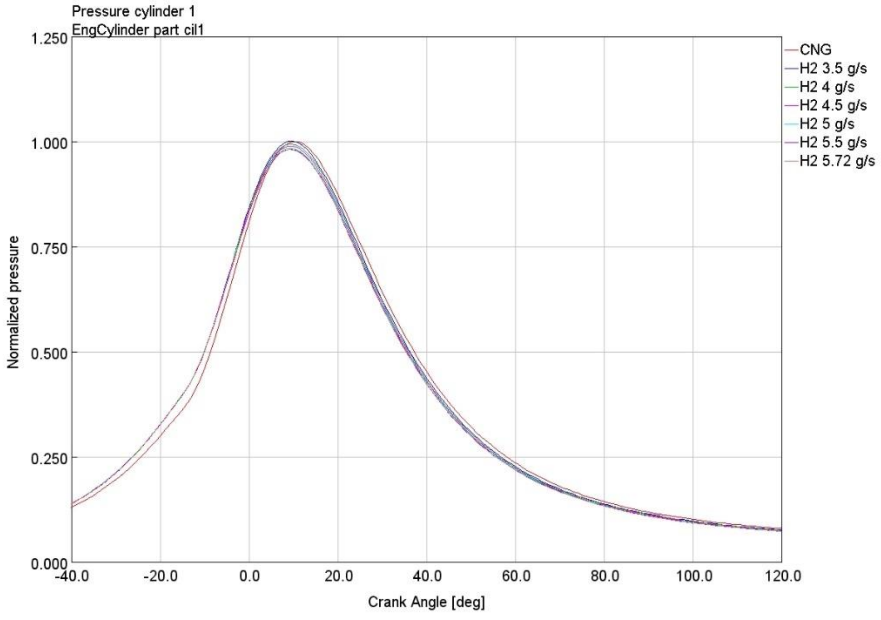

Figure 5-19: injector delivery rate sweep with aggressiveness factor=0.8

Once assessed the behavior of the model with such an aggressiveness factor, which has been

consistent for each considered delivery rate value, it has been decided to set the same base injector delivery rate of the other two considered working points, i.e. $\dot{m}_{inj} = 3.6\ g/s$, so as to evaluate the performances of the engine in working point (1), finally achieving satisfactory results, which are presented in the following.

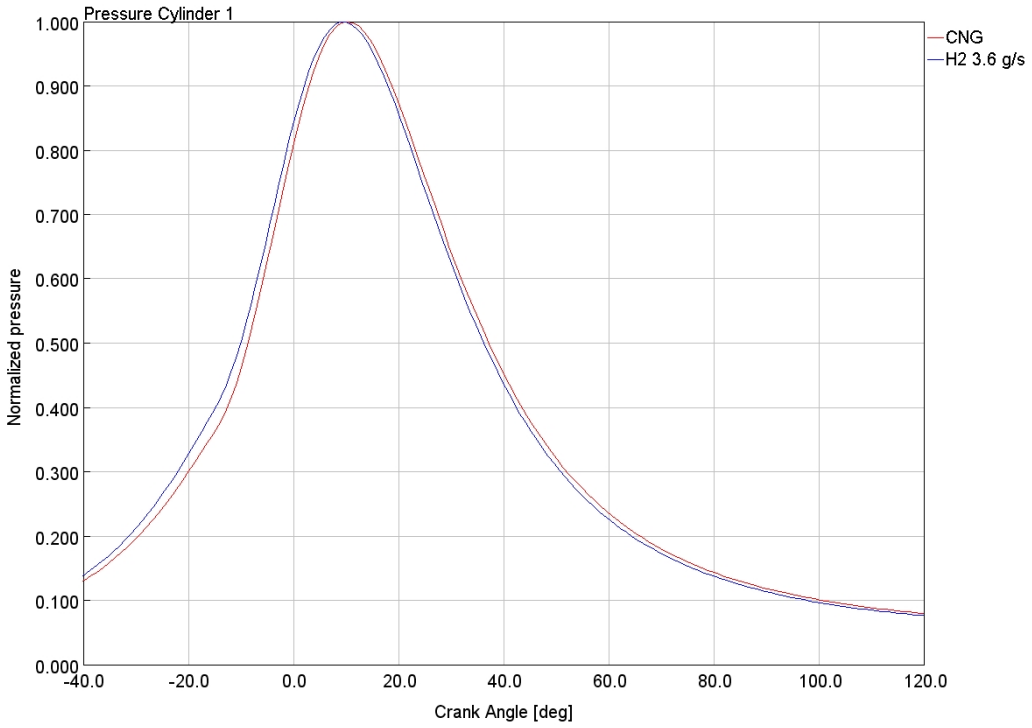

Figure 5-20: aggressiveness factor=0.8, delivery rate=3.6 g/s, working point (1)

Working point (1)	[]	CNG	$H_{2,st}$
Intake Manifold Pressure	[bar]	1.024	1.024
Intake Manifold Temperature	[K]	310	312
Fuel Flow Rate	[kg/h]	2.15	1.00
Air Flow Rate	[kg/h]	37	34
Target Boost Pressure	[bar]	1.024	1.024

Actual Boost Pressure	[bar]	1.024	1.024
Turbine Inlet Pressure	[bar]	1.058	1.057
Turbine Inlet Temperature	[K]	931	924
Turbine Outlet Pressure	[bar]	0.998	0.998
Turbine Outlet Temperature	[K]	918	911
Wastegate Diameter	[mm]	5.63	4.56
PFP cylinder 1	[bar]	29.98	29.97
CA at PFP cylinder 1	[deg]	10.43	9.48
Brake Torque	[Nm]	43.40	39.69
Brake Power	[HP]	12.19	11.15
Volumetric Efficiency (manifold)	[%]	39.30	36
BMEP	[bar]	3.99	3.65

Table 5-5: performances comparison between stoichiometric CNG/H2 mixtures, working point (1)

5.2. Hydrogen-air lean mixture: $\lambda = 2$

As discussed in chapter 1.2, it is difficult to run an internal combustion engine fueled with hydrogen adopting a stoichiometric mixture for different reasons. Due to the extremely high combustion temperature and flame speed values, for stoichiometric mixtures the NOx production is extremely high and abnormal combustion events, such as preignition and knock, are very likely to occur. If resorting, as in this case, to a DI configuration, the problem of backfire is of lower importance since, very often, the fuel is injected in the combustion chamber when the intake valve is closed. Moreover, it has been discussed that several countermeasures can be taken to face the emissions and combustion issues, such as the adoption of water cooled spark plugs, the use of EGR, turbocharging, charge cooling, VVT, a well-designed intake system and a proper exhaust aftertreatment system. These actions can be taken to keep the air-fuel ratio close to the stoichiometric one, reducing the occurrence of the abovementioned issues.

However, another path can be followed and this is what has been done to achieve the final objective of the present study. Since the NOx formation limit, that is defined as the relative air-fuel ratio (RAFR) below which the NOx formation raises to unacceptable values, occurs at $\lambda = 2$, for hydrogen fueled internal combustion engines' applications, several researches have been carried out to understand the feasibility of running the engine lean, that is physically possible due to the very low flammability limit of such a fuel, but that leads to significant decrease in performances if the only modified parameter when switching from stoichiometric to lean mixture is the air-fuel ratio.

The final objective, therefore, is the performance optimization of the reference engine when adopting $\lambda = 2$. To do this, several studies have been carried out, by analyzing the effects of changes of combustion phasing, injection timing, valve lift profiles and turbocharger group-related parameters. The steps leading to the final results are presented in the following and the final results are reported and discussed as well. For sake of simplicity, all the presented results refers to working point (6) only, that, as previously mentioned, is at 2000 rpm and full load conditions.

As very first step, the relative air-fuel ratio has been changed from $\lambda = 1$ to $\lambda = 2$ to assess the performance changes that would have occurred by switching from a stoichiometric mixture to a lean one.

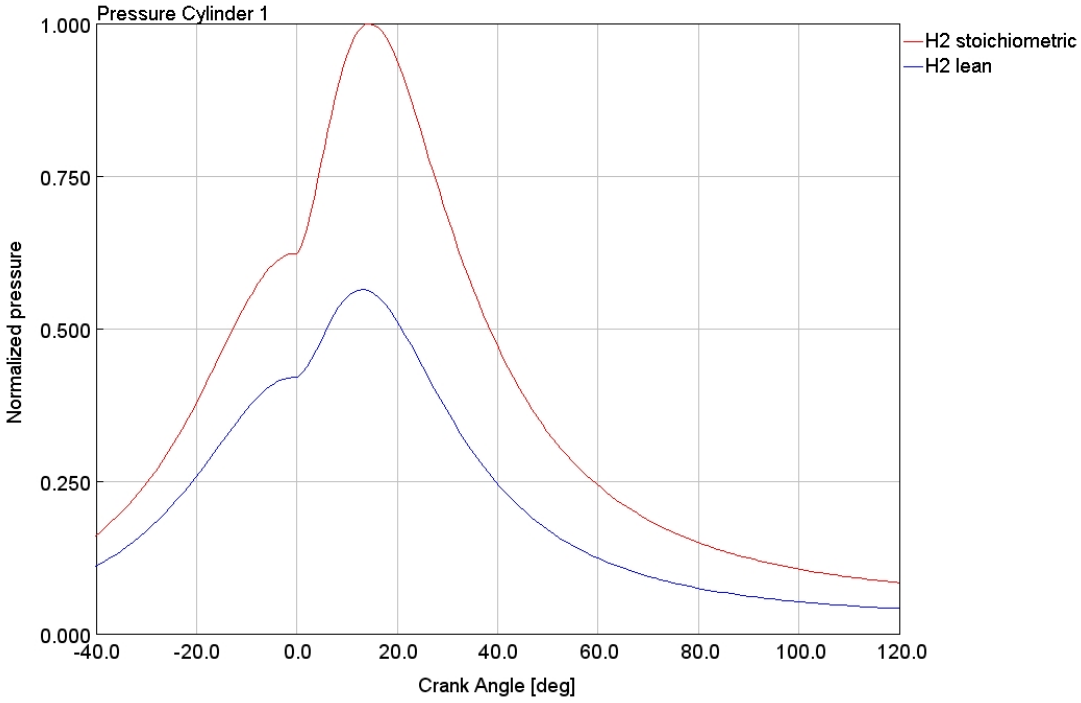

Figure 5-21: pressure cycle cylinder 1, H2 stoichiometric vs lean, working point (6)

Working point (6)	[]	$H_{2,st}$	$H_{2,lean}$
Intake Manifold Pressure	[bar]	1.741	1.391
Intake Manifold Temperature	[K]	354	354
Fuel Flow Rate	[kg/h]	3.81	1.52
Air Flow Rate	[kg/h]	129	103
Target Boost Pressure	[bar]	1.741	1.741
Actual Boost Pressure	[bar]	1.741	1.391
Turbine Inlet Pressure	[bar]	1.566	1.396
Turbine Inlet Temperature	[K]	1150	829

Turbine Outlet Pressure	[bar]	1.032	1.001
Turbine Outlet Temperature	[K]	1085	787
Wastegate Diameter	[mm]	8.92	0
PFP cylinder 1	[bar]	127.33	71.74
CA at PFP cylinder 1	[deg]	14.52	12.98
Brake Torque	[Nm]	215.26	87.08
Brake Power	[HP]	60.46	24.46
Volumetric Efficiency (manifold)	[%]	0.922	0.921
BMEP	[bar]	17.44	8

Table 5-6: H2 stochiometric vs lean comparison, working point (6)

As expected and previously anticipated, switching from a stoichiometric to a lean mixture leads to a strong decreases in performances. The peak firing pressure decreases of about 43.66% and the brake torque, brake power and bmep of about 54.13%. Moreover, the turbocharger is not able to reach the target boost pressure and the wastegate remains closed: this suggests that the in-cylinder temperatures reached during the combustion are too low, the enthalpy carried by the exhaust gas is too low and therefore the turbocharger is not able to work properly.

According to this last consideration, in order to optimize the performance of such a lean burn engine, i.e. to significantly increase the brake mean effective pressure, brake torque and brake power, the effect of the combustion phasing and the turbocharger characteristics have been investigated. Despite studies about modifications in valve lift profiles and injection timing have been carried out, they did not led to significant improvements and results. For this reason, they are not reported in the present dissertation.

As abovementioned, the most important aspects to be investigated were the combustion phasing and the turbocharger characteristics and behavior. The first analysis that has been carried out concerned the modifications of the combustion duration and the anchor angle so that to postpone the combustion, in order to increase the exhaust gas temperature and enthalpy to try to achieve a proper turbocharger behavior and then to increase the bmep.

The baseline characteristics of the H_2 lean model, that are the starting point for all the subsequent analyses, are reported in *Table 5-7*.

Baseline $H_{2,lean}$		
MFB50	[CA aTDCF]	11.52
Duration	[CA]	20
SOI	[CA]	545
Target boost pressure	[bar]	1.7413
Bmep	[bar]	8

Table 5-7: hydrogen lean model, cylinder 1 baseline, working point (6)

While increasing either the anchor angle or the combustion duration with respect to the baseline, without modifying any other parameter, leads to negligible increase of the performances, as presented from *Table 5-8* to *Table 5-12*, by increasing both it is possible to achieve more significant improvements.

Duration sweep							
Duration	[CA]	20	21	22	23	24	25
Bmep	[bar]	8	8.04	8.06	8.08	8.09	8.1

Table 5-8: sweep on combustion duration

MFB50 sweep					
MFB50	[CA]	7.5	8	8.5	9
Bmep	[bar]	7.52	7.58	7.64	7.71

Table 5-9: MFB50 sweep, cylinder 1, working point (6), part 1

MFB50 sweep					
MFB50	[CA]	9.5	10	10.5	11
Bmep	[bar]	7.77	7.84	7.9	7.97

Table 5-10: MFB50 sweep, cylinder 1, working point (6), part 2

MFB50 sweep					
MFB50	[CA]	11.5	12	12.5	13
Bmep	[bar]	8	8.08	8.13	8.18

Table 5-11: MFB50 sweep, cylinder 1, working point (6), part 3

MFB50 sweep					
MFB50	[CA]	13.5	14	14.5	15
Bmep	[bar]	8.23	8.29	8.34	8.39

Table 5-12: MFB50 sweep, cylinder 1, working point (6), part 4

As anticipated, by increasing both the anchor angle e the combustion duration it is possible to achieve much better results: since 6 sweeps with an overall number of MFB50-duration couples equal to 64 have been performed, for sake of brevity only the results coming from the couples of parameters that led to the better outcomes are presented from *Table 5-13* to *Table 5-15*.

MFB50 and duration sweep						
Duration	[CA]	37	37.5	38	38.5	39
MFB50	[CA]	20	21	22	23	24
Bmep	[bar]	9.26	9.37	9.49	9.62	9.76

Wastegate diameter	[mm]	0	0	0	0	0
BSFC	[g/kWh]	84.85	85.24	85.67	86.15	86.66
PFP	[bar]	68.58	68.12	67.75	67.53	67.65

Table 5-13: MFB50 and combustion duration sweep, cylinder 1, working point (6), part 1

MFB50 and duration sweep						
Duration	[CA]	39.5	40	40.5	41	41.5
MFB50	[CA]	25	26	27	28	29
Bmep	[bar]	9.7	9.6	9.5	9.4	9.3
Wastegate diameter	[mm]	1.12	1.59	1.95	2.25	2.51
BSFC	[g/kWh]	87.42	88.25	89.14	90.1	91.1
PFP	[bar]	67.8	67.79	67.79	67.78	67.77

Table 5-14: MFB50 and combustion duration sweep, cylinder 1, working point (6), part 2

MFB50 and duration sweep					
Duration	[CA]	42	42.5	43	43.5
MFB50	[CA]	30	31	32	33
Bmep	[bar]	9.2	9.1	8.98	8.85
Wastegate diameter	[mm]	2.75	2.97	3.17	3.36
BSFC	[g/kWh]	92.14	93.23	94.39	95.59
PFP	[bar]	67.77	67.76	67.76	67.75

Table 5-15: MFB50 and combustion duration sweep, cylinder 1, working point (6), part 3

As it is possible to notice by looking at the previous results, the performances started to increase despite the boost pressure was kept the same as the baseline one and the wastegate valve, for some of the considered combustion phasing values, started to open. This indicates that the combustion temperature and the exhaust gas enthalpy started to increase but not enough to be able to make the turbocharger group working properly, since in many points the wastegate valve was still closed.

For this reason, the subsequent step was that of analyzing the turbocharger group. In the turbine template of the GT-POWER model, there are two important parameters: the *mass multiplier* and the *efficiency multiplier*, by means of which it is possible in a very flexible way to operate analyses about the turbine design characteristics. The *mass multiplier* parameter is used to scale the turbine map mass flow rate: the code calculates the instantaneous pressure ratio and the speed and looks up the mass flow rate in the map, which is then multiplied by this parameter. In the original model, it was set equal to 1, meaning that the mass flow rate across the turbine was the one corresponding to the pressure ratio-speed couple which can be found in the turbine map. To set a mass multiplier lower than 1, as it has been done, physically means to evaluate the effect of reducing the turbine size, which lead to get a boost increase due to the increased backpressure. Nonetheless, a smaller turbine could cause problems at the higher speeds. The *efficiency multiplier* parameter is used to scale the turbine map efficiency: the code calculates the instantaneous pressure ratio and the speed and looks up the efficiency in the map, which is then multiplied by this parameter that, in the original model, it was set equal to 1. With the aim of optimizing the engine performance, the efficiency multiplier has been set equal to 1.3, that physically means to consider a turbine with an efficiency improved of 30%. The study about the effects of changing this parameter leads to understand which is the useful target efficiency to achieve the desired behavior. Once the target efficiency has been assessed, it could be necessary to revise the aerodynamic characteristics of the turbine (number of blades, angles, surface finishing and so on) or even to substitute the original turbocharger with another one.

Due to these considerations, the *mass multiplier* value has been changed from 1 to 0.8 and the *efficiency multiplier* value from 1 to 1.3.

By so doing and by considering the anchor angle-combustion duration couples reported from *Table 5-13* to *Table 5-15*, the results presented from *Table 5-16* to *Table 5-18* have been obtained.

MFB50 and duration sweep						
Duration	[CA]	37	37.5	38	38.5	39
MFB50	[CA]	20	21	22	23	24
Bmep	[bar]	10.08	10.01	9.93	9.85	9.77
Wastegate diameter	[mm]	6.24	6.33	6.43	6.52	6.61
BSFC	[g/kWh]	84.13	84.72	85.35	86.03	86.78
PFP	[bar]	74.01	72.27	70.63	69.09	67.82

Table 5-16: MFB50 and combustion duration sweep with mass_mult=0.8 and eff_mult=1.32, cylinder 1, working point (6), part 1

MFB50 and duration sweep						
Duration	[CA]	39.5	40	40.5	41	41.5
MFB50	[CA]	25	26	27	28	29
Bmep	[bar]	9.68	9.58	9.49	9.38	9.28
Wastegate diameter	[mm]	6.7	6.79	6.88	6.96	7.05
BSFC	[g/kWh]	87.57	88.42	89.31	90.26	91.26
PFP	[bar]	67.81	67.81	67.8	67.8	67.79

Table 5-17: MFB50 and combustion duration sweep with mass_mult=0.8 and eff_mult=1.32, cylinder 1, working point (6), part 2

MFB50 and duration sweep					
Duration	[CA]	42	42.5	43	43.5
MFB50	[CA]	30	31	32	33
Bmep	[bar]	9.17	9.06	8.95	8.84
Wastegate diameter	[mm]	7.13	7.22	7.3	7.38
BSFC	[g/kWh]	92.31	93.42	94.58	95.78
PFP	[bar]	67.79	67.78	67.77	67.77

Table 5-18: MFB50 and combustion duration sweep with mass_mult=0.8 and eff_mult=1.32, cylinder 1, working point (6), part 3

Apart from the further increased bmep with respect to the results related to the same combustion phasing but with the previous turbocharger, the most important aspect to be underlined is that, in these cases, the wastegate valve opens to a large extent even if the target boost pressure has been kept the same as the baseline, that was $p_{boost,target} = 1.741\ bar$. This means that, with this configuration, there was the possibility to increase the target boost pressure to optimize the engine performances, since the turbocharger started to properly work. This fact, in turn, means that the original turbocharger was not suitable for this engine to run with a hydrogen lean mixtures.

By considering the first combustion phasing parameters presented in *Table 5-16*, that is $\Delta\theta_{10\%-90\%} = 37\ °CA$ and $MFB50 = 20\ °CA$, which led to obtain $bmep = 10.08\ bar$ and $PFP = 74.01\ bar$ by employing $mass\ multiplier = 0.8$ and $efficiency\ multiplier = 1.32$, two additional cases have been considered.

The target boost pressure was increased to $p_{boost,target} = 2.5\ bar$ in the first case and to $p_{boost,target} = 3\ bar$ in the second case: the results obtained with such configurations and the comparison with the results from CNG stoichiometric and the very first case of H_2 lean are presented in *Table 5-19* and *Table 5.20* and discussed in the following.

Working point (6)	[]	Calibrated CNG	$H_{2,lean}$ Boost=2.5 bar	$H_{2,lean}$ Boost=3 bar
Intake Manifold Pressure	[bar]	1.741	2.499	2.915
Intake Manifold Temperature	[K]	354	354	354
Fuel Flow Rate	[kg/h]	7.79	2.82	3.29
Air Flow Rate	[kg/h]	132	192	224
Target Boost Pressure	[bar]	1.741	2.5	3
Actual Boost Pressure	[bar]	1.741	2.499	2.915
Turbine Inlet Pressure	[bar]	1.622	2.348	2.763
Turbine Inlet Temperature	[K]	1069	919	925
Turbine Outlet Pressure	[bar]	1.022	1.024	1.031
Turbine Outlet Temperature	[K]	1002	802	783
Wastegate Diameter	[mm]	6.18	4.6	3.95
PFP cylinder 1	[bar]	106.06	108.6	127.7
CA at PFP cylinder 1	[deg]	15.31	9.84	9.61
Brake Torque	[Nm]	189.83	165.89	195.87
Brake Power	[HP]	53.32	46.59	55.01

Volumetric Efficiency (manifold)	[%]	0.941	0.952	0.954
BMEP	[bar]	17.44	15.24	17.99
BSFC	[g/kWh]	195.84	81.13	80.3
LHV	[MJ/kg]	45.8	119.7	119.7
ESFC	[MJ/kWh]	8.97	9.71	9.61

Table 5-19: comparison between CNG calibrated model, H2 lean model with boost pressure=2.5 bar and H2 lean model with boost pressure=3 bar, with the best combustion phasing configuration

Working point (6)	[]	H2,lean	$H_{2,lean}$ Boost=2.5 bar	$H_{2,lean}$ Boost=3 bar
Intake Manifold Pressure	[bar]	1.391	2.499	2.915
Intake Manifold Temperature	[K]	354	354	354
Fuel Flow Rate	[kg/h]	1.52	2.82	3.29
Air Flow Rate	[kg/h]	103	192	224
Target Boost Pressure	[bar]	1.741	2.5	3
Actual Boost Pressure	[bar]	1.391	2.499	2.915
Turbine Inlet Pressure	[bar]	1.396	2.348	2.763
Turbine Inlet Temperature	[K]	829	919	925

Turbine Outlet Pressure	[bar]	1.001	1.024	1.031
Turbine Outlet Temperature	[K]	787	802	783
Wastegate Diameter	[mm]	0	4,6	3.95
PFP cylinder 1	[bar]	71.74	108.6	127.7
CA at PFP cylinder 1	[deg]	12.98	9.84	9.61
Brake Torque	[Nm]	87.08	165.89	195.87
Brake Power	[HP]	24.46	46.59	55.01
Volumetric Efficiency (manifold)	[%]	0.921	0.952	0.954
BMEP	[bar]	8	15.24	17.99
BSFC	[g/kWh]	83.22	81.13	80.3
LHV	[MJ/kg]	119.7	119.7	119.7
ESFC	[MJ/kWh]	9.96	9.71	9.61

Table 5-20: comparison between the very first H2 lean model, H2 lean model with boost pressure=2.5 bar and H2 lean model with boost pressure=3 bar, with the best combustion phasing configuration

By comparing the results coming from the CNG calibrated model and the last results obtained with hydrogen, $\lambda = 2$ and $p_{boost,target} = 2.5\ bar$ and the abovementioned values of mass multiplier and efficiency multiplier, it is possible to notice that a great improvement has been achieved with respect to the lean case in which no parameter has been modified except the air-fuel ratio. The results of the calibrated CNG model and lean hydrogen model became closer with a bmep, brake torque and brake power decrease of 12% compared with the 54% of the non-optimized configuration. Moreover, the peak firing pressure increases of about 2.4%. By comparing the results coming from the CNG calibrated model and the last results obtained with hydrogen, $\lambda = 2$ and $p_{boost,target} = 3\ bar$ and the

abovementioned values of mass multiplier and efficiency multiplier, even greater improvements can be achieved with an increase in bmep, brake torque and brake power of about 3%. The potential problem in this case is that the peak firing pressure increases a lot and therefore the mechanical characteristics of the engine should be revised by the designers. Moreover, it is important to notice that the modifications made on the turbine caused the fluid dynamics evolution of the flow across the turbine itself to become consistent with the experimental data. In chapter 4, the problems related to the fluid flow across the turbine were discussed, in particular concerning the temperature values and temperature drops. Thus, the problems related to the turbocharger in the model have been solved as well. Last, it is important to consider a parameter that is used to compare the energy consumption of different engines, that is called *energy specific fuel consumption,* defined by:

$$ESFC = BSFC \cdot LHV \tag{5.6}$$

By looking at the results, it comes out that the ESFC of the hydrogen lean mixture with target boost pressures of 2.5 bar and 3 bar increases with respect to CNG of 8.25% and 7.13%, respectively. In terms of emissions, this is not a great issue in the sense that NOx emissions are kept low due to the employed air-fuel ratio and CO_2 emissions are null in any case. The problem that can arise is the range coverable with such an engine with respect to the other fuel.

The pressure cycle of such an engine model simulation is presented in *Figure 5-22*: the shape of the pressure cycle curves are different with respect to the CNG and previously presented hydrogen stoichiometric and lean mixtures one due to the fact that the combustion phasing has been modified.

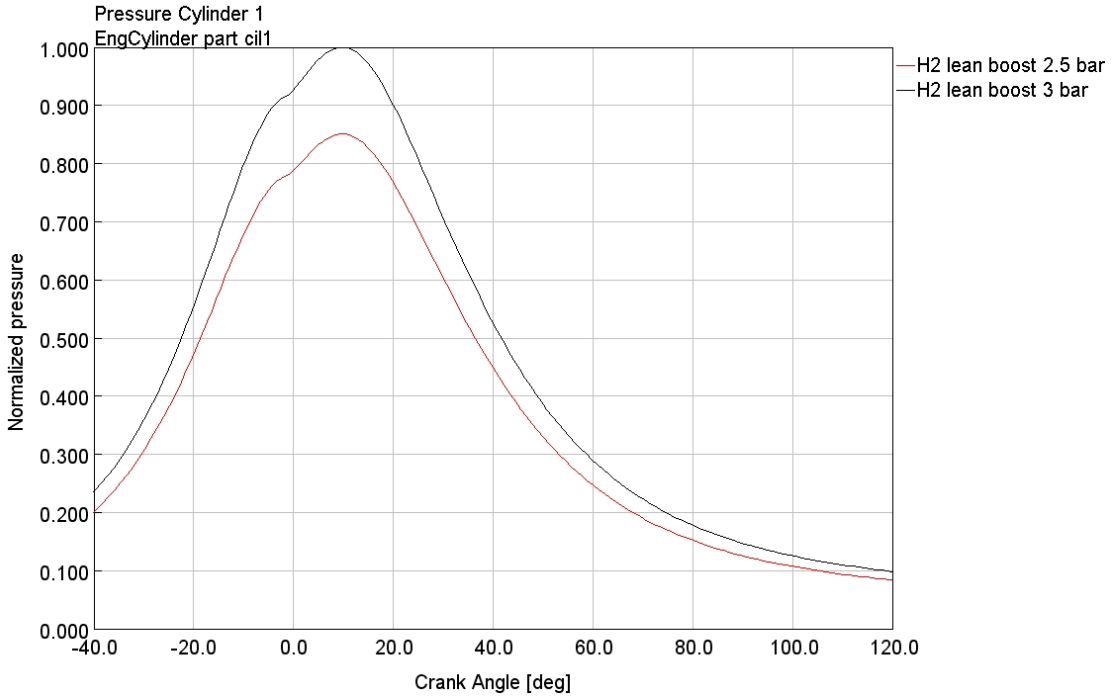

Figure 5-22: pressure cycle of optimized hydrogen-air lean mixtures

Last, it is interesting to notice, as presented in *Figure 5.23*, the peak firing pressure tends to increase as a function of bmep.

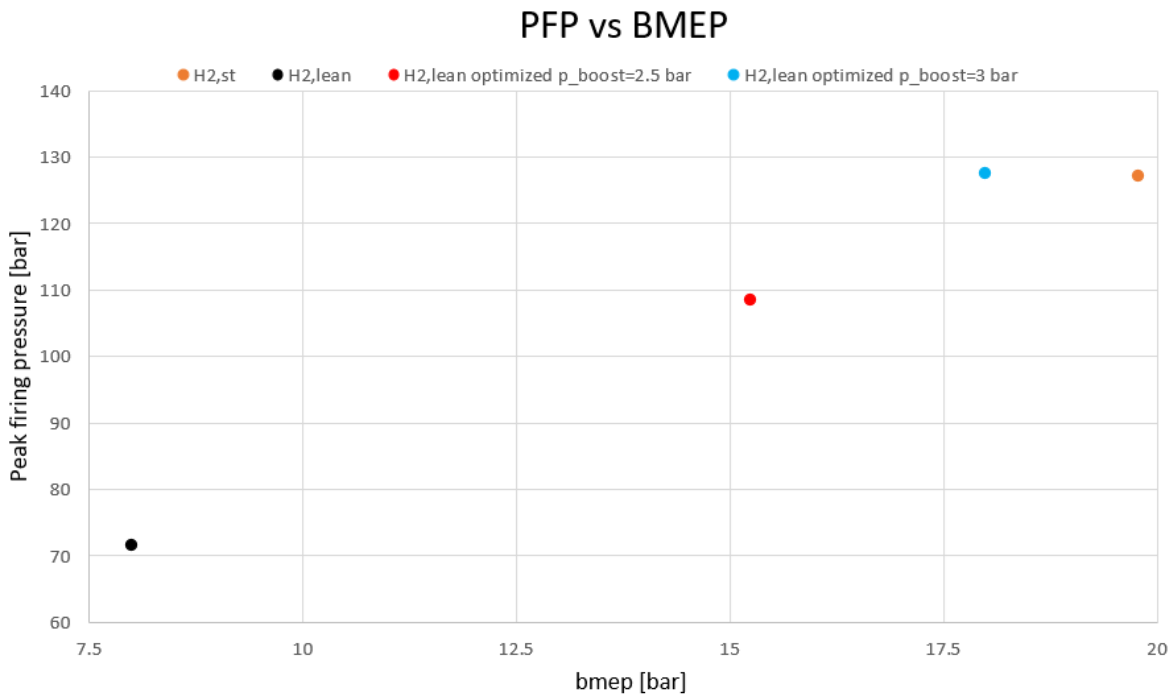

Figure 5-23: PFP as a function of bmep, hydrogen

6. Summary and conclusions

This project started from an existing CNG DI turbocharged internal combustion engine and from the results of a research previously carried out by AVL, CRF and Politecnico di Torino. The experimental data and the GT-POWER model were available.

The final objective of the present thesis was to assess and demonstrate the feasibility of running the reference engine with hydrogen and then to optimize its performances when using a lean mixture so that to drastically reduce the NOx emissions and to eliminate CO_2 emissions, being this latter aspect valid even when considering a stoichiometric mixture.

As mentioned in the introduction, this project has been developed to propose a valid alternative to the increasing tendency towards the electrification of road vehicles and to demonstrate that internal combustion engines, despite the recent decisions coming from the European Parliament which prescribe to completely ban internal combustion engines starting from 2035, have still the possibility to play an important role in a green mobility scenario, contemporarily following the path towards decarbonization and climate risks reduction.

The very first step was to calibrate the abovementioned GT-POWER CNG model and to validate it against the available experimental data, goal which has been successfully reached.

Secondly, the switch from stoichiometric air-CNG to stoichiometric air-hydrogen mixtures has been performed and the effects of this change on the engine behavior and characteristics have been investigated.

Thirdly, the switch from stoichiometric air-hydrogen to lean air-hydrogen mixtures has been performed due to the previously explained reasons.

Last, starting from the results coming from the very first lean-burn model simulations, an optimization of the engine performances, which resulted to be very close to the original CNG engine ones, has been successfully achieved, by acting on the combustion phasing and on the turbocharger group.

Undoubtedly, internal combustion engines run with green fuels can be a valid alternative to the complete road mobility electrification.

7. Bibliography

[1] S. Verhelst, R. Sierens. *Hydrogen engine-specific properties*. International Journal of Hydrogen Energy 26 (2001) 987-990.

[2] C.M. White, R.R. Steeper, A.E. Lutz. *The hydrogen-fueled internal combustion engine: a technical review*. International Journal of Hydrogen Energy 31 (2006) 1292-1305.

[3] Drell I.L., Belles F.E. *Survey of hydrogen combustion properties*. Technical Report 1383. National Advisory Committee on Aeronautics, 1958.

[4] L.M. Das. *Hydrogen-oxygen reaction mechanism and its implication to hydrogen engine combustion*. International Journal of Hydrogen Energy 21 (1996) 703-715.

[5] A. Mohammadi, M. Shioji, Y. Nakai, W. Ishikura, E. Tabo. *Performance and combustion characteristics of a direct injection SI hydrogen engine*. International Journal of Hydrogen Energy 32 (2007) 296-304.

[6] G.A. Karim. *Hydrogen as a spark ignition engine fuel*. International Journal of Hydrogen Energy 28 (2003) 569-577.

[7] M. Ciniviz, H. Köse. *Hydrogen use in internal combustion engine: a review*. International Journal of Automotive Engineering and Technologies 1 (2012) 1, 1-15.

[8] S. Verhelst, S. Verstraeten, R. Sierens. *A comprehensive overview of hydrogen engine design features*. Proc. IMechE Vol.221 Part D: J. Automobile Engineering.

[9] H.L. Yip, A. Srna, A.C.Y. Yuen, S. Kook, R.A. Taylor, G.H. Yeoh, P.R. Medwell, Q.N. Chan. *A review of hydrogen direct injection for internal combustion engines: towards carbon-free combustion*. Applied Sciences 2019, 9, 4842.

[10] Catania A.E; Misul D; Mittica A., Spessa E., 2000 SAE Trans., vol 109; p. 1610-1620, 2001.

[11] Ferrari G. (2016). *Motori a combustione interna*, casa editrice Esculapio.

[12] Heywood J.B. *Internal combustion engine fundamentals*.

[13] Semin and R. Abu Bakar. *A Technical Review of Compressed Natural Gas as an Alternative Fuel for Internal Combustion Engines*. American J. of Engineering and Applied Sciences 1 (4): 302-311, 2008.

[14] K. Bhandari, A. Bansal, A. Shukla and M. Khare. *Performance and emissions of natural gas fueled internal combustion engine: A review*. American J. of Engineering and Applied Sciences 1 (4): 302-311, 2008.

8. Acknowledgments

Giunto al termine del mio percorso universitario, voglio dedicare qualche riga alle persone a me più care, che mi hanno accompagnato durante questa lunga e importante esperienza.

Innanzitutto ringrazio la mia famiglia: mia madre Santuzza, mio padre Roberto e Andrea, che è come un padre per me. I momenti di difficoltà, anche importanti, sono stati numerosi durante questi anni e ognuno di loro, a modo suo, mi ha sempre supportato, ha tifato per me e mi è stato vicino, nonostante tutto. Sono convinto che, senza di loro, non sarei riuscito ad arrivare fino a qui.

Voglio poi dedicare un enorme ringraziamento alla mia ragazza Arianna, dalla quale ho imparato moltissimo, che mi è stata accanto nei momenti più bui senza mai esitare, grazie alla quale ho capito che cos'è l'amore e che desidero avere accanto per tutta la vita.

Infine, immancabilmente, voglio ricordare e ringraziare mia nonna Liliana che, purtroppo, se n'è andata nel 2017 e non potrà leggere queste righe. Gran parte di quello che sono lo devo a lei, che mi ha insegnato tantissimo, e la porterò per sempre nel cuore.